UNIVERSITY OF CALIFORNIA
SANTA CRUZ

SIMULATING THE PRODUCTION AND EVOLUTION OF EARLY-TYPE GALAXIES

A dissertation submitted in partial satisfaction of the
requirements for the degree of

DOCTOR OF PHILOSOPHY

in

PHYSICS

by

Lauren Porter

June 2013

The Dissertation of Lauren Porter
is approved:

Professor Joel R. Primack, Chair

Professor Sandra M. Faber

Professor Rachel S. Somerville

Dean Tyrus Miller
Vice Provost and Dean of Graduate Studies

Table of Contents

List of Figures

List of Tables

Abstract

Simulating the Production and Evolution of Early-Type Galaxies

by

Lauren Porter

We construct a simple prescription based on hydrodynamical simulations to predict the effective radii and velocity dispersions of early-type galaxies. We apply this prescription to a semi-analytic model, allowing for bulge formation via major and minor mergers as well as disk instabilities. We find that it is necessary to include disk instabilities in the model to reproduce the mass function of early-type galaxies, and that galaxies that form bulges via disk instability tend to form bulges earlier. This model is able to reproduce the low-redshift size-mass and Fundamental Plane relations. It predicts a degree of curvature in the Faber-Jackson relation that is not seen in local observations, but this could be offset if higher mass spheroids have more bottom-heavy initial mass functions. The model is also able to match the observed rapid evolution of the size-mass relation out to higher redshifts, as well as the slower evolution in the normalization of the Faber-Jackson relation.

Separating galaxies based on their morphology and peak central surface density, we determine the effects of mergers, disk instabilities, and quiescent star

formation on the sizes, surface densities, and star formation rates of massive galaxies. In agreement with observations, we find populations of compact red and blue galaxies at high redshift. We find that simulated compact star-forming galaxies are most likely to form from compact disks undergoing gravitational instabilities. While minor and gas-poor mergers have the effect of increasing the sizes of all bulge-dominated galaxies, the galaxies with large amounts of disk instability activity remain the most compact even in the local Universe.

We predict the effective radius, velocity dispersion, luminosity, age, and metallicity of bulge-dominated galaxies, enabling us to compare directly to observations of early-type galaxies. While we find a tight correlation between age and metallicity and velocity dispersion, we find a stronger dependence of metallicity on effective radius than observations report. We find that the correlations with velocity dispersion arise as a result of the strong link between the assembly time of a galaxy and its velocity dispersion. Furthermore, minor mergers introduce a large amount of scatter in size, weakening any dependence on effective radius. The strong relationship between effective radius and metallicity stems from the tight mass-metallicity relationship in the SAM. We examine the formation and assembly histories of the simulated galaxies and find that the scatter in the fundamental plane results from structural differences in the galaxies themselves and not passive fading from a young, bright stellar population.

To my parents,

Kevin and Joyce Porter,

who taught me to love learning

and dream of the stars.

Chapter 1

Introduction

Most of the mass in the Universe is in the form of dark matter. While the detailed structure of dark matter is not yet well understood, dark matter is thought to be move slowly compared to the speed of light and interact primarily through the gravitational force. In the standard ΛCDM cosmology dark matter structure forms hierarchically, with small halos forming first and larger structures forming from the merger of smaller halos (Blumenthal et al., 1984).

In this way small fluctuations in the density of the Universe give rise to ever-larger structures at later times. The evolution in size, shape, and structure of dark matter halos over time can be predicted and simulated using a variety of analytical methods (Zel'Dovich, 1970; Gunn & Gott, 1972; Press & Schechter, 1974) and N-body simulations (Centrella & Melott, 1983; Davis et al., 1985; Navarro et al.,

1996; Bullock et al., 2001; Springel, 2005; Klypin et al., 2011).

To first order baryonic matter in the universe tracks the density of the underlying dark matter structure. At high redshifts ($z > 20$) hot gas clouds within dark matter halos first began to cool and collapse, forming the seeds of high-redshift galaxies (Silk, 1977; Tegmark et al., 1997). These primordial galaxies then grow and evolve into the galaxies seen today, with merger histories dictated by those of the dark matter halos.

In the local Universe galaxies fall into two broad categories (Kennicutt, 1998b; Strateva et al., 2001; Kauffmann et al., 2003; Baldry et al., 2004): 'red sequence' or 'early-type' galaxies tend to be massive, quiescent, and bulge-dominated. These galaxies have old stellar populations, low gas fractions, and are relatively dense. In contrast 'blue cloud' or 'late-type' galaxies are less massive, with ongoing star formation, and large disks.

Since we believe small structures form first, mergers between galaxies would seem to be a natural explanation for this dichotomy. Indeed, hydrodynamical simulations have shown that elliptical galaxies may be created through major mergers of gas-rich disk galaxies, inducing massive amounts of star formation and forming a compact pressure-supported bulge from a rotation-supported disk (e.g. Toomre & Toomre, 1972; Toomre, 1977; Mihos & Hernquist, 1994; Barnes & Hernquist, 1996). More recent works have indicated that these same mergers

may account for the differing scaling relations between stellar mass, luminosity, effective radius, and velocity in disk galaxies and elliptical galaxies (Cox et al., 2006; Dekel & Cox, 2006; Naab et al., 2006; Robertson et al., 2006a; Covington et al., 2008; Hopkins et al., 2009b; Covington et al., 2011). Subsequent 'dry' mergers between gas-poor elliptical galaxies have been demonstrated to build up a diffuse bulge, while leaving the center relatively dense (e.g., Khochfar & Burkert, 2003; Naab et al., 2007; Naab et al., 2009; Oser et al., 2012). Such a picture would be consistent with observations suggesting elliptical galaxies formed their centers rapidly, while the outer regions were accreted over time (van Dokkum et al., 2010; Forbes et al., 2011).

The question remains, however, whether the frequency of these merger events is high enough to produce the population of elliptical galaxies seen at low redshift. Several toy models (Trujillo et al., 2011; Newman et al., 2012; Quilis & Trujillo, 2012) have attempted to quantify the amount of size growth that major and minor mergers can induce, concluding that there are not enough minor mergers to account for the rapid size evolution in elliptical galaxies. Alternative theories, including mass loss and the 'puffing up' of elliptical galaxies due to quasar activity, have been invoked (Fan et al., 2010).

More recently, both hydrodynamical simulations and high-redshift observations have proposed an alternative method of bulge formation. Bulges may form

in-situ, either via bar formation that destabilizes the disk, transferring mass into a bulge component (Toomre, 1964) or via clumps of gas that migrate inwards (Dekel et al., 2009a; Bournaud et al., 2011; Genzel et al., 2011; Dekel et al., 2013) though 'disk instabilities' (DI). Although hydrodynamical simulations (Naab et al., 2007) have shown that early-type galaxies can be formed without having undergone a major merger, the efficiency of bulge formation in these processes is not yet well-constrained.

As part of his thesis work, Matt Covington formed a simple analytic model to predict the sizes and velocity dispersions for bulge-dominated galaxies created from the merger of two disk-dominated galaxies (Covington et al., 2008, hereafter C08). When applied to two semi-analytic models (SAMs) of galaxy formation (Croton et al., 2006; Somerville et al., 2008b), this model showed (Covington et al., 2011, hereafter C11) that major mergers can account for the slope, zero-point, and dispersion of the elliptical size-mass relation (Shen et al., 2003), the relation between stellar mass and velocity dispersion ('Faber-Jackson', Faber & Jackson, 1976), and the relation between size, velocity dispersion, and stellar mass ('Fundamental Plane', Djorgovski & Davis, 1987; Dressler et al., 1987; Faber et al., 1987). However this model was applied in post-processing and did not attempt to account for any subsequent major or minor mergers or bulge growth through disk instabilities.

In this work we extend the work of C08 and C11 to include major and minor mergers between galaxies of all morphologies, as well as disk instabilities (Chapter 2). These improvements allow us to calculate the stellar radius and velocity dispersion for all bulge-dominated galaxies in a SAM (Somerville et al., 2012, hereafter S12) at all times. We then use this model to form the various known scaling relations for early-type galaxies at both low and high redshifts, comparing to observations where they are available and making predictions where they are not (Chapter 3). We show that the model is able to accurately reproduce the observed size-mass relation from z=0 to z=1.5, and that including bulge growth through disk instabilities is necessary to reproduce the observed morphologically-separated mass function.

In Chapter 4 we examine the evolution of disk-dominated and bulge-dominated galaxies in more detail. We find a population of bulge-dominated galaxies at z=0 that underwent a period of rapid star formation accompanied by a large increase in surface density. Tracing the formation histories of these galaxies, we find that 'blue nugget' galaxies originate from the most compact disk-dominated galaxies at high redshift. These galaxies then experience large amounts of bulge growth through disk instabilities, forming compact spheroids. In contrast stellar bulges that form from mergers tend to be somewhat larger, and form at later redshifts.

In Chapter 5 we study the Fundamental Plane of low-redshift early-type galax-

ies. Separating galaxies by their scatter around the Fundamental Plane, we examine correlations with stellar age and metallicity. We find that these stellar population parameters are more dependent on effective radius than velocity dispersion, in agreement with observations. We compare the formation histories of galaxies with low and high surface brightnesses at a given velocity dispersion and effective radius, showing that the difference in surface brightness is more due to the structural differences between galaxies than the stellar populations within galaxies.

All results presented here assume a ΛCDM cosmology, with cosmological parameters taken from the Wilkinson Microwave Anisotropy Probe (WMAP) 5/7-year results: $\Omega_m = 0.28$, $\Omega_\Lambda = 0.72$, $h = 0.70$, $\sigma_8 = 0.81$ (Komatsu et al., 2009, 2011).

Chapter 2

The Semi-Analytic Model

2.1 Introduction

Semi-analytic models provide a framework for examining methods of bulge formation. Previous works (De Lucia et al., 2011; Fontanot et al., 2012) have used SAMs to show the importance of mergers and disk instabilities in building the population of early-type galaxies, and have proposed an evolutionary link between the bulge mass, AGN mass, and quenching of massive galaxies (Croton et al., 2006). De Lucia et al. (2006) showed that the growth of elliptical galaxies is anti-hierarchical; the stars in more massive galaxies form earlier, but assemble later.

The Somerville et al. (2008b, 2012) SAM 'GF' also is successful in predict-

ing many properties of local disk galaxies, notably the size-mass relationship for disk-dominated galaxies (Somerville et al., 2008b), the morphologically-separated stellar mass functions, and the cold gas mass function. The SAM also reproduces the observed major merger rate of galaxies, though it underpredicts the minor merger rate (Lotz et al., 2011).

These successes indicate that this SAM is well-equipped to predict the properties of early-type galaxies. A preliminary model (Covington et al., 2011) based on an analytic treatment of galaxy mergers in hydrodynamical simulations (Covington et al., 2008) showed promising results; in particular the SAM was able to reproduce the tilt of the Faber-Jackson relation and produce bulge-dominated galaxies that were smaller and obeyed a steeper size-mass relation than disk-dominated galaxies. However that model was limited in that the sizes and velocity dispersions were calculated via post-processing, and only for major mergers between two disk-dominated galaxies. Here we extend the model to include all mergers as well as disk instabilities, allowing for a self-consistent calculation of size and velocity dispersion at all redshifts. In this chapter we provide a brief overview of all the mechanisms in the SAM, paying particular attention to the areas where the current SAM differs from recently-published versions (Somerville et al., 2008b, 2012; Hirschmann et al., 2012). We detail the model, motivated by hydrodynamical simulations, that we use to predict the effective radii and velocity

dispersions of bulge-dominated galaxies.

2.2 Methods

The SAM used is an extension of the model of Somerville et al. (2001, 2008b, 2012). Galaxies form, evolve, and merge in a hierarchical manner, following the growth of their underlying dark matter halos. We include prescriptions for the radiative cooling of gas, star formation, supernova feedback, AGN activity, and chemical enrichment of the stars, interstellar medium (ISM), and intergalactic medium (IGM). We provide a summary of the mechanisms used here, emphasizing the differences between this model and previous versions. For the full details of the SAM, we refer readers to Somerville et al. (2008b).

GF is rooted in a merger tree (Behroozi et al., 2013) drawn from the Bolshoi N-Body dark matter simulation (Klypin et al., 2011; Trujillo-Gomez et al., 2011). This simulation is complete down to $V_{circ} = 50$ km/s, with a force resolution of 1 h^{-1} kpc and a mass resolution of 1.9×10^8 $M_\odot$. This is the first version of the SAM to be based on a cosmological merger tree; the high resolution and precise statistics allow us to determine the local environment of galaxies as well as the growth of low-mass halos.

When two dark matter halos merge we define the 'central' galaxy as the most massive galaxy of the larger halo, with all other galaxies termed 'satellites.' The

satellite galaxies then lose angular momentum and merge with the central galaxy on a timescale determined by Boylan-Kolchin et al. (2008). Satellites are tidally stripped during this process, so that satellites with long merger timescales may become tidally disrupted and destroyed before they merge with the central galaxy. In this case, the stars from the satellite are added to a diffuse stellar halo. We do not allow satellite galaxies to merge with other satellites in this model.

2.2.1 Gas cooling

Gas cools and condenses from a reservoir of hot gas in the dark matter halo. Before reionization, the amount of hot gas in the halo is equal to the baryon fraction multiplied by the halo mass; once reionization begins, the amount of collapsed gas is a function of the timescale of reionization and the halo mass. We treat this quantity using a parameterization (Gnedin, 2000; Kravtsov et al., 2004), using $z_{overlap} = 12$ as the redshift at which H II regions first overlap and $z_{reion} = 11$ as the redshift at which the universe is fully reionized.

The hot gas is initialized at the virial temperature of the halo and follows an isothermal density profile, $\rho_{\rm gas}(r) = m_{\rm hot}/(4\pi r^2 r_{\rm vir})$, where $m_{\rm hot}$ is the mass of hot gas and $r_{\rm vir}$ is the virial radius of the halo. This gas then cools from the center to progressively larger radii on a timescale $t_{\rm cool}$ dependent on the density of the hot gas. We can thus define a cooling radius $r_{\rm cool}$ as the radius within which all

the enclosed gas has had enough time to cool. This radius is calculated using the temperature- and metallicity-dependent atomic cooling curves of Sutherland & Dopita (1993).

By setting the cooling time to be equivalent to the dynamical time of the halo, we find that $t_{\rm cool} \propto r_{\rm vir}/V_{\rm vir}$, where $V_{\rm vir}$ is the virial velocity of the halo. If the cooling radius is less than the virial radius then solving for the mass within the cooling radius and differentiating yields a cooling rate of

$$\dot{m}_{\rm cool} = 0.5 m_{\rm hot} \frac{r_{\rm cool}}{r_{\rm vir}} \frac{1}{t_{\rm cool}}. \tag{2.1}$$

If the cooling rate is larger than the virial radius then the cooling rate is given by the rate at which gas falls into the halo,

$$\dot{m}_{\rm cool} = 0.5 m_{\rm hot} \frac{1}{t_{\rm cool}}. \tag{2.2}$$

These two modes of gas accretion are termed 'hot' and 'cold' mode accretion, respectively. In the 'hot' mode gas is assumed to be shock-heated to the virial temperature of the halo, resulting in relatively long cooling times. In the 'cold' mode the gas is thought to penetrate the halo via filamentary streams or 'cold flows' (Birnboim & Dekel, 2003; Kereš et al., 2005; Dekel et al., 2009a), and is never shock-heated. The transition between these two regimes is dependent on halo mass and redshift, with cold flows becoming more dominant at higher redshifts and lower halo masses.

In this SAM we associate cold gas with the central halo, so that only the central galaxy may accrete gas. Accreted satellite galaxies retain their cold gas upon their accretion into a larger halo, but this gas is typically consumed on a short timescale. This produces a population of satellite galaxies that is unrealistically red and old, as true satellite galaxies may preserve some of their hot gas haloes, producing a supply of cold gas even after they are accreted. As we are mainly concerned with the properties of massive early-type galaxies we will defer a more realistic treatment of satellite galaxies to future work.

2.2.2 Disk formation

As gas cools, we assume it settles into a rotationally-supported exponential disk. Assuming the halo follows an NFW profile (Navarro et al., 1997) and responds adiabatically to disk formation, we can use conservation of angular momentum to find the scale radius of the disk given the halo's concentration and spin, and the ratio of baryons in the disk to the mass of the halo. We assume that halo spin is distributed evenly with redshift, so that size evolution with redshift is driven by evolution in the baryonic fraction and halo concentration, which scales as $c \propto (1+z)^{-1}$ in our model (Bullock et al., 2001). This prescription is based off the work of Mo et al. (1998) and described in further detail in Somerville et al. (2008a), and has been shown to reproduce the scaling relations for disk galax-

ies out to z $\sim$ 2. In contrast to Somerville et al. (2008a) here we calculate the baryon fraction of the disk directly and assume that the scale radius is the scale length of the gas disk. We convert between the disk and gas scale lengths using $r_{\rm gas} = \chi\ r_{\rm stars}$, where $\chi = 1.7$.

2.2.3 Quiescent star formation

We allow for two modes of star formation: 'quiescent' star formation, which occurs in disks at all timesteps, and 'burst mode' star formation, which occurs after two galaxies merge or after a disk instability. Stars are assumed to form following a Chabrier (2003) initial mass function (IMF). We use an instantaneous recycling approximation to incorporate stellar mass loss; at every time-step a fraction R = 0.43 of the stars formed is returned to the cold gas. This parameter has been shown to be a good approximation to the mass loss from massive stars in a Chabrier IMF (Bruzual & Charlot, 2003).

In the 'quiescent' mode the star formation rate is dependent on the surface density of cold gas in the disk, following the empirical Schmidt-Kennicutt relation (Kennicutt, 1988, 1998a):

$$\dot{\Sigma}_{\rm SFR} = A_{\rm Kenn}\Sigma_{\rm gas}^{N_{\rm K}}, \tag{2.3}$$

where, $A_{\rm Kenn} = 1.67 \times 10^{-4}$, $N_{\rm K} = 1.4$ and $\Sigma_{\rm gas}$ is the surface density of cold gas in the disk. Only gas above a critical density threshold $\Sigma_{crit} = 6{\rm M}_{\odot}\ {\rm pc}^{-2}$ is allowed

to form stars. All stars that form in the 'quiescent' mode are added to the disk.

2.2.4 Mergers

Mergers between two galaxies are assumed to trigger a burst of star formation, with an efficiency that is dependent on the gas fraction of the central galaxy's disk and the mass ratio of the two progenitors. This efficiency is parameterized based on the results of hydrodynamical simulations (Robertson et al., 2006b; Cox et al., 2008; Hopkins et al., 2009a); a higher efficiency produces a higher star formation rate and destroys a higher fraction of the disk, transferring that stellar mass to a spheroid. Following Hopkins et al. (2009a,d) the efficiency increases with mass ratio and decreases with gas fraction; in extremely gas-rich disks there is not enough stellar mass to create a torque between the gas and stars, and so the gas cannot lose its angular momentum and collapse. This is the same approximation as used in S12 but represents an improvement from S08, in which the merger efficiency was strictly an increasing function of mass ratio.

All the stars formed in the 'burst' mode are added to the bulge of the remnant. We also allow for a fraction $f_{scatter} = 0.2$ of the stars in the satellite galaxy to be scattered into the diffuse stellar halo; all of the other stars in the satellite galaxy are added to the bulge. In addition, we allow for violent relaxation (Lynden-Bell, 1967), wherein a portion of the central galaxy's stellar disk at final coalescence

will scatter and become dispersion-supported . Following Hopkins et al. (2009a,d) we set the fraction of the disk that participates in the violent relaxation to be equivalent to the mass ratio of the merger, which is roughly equivalent to the fraction of the central galaxy's stellar disk that lies within the radius of the satellite galaxy at coalescence.

2.2.5 Supernova feedback and chemical enrichment

Massive stars and supernovae are assumed to produce winds that drive cold gas back into the ISM and IGM, heating the gas in the process. The mass outflow rate is proportional to the star formation rate,

$$\dot{m}_{rh} = \epsilon_{\rm SN} \left(\frac{200 \text{ km s}^{-1}}{V_{\rm disk}} \right)^{\alpha_{rh}} \dot{m}_*, \tag{2.4}$$

where $\epsilon_{\rm SN} = 1.5$ and $\alpha_{rh} = 2.2$ are free parameters and $V_{\rm disk}$ is the circular velocity of the disk, set to equal the maximum rotation velocity of the dark matter halo. The proportion of the gas that is ejected from the halo entirely is a decreasing function of the halo's virial velocity. This gas can then fall back into the ISM, at a reinfall rate that is proportional to the mass of the ejected gas and inversely proportional to the dynamical time of the halo.

We model chemical enrichment using an extension of the instantaneous recycling approximation. Whenever a mass dm_* of stars is formed, we add a mass of metals d$M_{\rm Z} = y\ dm_*$ to the cold gas, where the chemical yield value y = $1.5 Z_\odot$

is a free parameter. Newly-formed stars are assumed to have the same metallicity as the mean metallicity $Z_{\rm cold}$ of the cold gas in the galaxy at that timestep. When gas is ejected due to supernova feedback, these winds are assumed to have a metallicity $Z_{\rm cold}$; similarly, reinfalling gas is assumed to have the same metallicity as the mean metallicity of the IGM.

2.2.6 Disk instabilities

Observations and hydrodynamical simulations have shown that gas-rich disks can undergo gravitational fragmentation, forming star-forming clumps (Dekel et al., 2009b; Genzel et al., 2011). These clumps then migrate to the center of the galaxy, providing an alternative pathway to bulge formation.

Other SAMs have shown that these disk instabilities (DI) have the greatest importance in intermediate-mass early-type galaxies (Guo et al., 2011; De Lucia et al., 2011; Shankar et al., 2013). However the current generation of SAMs is not equipped to precisely estimate the instability criterion; indeed nearly every modern SAM adopts a different threshold for instability as well as the behavior of the gas and stars when in this mode. While recent hydrodynamical simulations (Dekel et al., 2009b; Genel et al., 2012b; Ceverino et al., 2012; Dekel et al., 2013) have made progress on this front, the timescale of clump migration and amount of mass transferred may vary with the feedback recipe of the simulations. For this

reason, while we include a model of disk instabilities in the SAM, we emphasize that a more fully-developed theory is clearly needed.

We consider two models of disk instabilities: one in which the stability of the disk is only dependent on its stellar properties ('Stars DI'), and one that also takes the gaseous component of the disk into account ('Stars+Gas DI'). We also include a model with no bulge growth through disk instabilities ('No DI'); in this model stellar bulges only form in mergers between two galaxies.

We determine the stability of the disk using the Toomre (1964) parameter, using the criterion of Efstathiou et al. (1982) for a cold disk:

$$\epsilon = \frac{V_{\rm max}^2 \; r_{\rm disk}}{G \; M_{\rm disk}}, \tag{2.5}$$

where $V_{\rm max}$ is the maximum circular velocity of the halo, $r_{\rm disk}$ is the scale length of the stellar disk (in the 'Stars DI' model) or gas disk (in the 'Stars+Gas DI' model), and $M_{\rm disk}$ is the stellar (in the 'Stars DI' model) or baryonic (in the 'Stars+Gas DI' model) mass of the disk. We calculate ϵ at every timestep, and if the value is less than $\epsilon_{\rm crit}$ we transfer enough stellar mass to the bulge to restore stability (but see Athanassoula 2008, which claims that this criterion may be insufficient to determine the stability of the disk). In practice DI tends to occur in galaxies with high star formation rates in the disk, so that while stability is restored in a timestep, the disk will become unstable again at the next timestep, producing a cascade of instability events in the SAM.

Previous studies suggest that the value of $\epsilon_{\rm crit}$ is in the range of 0.6-1.1, with gaseous disks having a lower instability threshold then pure stellar disks (Efstathiou et al., 1982; Christodoulou et al., 1995; Mo et al., 1998; Syer et al., 1999); we find that using $\epsilon_{\rm crit} = 0.75$ in the 'Stars DI' model and 0.70 in the 'Stars+Gas DI' model reproduces the stellar mass functions for early- and late-type galaxies.

2.2.7 Black holes

Previous work (Hirschmann et al., 2012) has found that it is necessary to include black hole growth via both mergers and DI to reproduce the 'downsizing' trend, wherein more massive black holes form earlier. We use a modified version of those prescriptions; for more detail we refer the reader to Hirschmann et al. (2012).

Each galaxy is seeded with a 'heavy' black hole (Loeb & Rasio, 1994; Koushiappas et al., 2004; Volonteri & Stark, 2011), with a mass 10^5 $M_\odot$. When two galaxies merge their black holes are assumed to merge as well. A fraction $f_{\rm fuel,merge} = 0.10$ of the gas that interacts during the merger is allowed to fall into a low-angular momentum reservoir, fueling the black hole.

As the two galaxies approach coalescence the black hole begins to accrete cold gas, depositing energy into the ISM. If the mass of the black hole is below a critical threshold the black hole accretes at the Eddington rate; once the mass of

the black hole passes this threshold (or if the total mass of the two progenitor black holes exceeds the critical threshold) the accretion rate falls with a declining power law until the gas reservoir is depleted. Following Hopkins et al. (2007) the critical mass is set to be

$$\log M_{\rm crit}/M_{*,\rm bulge} = f_{\rm crit} * [-3.27 + 0.36\,{\rm erf}[(f_{\rm gas} - 0.4)/0.28]], \qquad (2.6)$$

where $M_{*,\rm bulge}$ is the stellar mass of the bulge, $f_{\rm gas}$ is the gas fraction of the merger, and $f_{\rm crit} = 1.0$ is a tunable parameter set to reproduce the redshift zero relationship between the mass of the black hole and the mass of the stellar bulge (McConnell & Ma, 2013).

In the 'Stars DI' and 'Stars+Gas DI' models black holes are also allowed to grow following a DI, using a similar mechanism as in the case of major mergers. As with mergers, the growth of the black hole is limited by the amount of low angular momentum material in the center of the galaxy following an instability event. We limit this term to be a fraction $f_{\rm fuel,DI} = 0.002$ of the mass that is transferred from the disk to the bulge. We determine the critical black hole threshold using equation 2.6, setting $f_{\rm gas}$ to be the gas fraction of the disk and keeping $f_{\rm crit}$ as a tunable parameter. We find that setting $f_{\rm crit} = 1.0$ and 0.6 in the 'Stars DI' and the 'Stars+Gas DI' models, respectively, reproduces the observed black hole-stellar bulge scaling relation at redshift zero.

The high gas inflow rate rate at high redshifts tends to produce gas-rich disks

that are unstable for extended periods of time in the 'Stars+Gas DI' model. Allowing the black hole to accrete at the Eddington rate for this duration would produce black holes that are too massive at high redshifts. As a consequence we limit the DI-triggered black hole accretion rate to be a fraction $f_{\rm Edd,DI} = 0.01$ of the Eddington limit in this model.

Black holes are also allowed to grow via 'radio mode' feedback. This mechanism is motivated by the association of black holes with radio jets heating gas in a hot halo, and assumes that black holes grow via Bondi-Hoyle accretion (Bondi, 1952) when galaxies are in the 'hot mode' regime.

The accretion rate onto the black hole is given by

$$\dot{m}_{\rm radio} = \kappa_{\rm radio} \frac{k{\rm T}}{\Lambda(T, Z_h)} \frac{M_{\rm bh}}{10^8 {\rm M}_\odot}, \tag{2.7}$$

where kT is the temperature of the hot gas , $\Lambda(T, Z_h)$ is the cooling function for hot gas (Sutherland & Dopita, 1993), $M_{\rm bh}$ is the mass of the black hole, and $\kappa_{\rm radio}$ is a free parameter tuned to match the accretion rate of observed elliptical galaxies.

We assume that this mechanism of black hole growth can couple to the hot gas in the halo, preventing further cooling. If the radius of cool gas in the galaxy is less than the virial radius of the halo, we reduce the cooling rate by

$$\dot{m}_{\rm heat} \propto \frac{\dot{m}_{\rm radio}}{V_{\rm vir}^2}, \tag{2.8}$$

where $V_{\rm vir}$ is the virial velocity of the halo. While this accretion rate is sub-Eddington, it serves to limit gas cooling at late times and in massive galaxies (Croton et al., 2006). In practice this feedback is required to reproduce the high-mass cutoff in the stellar mass function.

2.3 Model to predict effective radius and velocity dispersion

2.3.1 Effective radius

A major improvement in this SAM is in the prediction of effective radii and velocity dispersions for bulge-dominated galaxies. Using hydrodynamical simulations (Cox, 2004; Cox et al., 2006, 2008), C08 developed an analytic model to predict the effective radius and velocity dispersion following the major merger of two disk galaxies. This model was based upon the virial theorem and additionally incorporated energy losses due to dissipation. In further work, C11 simplified the model and applied it via post-processing to mergers of disk-dominated galaxies with properties taken from the Croton et al. (2006) Millennium SAM and the S08 SAM. C11 showed that the C08 model reproduces the observed steepening in the size-mass relation of ellipticals when compared to disks, as well as the observed decreased dispersion in radius compared to the progenitor galaxies (Shen et al.,

2003). The model predicted a small dispersion in the size-mass relation for early-type galaxies despite the large size-mass dispersion of the progenitor disk galaxies. This results because the larger disk galaxies tend to be gas-rich, and the merger drives gas to the center producing smaller stellar spheroids; in contrast smaller disk galaxies tend to be gas poor, producing more diffuse stellar spheroids. The contrast between these two processes produces remnants that are of similar sizes, irrespective of the sizes of the progenitor galaxies. In addition, this model qualitatively reproduced the evolution of these properties versus redshift (Trujillo et al., 2006). The C08 model was also shown to correctly reproduce a tilt in the FP away from the simple virial relation. Using the methods of C08 and C11, as well as an alternative prescription from Hopkins et al. (2009c), Shankar et al. (2011) reached similar conclusions.

In the case of a merger without dissipation, simple conservation of energy arguments would predict that the internal energy of the two progenitors is conserved during the merger:

$$C_{\rm int} \sum_{i=1}^{2} G \frac{(M_{*,i} + M_{\rm new*,i})^2}{R_{*,i}} = C_{\rm int} G \frac{M_{\rm f}^2}{R_{\rm f}}, \tag{2.9}$$

where $M_{*,i}$ is the stellar mass of each of the two progenitors, $M_{\rm new*,i}$ is the mass of stars formed during the merger, $R_{*,i}$ is the effective radii of the progenitors, $M_{\rm f}$ and $R_{\rm f}$ are the stellar mass and effective radius of the merger remnant, and $C_{\rm int}$ is a dimensionless constant relating the internal energy of the galaxy to GM^2/R.

However, major mergers are typically dissipative, inducing large amounts of star formation (Dekel & Cox, 2006; Robertson et al., 2006a; Hopkins et al., 2009d); thus the conservation of energy relation must be modified with a term incorporating radiative losses. We note that the parameter $C_{\rm int}$ in equation 2.9 may actually have a degree of dependence on the morphology of the galaxy, but we have not attempted to account for that here.

Motivated by the results of hydrodynamical simulations (Cox et al., 2006, 2008), Covington et al. (2008) provides a simple parameterization of this radiative energy loss:

$$E_{\rm rad} = C_{\rm rad} \sum_{i=1}^{2} K_i f_{{\rm g},i} f_{{\rm k},i} (1 + f_{{\rm k},i}), \tag{2.10}$$

where K_i, $f_{{\rm g},i}$, and $f_{{\rm k},i}$ are the total kinetic energy, baryonic gas fraction, and fractional impulse of progenitor i, $C_{\rm rad}$ is a dimensionless constant and the sum is over the two progenitors. Adding this term to the left hand side of equation 2.9 provides a natural way to incorporate dissipation in the calculation of the effective radius of elliptical galaxies. Mergers with higher amounts of dissipation and star formation produce remnants with smaller effective radii, allowing for the creation of compact elliptical galaxies from diffuse spiral galaxies.

These two formulae have previously been shown to provide accurate predictions for the effective radii of elliptical galaxies resulting from the gas-rich mergers of spiral galaxies (Covington et al., 2008, 2011). In this case, the constants $C_{\rm rad}$

and $C_{\rm int}$ were measured by fitting the relations to a suite of hydrodynamical merger simulations (Cox et al., 2006, 2008). Incorporating a simplified version of these formulae in semi-analytic models has been shown to reproduce the size-mass relation of early-type galaxies (Shankar et al., 2013).

This model was limited in that it was only calibrated against gas-rich mergers and was applied to SAMs via post-processing. As a result there were additional uncertainties such as the efficiency of star formation that had to be parameterized. In this work we extend the model to include all mergers between two galaxies, so that we may self-consistently calculate the effective radius at any timestep.

We calibrate our model against 68 GADGET-2 (Springel, 2005) hydrodynamical simulations of binary mergers, described in Johansson et al. (2009). This suite includes major (mass ratio $>$ 3:1) and minor mergers between two disk-dominated galaxies (D-D), and between a disk-dominated and bulge-dominated galaxy (B-D). It also contains major mergers between two bulge-dominated galaxies (B-B); the only merger morphologies lacking are those of minor mergers between two bulge-dominated galaxies, and mergers between a larger disk-dominated galaxy and a smaller bulge-dominated galaxy.

The bulge-dominated galaxies were formed from mergers of disk-dominated galaxies with gas fractions ranging from 20% to 80%, producing a range of stellar masses and gas fractions in all of the mergers. We have measured the three-

dimensional half-mass effective radii of these merger remnants directly, using these values to perform a χ^2 fit to constrain $C_{\rm int}$ and $C_{\rm rad}$. We calculate $C_{\rm int}$ and $C_{\rm rad}$ independently for the five categories of mergers described above.

Results are shown in Table 2.1 and Figure 2.1. The value of $f_{\rm rad} \equiv C_{\rm rad}/C_{\rm int}$ can be thought of as characterizing the relative importance of dissipation; high values indicate more dissipation. We find that this value is highest for major mergers for two disk-dominated galaxies ($f_{\rm rad} = 5.0$), is lower for minor mergers between two disk-dominated galaxies ($f_{\rm rad} = 2.7$) and is zero for mergers where one or both of the galaxies is bulge-dominated. This subset of mergers is thus essentially dissipationless; considering the average baryonic gas fraction in this group of mergers is 5.5% this is not an unexpected result. We note that in our estimates for both effective radius and velocity dispersion there are two significant outliers; these galaxies had high gas fractions and low pericentric distances, resulting in the largest proportions of star formation during the mergers. Thus these outliers may be an indication that the model breaks down in the most extreme merger events.

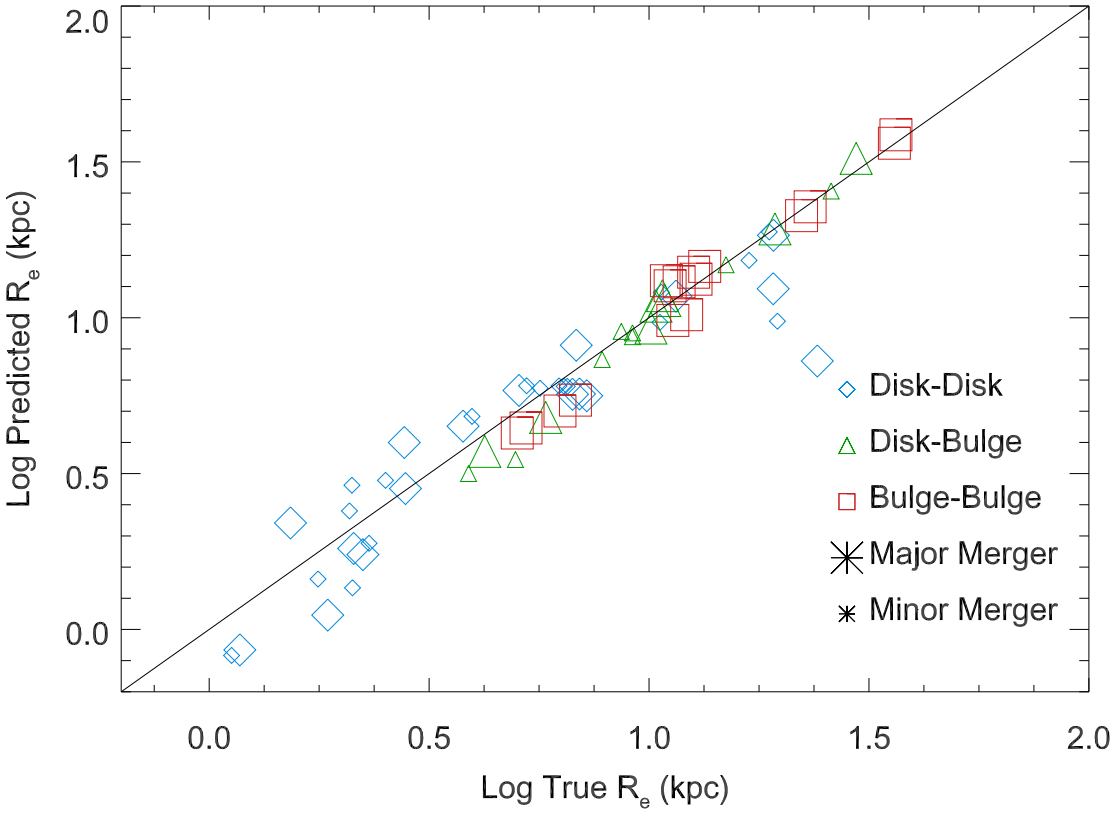

Figure 2.1: Predicted versus measured effective radius for the merger remnants of Johansson et al. (2009). The constants $C_{\rm int}$ and $C_{\rm rad}$ were calibrated independently for major (large symbols) and minor (small symbols) mergers, depending on the morphology of the progenitors (see Table 2.1). Blue diamonds represent mergers between two disk-dominated galaxies, green triangles represent mergers between a disk-dominated and a bulge-dominated galaxy, and red squares represent mergers between two bulge-dominated galaxies.

Merger	$C_{\rm int}$	$C_{\rm rad}$	Number
D-D	0.50	2.50	18
D-d	0.50	1.35	18
B-D	1.00	0.00	11
B-d	1.00	0.00	8
B-B	1.00	0.00	11

Table 2.1: Best-fit calculations of $C_{\rm int}$ and $C_{\rm rad}$ for the Johansson et al. (2009) hydrodynamical simulations. Progenitor types B and D designate bulge- and disk-dominated galaxies, respectively. Capital (lowercase) letters denote major (minor) mergers. Lower values of $C_{\rm rad}/C_{\rm int}$ represent mergers with less dissipation; mergers where $C_{\rm rad} = 0.0$ are essentially dissipationless.

2.3.2 Velocity dispersion

We use the virial theorem to determine the three-dimensional velocity dispersion of the remnant:

$$\sigma = \left(\frac{C_\sigma G}{2R_{\rm f}} \frac{M_{*,{\rm f}}}{(1 - f_{\rm dm,f})} \right)^{1/2}, \tag{2.11}$$

where $M_{*,{\rm f}}$ is the stellar mass of the remnant (or the single galaxy, in the case of disk instabilities), $R_{\rm f}$ is the stellar half-mass radius of the remnant, and C_σ is a dimensionless constant that accounts for the conversion between the three-dimensional effective radius and the line-of-sight projection of the velocity dispersion. $f_{\rm dm,f} = M_{\rm dm}/(0.5M_{*,{\rm f}} + M_{\rm dm})$ is the central dark matter fraction of the remnant (i.e. the proportion of mass within the stellar effective radius that is dark matter). Thus the term $0.5M_{*,{\rm f}} + M_{\rm dm} = 0.5M_{*,{\rm f}}/(1 - f_{\rm dm,f})$ represents the total amount of stars and dark matter within the stellar effective radius.

We have calculated C_σ using a least-squares fit for the five categories of merger

simulations described above. Stellar velocity dispersions were measured at the half-mass radius, using the average of 50 random line-of-sight projections. In this fit, the 'true' (rather than the 'predicted') half-mass radius was used. In all cases, the value of C_σ was between 0.29 and 0.31; thus we adopt the value $C_\sigma = 0.30$ for all mergers. Results are shown in Figure 2.2. We find that this model does an accurate job of reproducing the velocity dispersions of merger remnants, with relatively small scatter.

2.3.3 Implementation within the SAM

We apply these prescriptions in the SAM whenever two galaxies with a mass ratio greater than 1:10 merge. We assume orbital merger parameters following a statistical distribution (Wetzel, 2010) that is dependent on the redshift of the merger and the mass of the halo containing the more massive progenitor. Whereas in the hydrodynamical simulations we were able to measure the contribution of dark matter within one effective radius directly, in the SAM we assume that the two dark matter halos merge dissipationlessly and that the remnant halo follows an isothermal profile. This been shown in strong lensing results to be an accurate model for massive early-type galaxies (Auger et al., 2010).

The above formulae have only been calibrated against hydrodynamical simulations of binary mergers, but in the SAM we may also form a stellar bulge through

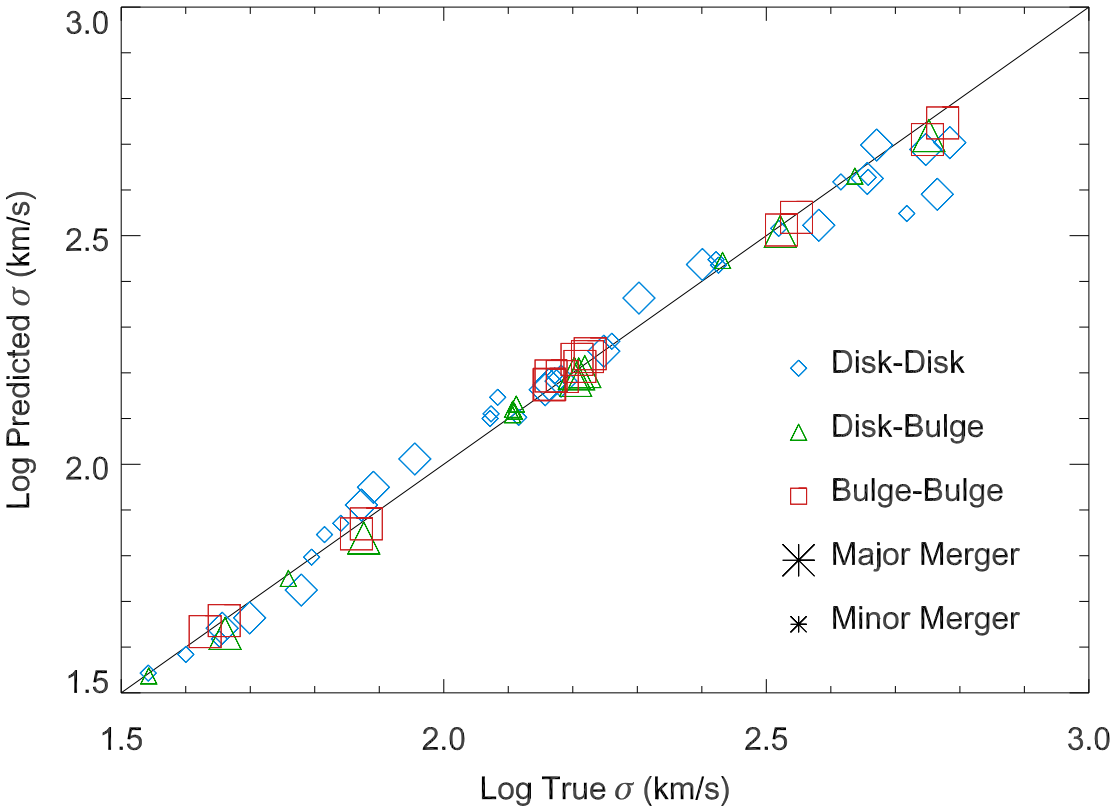

Figure 2.2: Predicted versus measured velocity dispersion for the merger remnants of Johansson et al. (2009). The constant C_σ was calibrated independently for major (large symbols) and minor (small symbols) mergers, depending on the morphology of the progenitors. All calibrations resulted in values $0.29 < C_\sigma < 0.31$; we adopt $C_\sigma = 0.30$ for all mergers. Blue diamonds represent mergers between two disk-dominated galaxies, green triangles represent mergers between a disk-dominated and a bulge-dominated galaxy, and red squares represent mergers between two bulge-dominated galaxies.

disk instabilities. In this case we follow the prescription of Guo et al. (2011), assuming that the new bulge mass forms from the center of the stellar disk, which has an exponential surface density profile: $\Sigma(r) = \Sigma_0 \exp(-r/r_{\rm d})$, $\Sigma_0 = M_d/2\pi r_{\rm d}^2$, where $M_{\rm d}$ is the mass of the disk and $r_{\rm d}$ is the scale length of the stellar disk. The radius $r_{\rm pb}$ of the disk enclosing this proto-bulge is then found by solving:

$$M_{\rm pb} = \frac{M_{\rm d}}{r_{\rm d}} \left[r_{\rm d} - e^{\frac{-r_{\rm pb}}{r_{\rm d}}} (r_{\rm d} + r_{\rm pb}) \right], \tag{2.12}$$

for $r_{\rm pb}$where $M_{\rm pb}$ is the mass of the disk transferred to the bulge in the instability event. We then assume that this stellar proto-bulge merges dissipationlessly with any existing bulge.

Having calculated the radius of the bulge following the disk instability, we model velocity dispersion using the same extension of the virial theorem that we use for mergers.

Chapter 3

Understanding Scaling Relations in Early-Type Galaxies

3.1 Introduction

While there are several proposed pathways to forming elliptical galaxies, the population as a whole obeys several key relations. Massive early-type galaxies tend to be older (Gallazzi et al., 2006), larger (Shen et al., 2003), and have higher velocity dispersions (Faber & Jackson, 1976) than their less-massive counterparts. Furthermore elliptical galaxies obey a relation between surface brightness, size, and velocity dispersion (Djorgovski & Davis, 1987; Dressler et al., 1987; Faber et al., 1987), termed the Fundamental Plane (FP). The existence of these relations

imposes tight constraints on models of spheroid formation.

These scaling relations have also been shown to evolve over time. While bulge-dominated galaxies in the local universe are smaller at fixed mass than their disk-dominated counterparts (Shen et al., 2003), the difference becomes even more pronounced at higher redshifts (Trujillo et al., 2006; Buitrago et al., 2008; Williams et al., 2010). This rapid increase in size is accompanied by a smaller increase in central velocity dispersion (Cappellari et al., 2009; Cenarro & Trujillo, 2009; Bezanson et al., 2011), suggesting that the cores of these galaxies are in place at high redshifts.

We use the GF SAM to form the known scaling relations for early-type galaxies, comparing to observations where available and making predictions where the observations have yet to yield results. In Section 3.2 we present the stellar mass function, bulge-to-total ratio, size-mass, Faber-Jackson, and Fundamental Plane relations for the simulated galaxies, from redshift 0 to redshift 1.75. We find that including disk instabilities has a negligible effect on the scaling relations, but that they are necessary to reproduce the low-redshift stellar mass function. We find that the SAM is able to reproduce the size, dispersion, and evolution in the size-mass relation, as well as the zero-point and evolution in the Faber-Jackson relation. We reproduce the scaling of the Fundamental Plane, and make predictions for the evolution of this scaling out to higher redshifts. We discuss the

implications of this model in Section 3.3.

Since the exact threshold for disk instabilities remains unclear, we present results without ('No DI') and with bulge growth via disk instabilities triggered by stars ('Stars DI') and stars and gas ('Stars+Gas DI'). We tune the above-mentioned parameters for black hole growth and disk instabilities to reproduce the stellar mass function and black hole-stellar bulge mass scaling relations at redshift zero. In the two DI models we apply the additional constraint of the morphologically-separated stellar mass functions at redshift zero to fix the instability criterion.

The observations we are comparing to use differing criteria to define 'early-type' galaxies; in particular an analysis (Cheng et al., 2011) of SDSS galaxies found that many selection criteria, such as concentration, can include a significant population of Sa and S0 galaxies in addition to ellipticals. In this analysis we use the stellar bulge-to-total ratio as a proxy for concentration, but we are careful to note that this population of early-types may include galaxies with significant disks.

3.2 Results

3.2.1 Stellar Mass Functions

We first compare to the observed (Moustakas et al., 2013) stellar mass function at redshift zero (Figure 3.1). As discussed in Section 3.1 the efficiency of the radio mode feedback in quenching star formation is tuned independently in all three models to reproduce the knee and high-mass end of the mass function.

All three models have an excess of low-mass galaxies. This problem is common to most SAMs (Bower et al., 2006; Guo et al., 2011, Lu et al. in prep) and may indicate the inefficiency of supernova feedback at preventing star formation in low-mass galaxies. A recent work has shown that this discrepancy may be alleviated by introducing additional parameters into the cold gas reincorporation timescale (Henriques et al., 2013). We note that all of the models either fall below the knee of the observed stellar mass function or lie above the observed high-mass turnover. This is an indication of the tension between matching the turnover and the high-mass cutoff of the mass function; increasing the strength of the radio mode feedback provides a better match to the high-mass end but underpredicts the knee of the stellar mass function.

We next turn to the morphologically-separated mass function, considering 'early-types' to be galaxies with stellar bulge-to-total ratios greater than 0.3, and

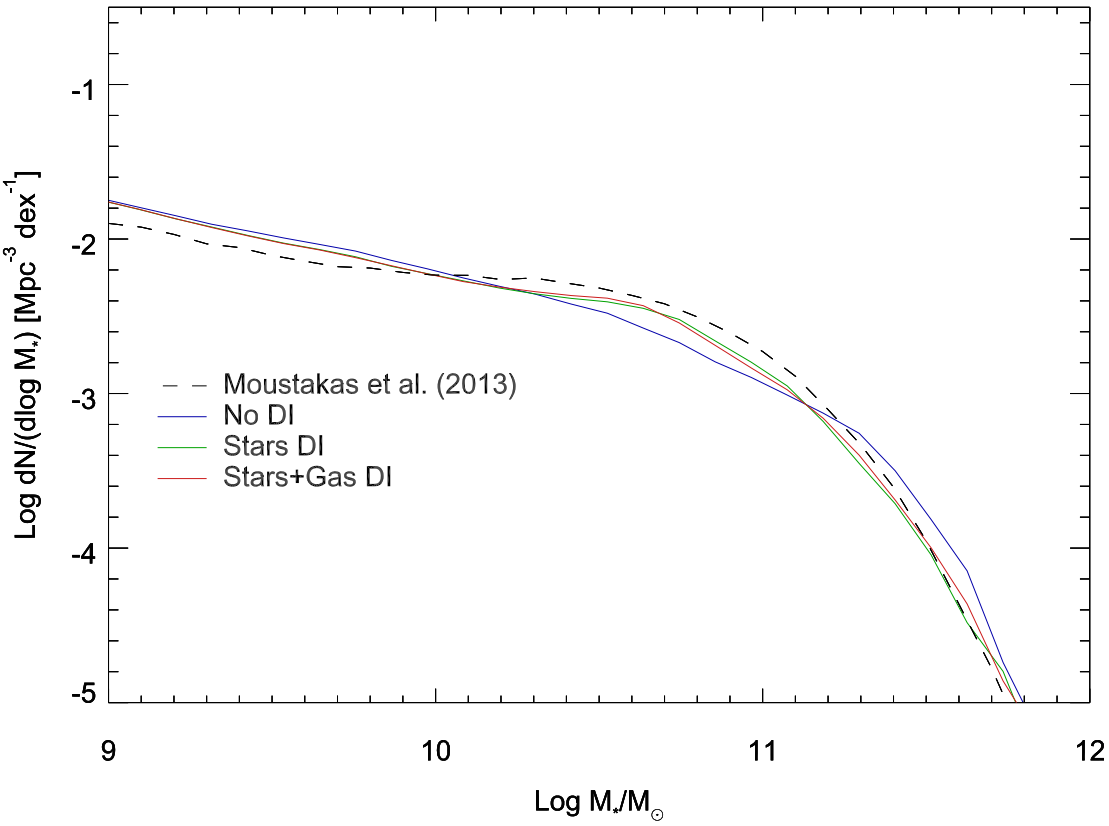

Figure 3.1: Stellar mass function at redshift zero. The three colored lines show the 'No DI' (blue), 'Stars DI' (green), and 'Stars+Gas DI' (red) versions of the SAM. The solid black line shows the observed mass function of Moustakas et al. (2013). All three models are able to approximately reproduce the observed stellar mass function.

'late-types' to have stellar bulge-to-total ratios less than 0.3. We compare against two sets of observations: the Bell et al. (2003) observations, separated by color and concentration, and the Baldry et al. (2012) observations, separated by color.

When galaxies are separated by bulge-to-total ratio, the differences between the three models become clearer. The model without disk instabilities has too many high-mass late-type galaxies, and too few intermediate-mass ($10^{10} < M_{\odot} < 10^{11}$) early-type galaxies. A similar result has been found in other SAMs (Parry et al., 2009; De Lucia et al., 2011), which use different prescriptions for disk instabilities and merger events. In contrast our 'Stars DI' and 'Stars+Gas DI' models match the observed early-type and late-type mass functions for all but the lowest-mass early-type galaxies. Thus mergers alone do not appear sufficient to reproduce the observed number densities of early-type galaxies. We remind the reader that our SAM is based on the merger trees of the Bolshoi simulation, which determine the number of major mergers.

3.2.2 Black hole-stellar bulge scaling relation

We next discuss the black hole-stellar bulge mass scaling relation for all galaxies from redshift 0 to 1.75. While observations have reached a general consensus regarding the slope and zero-point of the z = 0 relation (Häring & Rix, 2004; Sani et al., 2011; McConnell & Ma, 2013), at higher redshifts studies have tended to

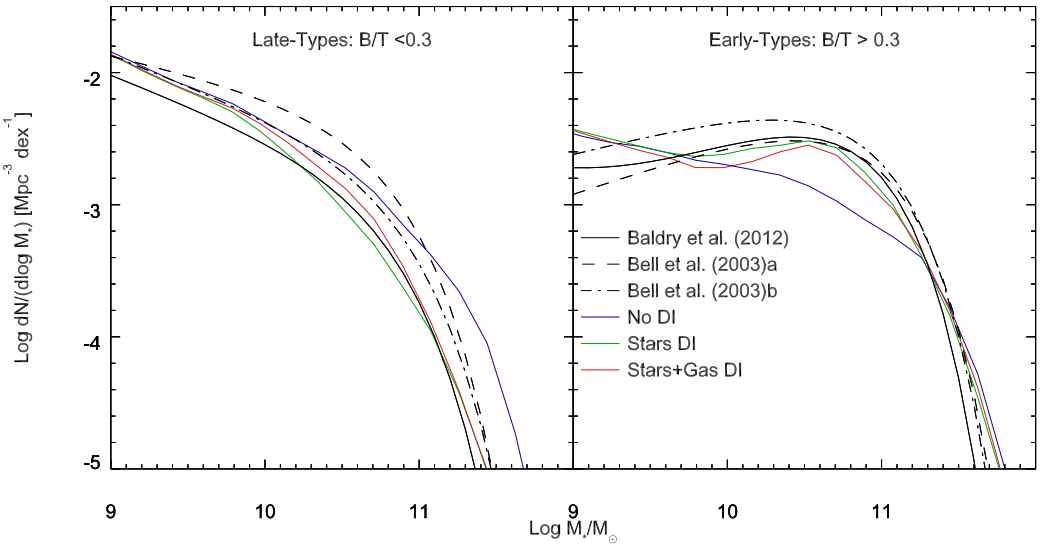

Figure 3.2: Stellar mass function at redshift zero, separated by the stellar bulge-to-total ratio. 'Late-types' (left pane) and 'Early-types' (right pane) have stellar bulge-to-total values less than and greater than 0.3, respectively. The three colored lines show the 'No DI' (blue), 'Stars DI' (green), and 'Stars+Gas DI' (red) versions of the SAM. The dashed and dot-dashed grey lines show the g-band mass functions,of Bell et al. (2003), separated by the g-r color-magnitude relation and concentration, respectively. The dotted black lines show the mass functions of Baldry et al. (2012), separated by the g-r color-magnitude relation. The version of the SAM without disk instabilities has too few early-type galaxies between 10^{10} and $10^{11}M_{\odot}$ and too many late-type galaxies above $10^{10}M_{\odot}$ compared to Baldry et al. (2012) and above $10^{11}M_{\odot}$ compared to Bell et al. (2003).

find differing results based upon their selection criteria. Observations of luminous AGN have found that the supermassive black hole grows more rapidly than the stars (Woo et al., 2008b; Merloni et al., 2010), while black holes in submillimeter galaxies tend to lag behind the host galaxy (Alexander et al., 2008).

The three models produce nearly identical results, falling within the observational errors of McConnell & Ma (2013) at redshift zero. At higher redshifts the models predict a slight downturn at the high mass end, indicating that the most massive stellar bulges form more rapidly than their supermassive black holes. We defer a comprehensive study of the evolution of the black hole scaling relations to future work (Hirschmann et al. in prep).

3.2.3 Growth of the stellar bulge

We next discuss the evolution of the stellar bulge-to-total ratio for all galaxies from redshift zero to 1.75 (Figure 3.4). At all redshifts, the models with disk instabilities produce galaxies that are more bulge-dominated, as indicated by the stellar mass functions. More significantly, the models with and without DI predict different evolutions of the bulge-to-total ratio. If disk instabilities are included, massive galaxies become bulge-dominated at high redshifts; above $10^{10.5}$ $M_{\odot}$ the majority of galaxies are bulge-dominated even at z = 1.75. This suggests that as galaxies increase in mass they move along this relation; evidently there is an upper

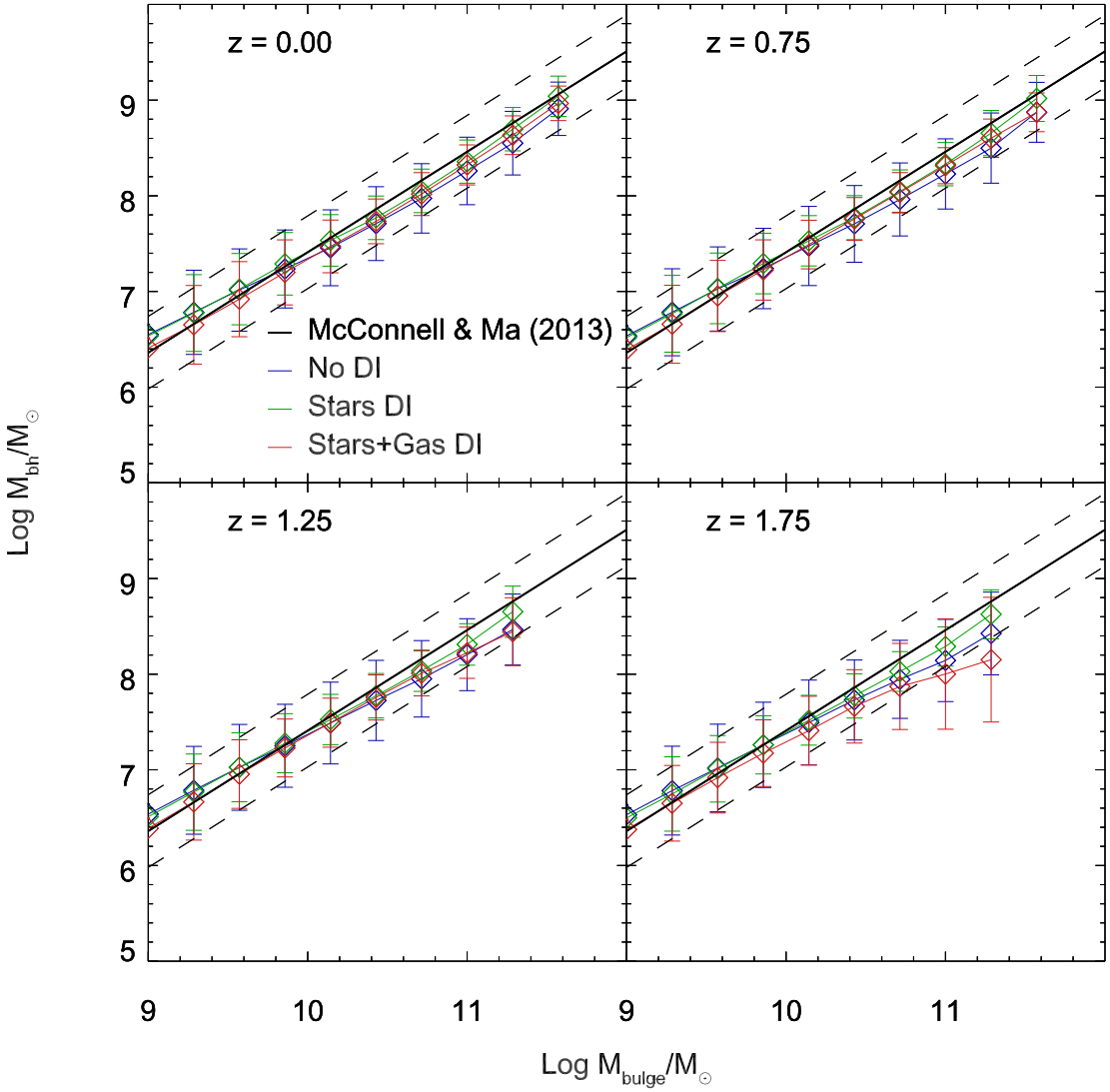

Figure 3.3: The black hole-stellar bulge mass scaling relation at redshifts z = 0.0, 0.75, 1.25, and 1.75 for the 'No DI' (blue), 'Stars DI' (green), and 'Stars+Gas DI' (red) versions of the SAM. The solid black line, with dashed $1-\sigma$ errors, shows the z = 0 observed relation from McConnell & Ma (2013). All three models have been tuned to reproduce the observed z = 0 relation and show minimal evolution with redshift.

limit to the bulge mass at a given stellar mass in our models. Similar results can be seen in De Lucia et al. (2011).

In contrast, in the model with mergers but no disk instabilities massive galaxies are disk-dominated at high redshifts. The effect of disk instabilities is to form a bulge early, when disks are more turbulent and dynamically unstable. At low masses (lower than $10^{10}\mathrm{M}_{\odot}$) there is no difference between the two models; disk instabilities evidently have little contribution in this mass range in our SAMs.

3.2.4 Size-mass relation

A major prediction of this thesis is the size-mass relation for bulge-dominated galaxies (Figure 3.5). All three models predict a size-mass relationship that closely agrees with the slope, dispersion, and zero-point for low-redshift observations (Shankar et al., 2010) of early-type galaxies in the Sloan Digital Sky Survey, falling within the 1-σ error range for nearly three decades in stellar mass. We emphasize here that the model for bulge sizes is never explicitly tuned to observations; the only free parameters are constrained by hydrodynamical simulations. The fact that we are correctly predicting the local size-mass relation is thus a key finding of the thesis.

For comparison, we also include a version of the model in which $C_{\mathrm{rad}} = 0.0$ for all mergers. This dissipationless model produces galaxies that are too large at all

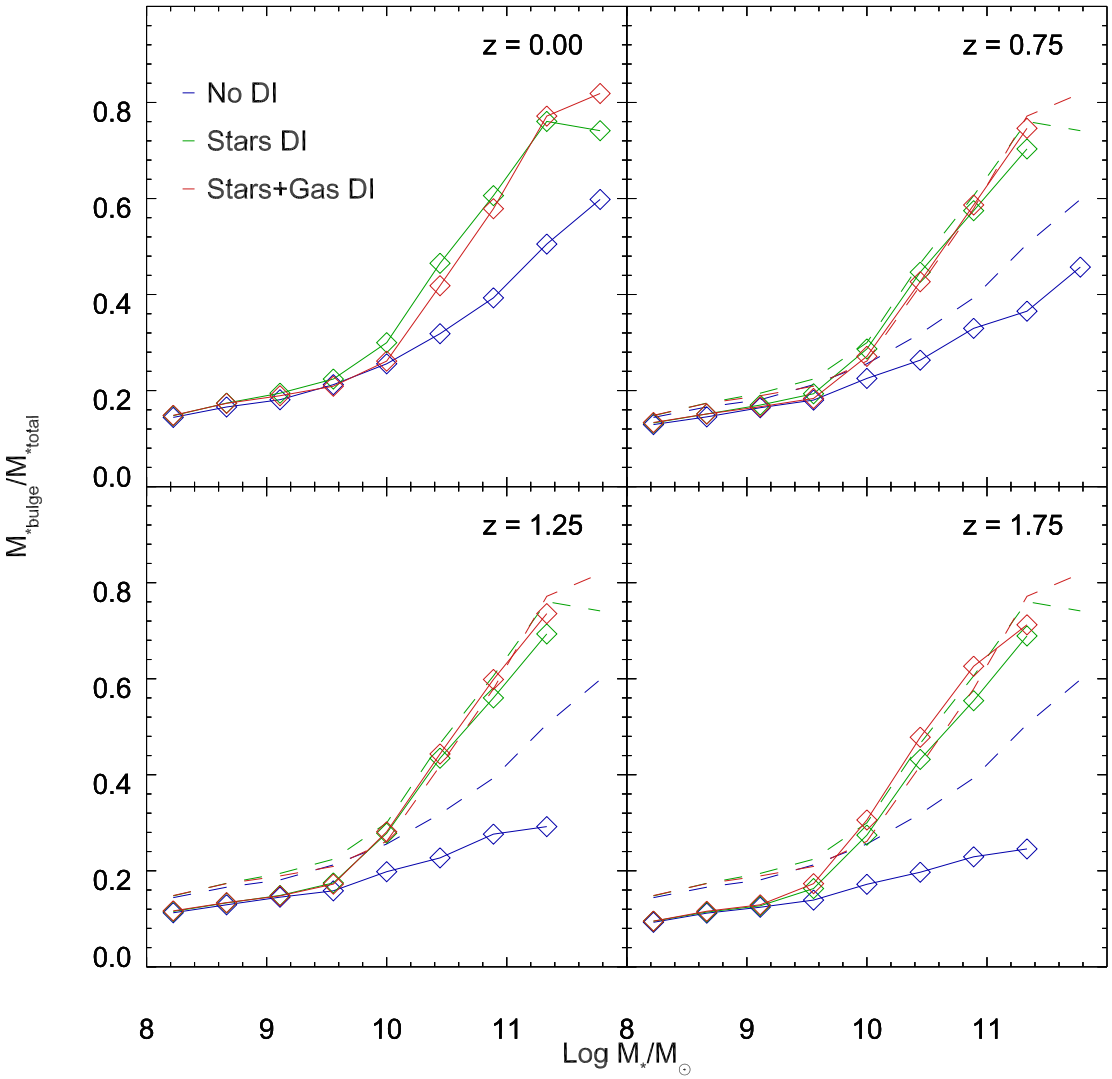

Figure 3.4: Stellar bulge-to-total ratio at redshifts z = 0.0, 0.75, 1.25, and 1.75 for the 'No DI' (blue), 'Stars DI' (green), and 'Stars+Gas DI' (red) versions of the SAM. The dashed lines at higher redshifts indicate the redshift zero relations. More massive galaxies tend to have higher bulge ratios at all redshifts, but bulges tend to form earlier in the models with disk instabilities.

masses, with a size-mass relation that is nearly flat below $10^{10.5}M_{\odot}$. As described above, the amount of dissipation is tied to the amount of gas present in the merger. Since the gas fraction of disk-dominated galaxies increases with decreasing stellar mass (Kannappan, 2004), low-mass bulge-dominated galaxies are more likely to have formed via gas-rich processes. Furthermore, more massive bulge-dominated galaxies are more likely to have undergone subsequent dry mergers, weakening the overall contribution from dissipation. A similar flattening in disagreement with observations can be seen in other SAMs that model bulge sizes without including dissipation (Guo et al., 2011; Shankar et al., 2013).

Having established that our model reproduces the size-mass relationship at redshift zero, we now turn to the evolution of this relation to higher redshifts. Numerous observations (Trujillo et al., 2006; Marchesini et al., 2007; Toft et al., 2007; Williams et al., 2010) have shown that high-redshift quiescent galaxies are more compact than their low-redshift counterparts; here we compare to a recent study by Newman et al. (2012).

Following Newman et al. (2012), we select all galaxies with specific star formation (sSFR) rates less than 0.02 Gyr^{-1}. For consistency with our other figures we also limit the population to bulge-dominated galaxies, although the results do not change if we include all quiescent galaxies. We have converted the Newman et al. (2012) results to a Chabrier IMF to match our SAM. The median size-mass

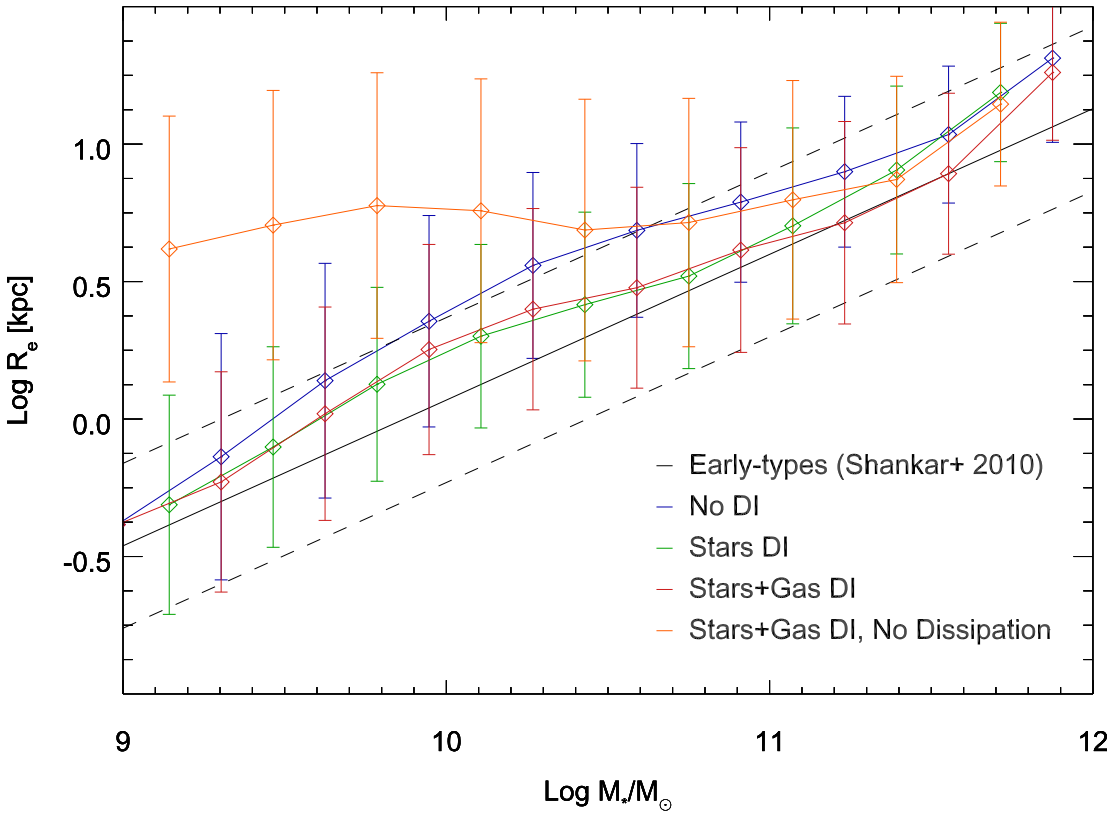

Figure 3.5: Size-mass relation for bulge-dominated galaxies at redshift zero. The blue, green, and red lines show the 'No DI', 'Stars DI' and 'Stars+Gas DI' dissipational versions of the SAM. The orange line shows the median relation for a model in which all mergers are considered to be dissipationless. The error bars represent the 1σ dispersion in the SAM predictions. The black line shows the local relation from Shankar et al. (2010). All dissipational models reproduce the observed scaling, while the dissipationless model produces galaxies that are too large at low masses.

relation at redshifts 0, 0.75, 1.25, and 1.75 is shown in Figure 3.6.

The two DI models of the SAM fall within observational errors for all masses and all redshifts, while the model without DI lies slightly above the $1-\sigma$ errors at redshift 0. We obtain similar results if we compare to Williams et al. (2010), using their evolving sSFR threshold (sSFR < 0.3 t_H, where t_H is the Hubble time at that redshift). Galaxies in the 'No DI' model are larger at all redshifts; in the SAM bulges formed via DI tend to be smaller than bulges formed from mergers (Figure 3.5). Since the stability criterion for the disk depends on its surface density, DI bulges in the SAM tend to form from compact disks at high redshift. Though the DI bulges merge dissipationlessly, they remain relatively smaller even at low redshifts. Further examination of the differences between DI-driven bulges and merger-driven bulges will presented in Chapter 4.

3.2.5 Faber-Jackson relation and the Fundamental Plane

Observations have shown that galaxies also fall on a tight relation between stellar mass and velocity dispersion, termed the Faber-Jackson (Faber & Jackson, 1976, hereafter FJ) relation. While this relation is a power law to the first order (Gallazzi et al., 2006), there are indications that it may be better approximated by a broken power law (Tortora et al., 2009) or a curve (Hyde & Bernardi, 2009; Cappellari et al., 2012), in the sense that more massive galaxies have relatively

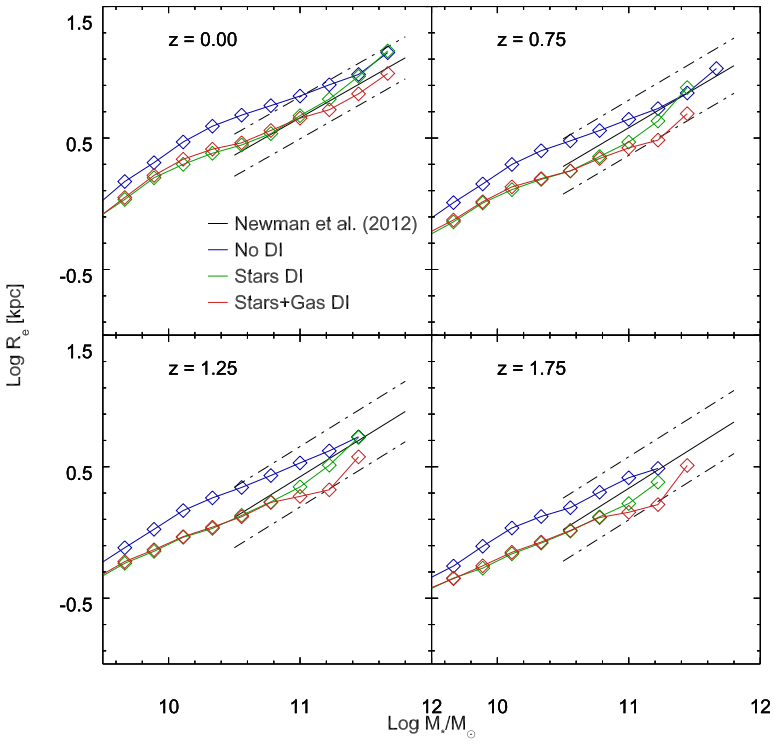

Figure 3.6: Size-mass relation for bulge-dominated quiescent galaxies at redshift 0.0, 0.75, 1.25, and 1.75. The blue, green, and red lines show the 'No DI', 'Stars DI' and 'Stars+Gas DI' dissipational versions of the SAM. The black line shows the observed evolution in the relation Newman et al. (2012). The two DI models fall within the observed error bars for all redshifts and masses, while galaxies in the 'No DI' model are slightly too large at low redshifts.

lower velocity dispersions.

The simulated FJ relation is shown in Figure 3.7. We find that the SAM reproduces the normalization of the relation at redshift zero (Gallazzi et al., 2006). While the high-redshift FJ relation is not yet well-constrained by observations, the SAM predicts that the normalization of the relation increases with redshift, in agreement with observations (Cappellari et al., 2009).

The SAM fully agrees with the predictions of hydrodynamical simulations (Oser et al., 2012) and observations of the evolution of the size-mass and Faber-Jackson relations at fixed stellar mass (Trujillo et al., 2006; Cappellari et al., 2009; Williams et al., 2010; Newman et al., 2012): galaxies at higher redshifts have higher velocity dispersions, but this evolution is much less significant than the evolution in the size-mass relation. Hydrodynamical simulations (Dekel & Cox, 2006; Robertson et al., 2006a; Hopkins et al., 2010) have shown that galaxies that form via gas-rich processes will be compact, with high velocity dispersions. Simple analytic arguments (Naab et al., 2009) predict that dissipationless minor mergers can greatly increase the sizes of early-type galaxies while inducing only minor changes in the velocity dispersion.

In the SAM, this occurs because subsequent minor mergers increase the effective radius of the galaxy, enclosing more diffuse material within the effective radius. Thus the evolution in the velocity dispersion is indicating an evolution

in the central surface density of galaxies. The fact that the SAM reproduces the *magnitude* of the evolution is an indication that the overall SAM prescription (i.e. the merger rate, gas fractions, etc.) is sufficient to reproduce the evolution of galaxy properties to higher redshifts.

While we are reproducing the evolution in the normalization of the FJ relation, we find evidence of a curvature in the opposite direction as local observations. We predict velocity dispersions that are too high in the high-mass regime. This curvature seems to be a robust feature of our model, and we have checked that our results are not biased by a population of extremely compact galaxies, or galaxies too faint to be seen in the local universe.

One possibility is that the discrepancy in the high-mass end stems from variations in the initial mass function. There is a growing body of evidence (Cappellari et al., 2012; Conroy & van Dokkum, 2012; Dutton et al., 2012) showing that early-type galaxies with high stellar masses or high velocity dispersions may have a bottom-heavy IMF (e.g. Salpeter), containing more low-mass stars. Such an IMF would have a higher stellar mass-to-light ratio.

Most observations, such as the Gallazzi et al. (2006) analysis, use stellar luminosities along with stellar population synthesis techniques to infer the stellar mass. Using an IMF that is too top-heavy for high-mass early-type galaxies would tend to overpredict the stellar masses of galaxies with high velocity dispersions:

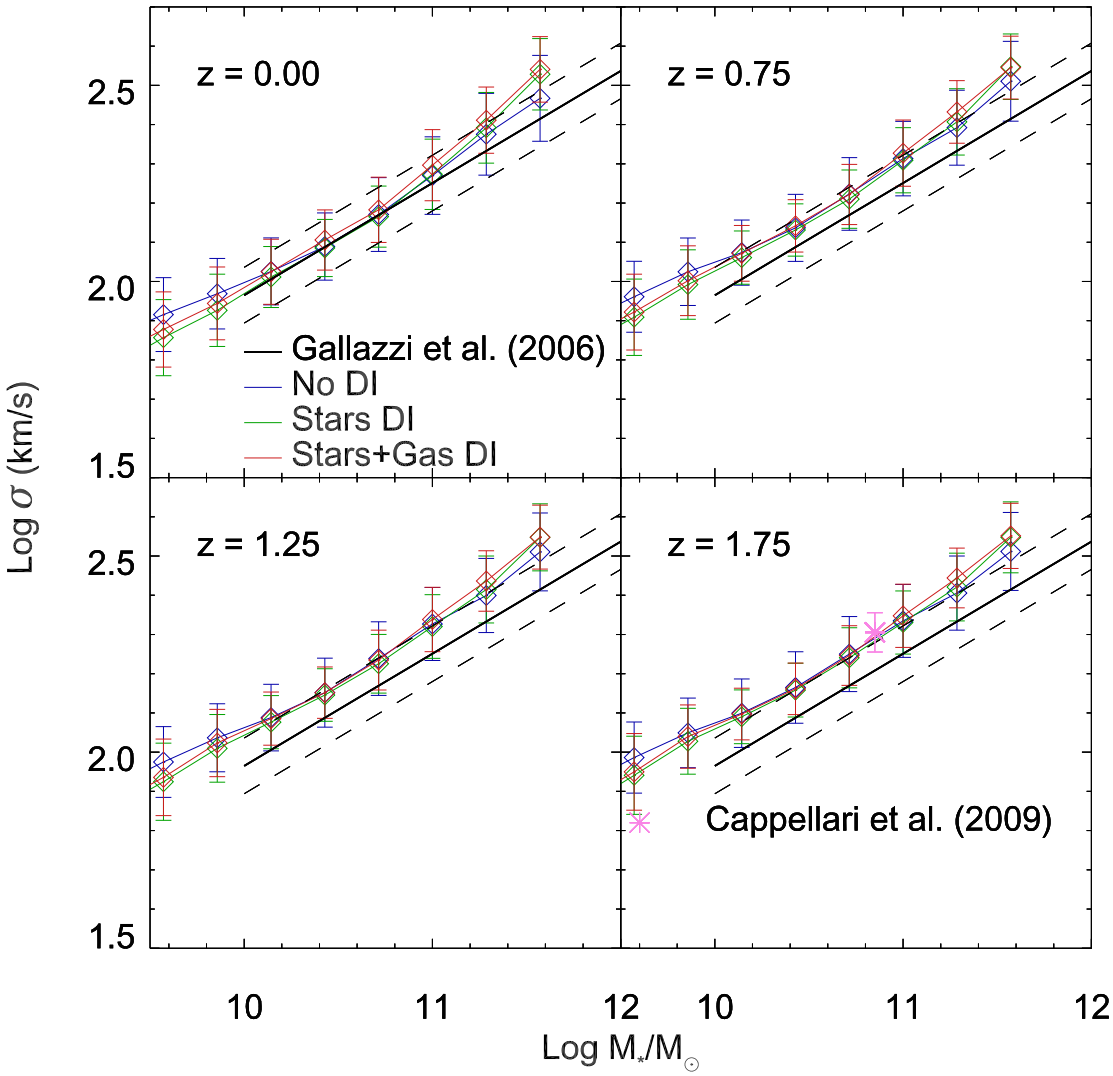

Figure 3.7: Faber-Jackson relation for bulge-dominated galaxies at redshifts z = 0.0, 0.75, 1.25, and 1.75. The blue, green, and red lines show the 'No DI', 'Stars DI' and 'Stars+Gas DI' dissipational versions of the SAM. The black line shows the observed z = 0 relation, with $1-\sigma$ scatter (Gallazzi et al., 2006). The pink star in the lower right panel shows the average observed relation at z $\sim$ 1.6 (Cappellari et al., 2009). While the simulated galaxies match the zero-point of the observed low-redshift relation they display a curvature that is not present in local observations, although this could be offset by changes in the IMF suggested by other observations (Conroy & van Dokkum, 2012). The simulated galaxies agree with observations of the evolution in the normalization of the Faber-Jackson relation at higher redshifts.

(Conroy & van Dokkum, 2012) estimate that stellar mass-to-light ratios for a $\sigma > 300$ kms^{-1} galaxy may be twice that of the Milky Way. Such a correction would lower the high-mass end of the observed FJ relation by a factor of 0.3 dex, in much closer agreement with our model. Furthermore while it is difficult to predict all of the consequences of adopting a more bottom-heavy IMF in the SAM, such an IMF would have a lower instantaneous recycling fraction than the value of 0.43 adopted for the Chabrier IMF. This would have the effect of increasing the masses in our high-mass galaxies; since $\sigma \propto \sqrt{M_*}$ in our model this would shift the high-mass FJ relation in the needed direction.

We now turn to the Fundamental Plane, which we consider in the projection $M_{\rm star} \propto (\sigma^2 R_e)^\alpha$. If all galaxies had the same mass-to-light ratio then one would expect a simple virial scaling, with $\alpha = 2$. However observations (Djorgovski & Davis, 1987; Dressler et al., 1987) have shown that the true FP is tilted from the virial relation, with estimates of the scaling near $\alpha \sim 1.2$ (Pahre et al., 1998; Padmanabhan et al., 2004; Gallazzi et al., 2006). Hydrodynamical simulations (Dekel & Cox, 2006; Robertson et al., 2006b; Covington et al., 2008) have shown that a gradient in gas fraction with respect to stellar mass can induce more dissipation in lower-mass galaxies. These galaxies will have higher concentrations of baryonic matter and lower dark matter fractions within their effective radii, producing a tilt in the Fundamental Plane. Here we examine this tilt in a cosmological context.

As there is some evidence that galaxies with large pseudobulges may have a different FP tilt (Kormendy & Fisher, 2008) and the observations we are comparing to either limit their samples to galaxies with high Sérsic indices or fit galaxies to a de Vaucouleurs n=4 profile, we restrict this analysis to galaxies that have grown at least half of their bulge mass through mergers; in practice this restriction has a minimal effect on the results. In our projection there is no dependence on the stellar mass-to-light ratio; any tilt in the FP comes from variations in the internal structure of the galaxies. We find that the SAM closely reproduces the observed local scaling of $\alpha \approx 1.2$ and, in agreement with observations, the scatter in the FP is smaller than the scatter in either the size-mass or Faber-Jackson relations. We find a slight steepening in the FP at high masses ($M_* > 10^{11.5} \mathrm{M}_\odot$), due to the curvature in the FJ relation. There is no dependence on stellar bulge-to-total ratio or change between the models with and without growth through disk instabilities.

We find only minor evidence of a decrease in the normalization of the FP and slightly stronger evidence of a decrease in the tilt of the FP with redshift. Performing a least-squares linear fit to the FP relation we find a coefficient of $\alpha = 1.21$ at redshift zero, consistent with observations, evolving to $\alpha = 1.11$ at z = 1.75. The evolution of this tilt supports a scenario wherein mergers between disk-dominated galaxies have less dissipation at lower redshifts due to the lower gas content of the progenitors. While subsequent dry mergers are thought to

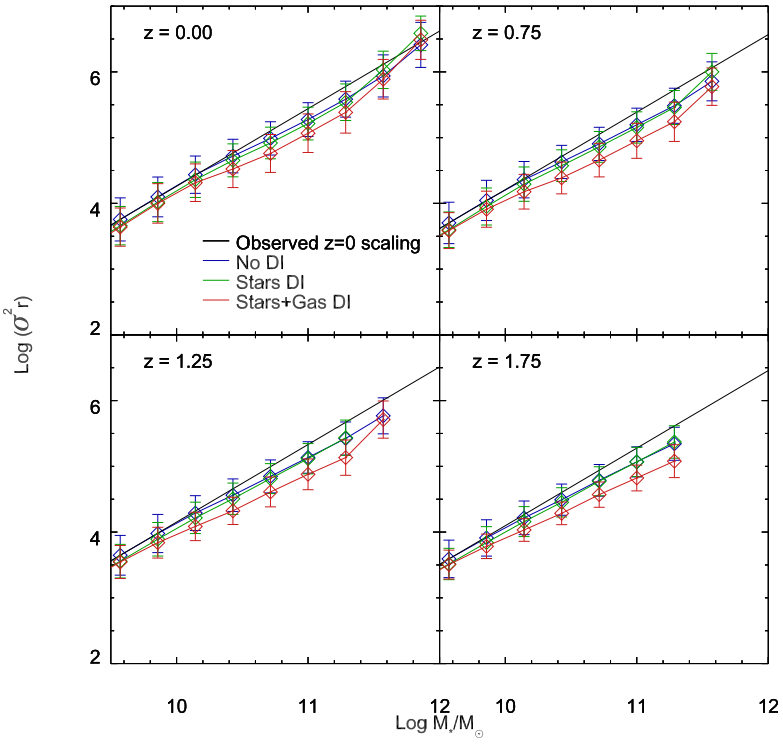

Figure 3.8: Projected Fundamental Plane at redshifts z = 0.0, 0.75, 1.25, and 1.75. The blue, green, and red lines show the 'No DI', 'Stars DI' and 'Stars+Gas DI' dissipational versions of the SAM. Only bulge-dominated galaxies that grew bulges mainly through mergers are shown here (blue lines, with associated 1-sigma error bars). The slope of the FP at each redshift is denoted by α. In the local universe the SAM reproduces the observed tilt of the FP, $\alpha \approx 1.2$, and shows only minor evolution towards higher redshift. Any evolution in the zero-point with redshift is within the 1-sigma errors.

preserve the tilt (Robertson et al., 2006b) induced by the formative event, the population is continuously supplanted with the products of increasingly gas-poor mergers. In this way the tilt of the FP may slowly evolve over time.

3.3 Discussion and Conclusions

We have updated the Somerville et al. (2008a, 2012) semi-analytic model to predict the properties of early-type galaxies, using an analytic model (Covington et al., 2008; Covington et al., 2011) based on hydrodynamical simulations of galaxy mergers (Johansson et al., 2009). These simulations allow us to parameterize the amount of dissipation that occurs during a merger depending on the mass ratio, gas content, size, morphology, and orbit of the progenitor galaxies. This dissipation in turn produces compact bulges from progenitor diffuse disks. The hydrodynamical simulations also show that the velocity dispersion can be determined simply by using the virial theorem, accounting for the amount of dark matter in the center of the galaxy.

Our model is able to reproduce the slope, zero-point, scatter and evolution of the size-mass relation for early-type galaxies. We emphasize that the model has not been tuned to do this; the free parameters in our merger model were instead tuned to agree with hydrodynamical simulations. We note that there have been recent indications that minor mergers alone may not be able to account for all of

the evolution in the size-mass relation, particularly above $z \sim 1$ (Newman et al., 2012; Shankar et al., 2013). A detailed comparison of the methods is beyond the scope of this thesis; however we note the papers previously mentioned only treat gas-poor mergers as dissipationless. The hydrodynamical simulations we use show that mergers between a disk-dominated and a bulge-dominated galaxy are dissipationless as well. Since spiral galaxies tend to be larger than elliptical galaxies at all redshifts, these mergers will greatly increase the effective radii of early-type galaxies, even moreso than mergers between two dry spheroids. In contrast to Newman et al. (2012) we also allow high-redshift bulge-dominated galaxies to regrow a disk; this process may remove some compact early-type galaxies from our population at lower redshifts. In Chapter **??** we show that the growth in the mean size of early-type galaxies is partially driven by the late production of relatively diffuse bulges via mergers.

The model predicts a curvature in the Faber-Jackson relation at high stellar masses that is not seen in observations, but at lower stellar masses we are able to reproduce the slope and normalization of the relation. At higher redshifts we predict an increase in velocity dispersion at fixed mass, in agreement with recent observations. We also are able to match the tilt of the projected Fundamental Plane ($M_* \propto \sigma^2 r$) at redshift zero. We predict a slight decrease in this tilt to higher redshifts; however the magnitude of this change is well within the measurement

errors of high-redshift observations.

We are less certain about our treatment of disk instabilities. Both SAMs and hydrodynamical simulations point to the importance of disk instabilities in forming stellar bulges (Dekel et al., 2009a; De Lucia et al., 2011; Genel et al., 2012a), but the exact mechanisms are poorly constrained at this time. We find that disk instabilities are needed to reproduce the early-type mass function, and that they lead to more efficient bulge formation at higher redshifts. In addition to producing different early-type mass functions at redshift zero, the models with and without disk instabilities predict different evolution in the stellar bulge-to-total ratio over time. These differences represent possible tests of our model of disk instabilities, as high-redshift observations may be able to place further constraints on the model. Despite the differences in morphology, the scaling relations with and without disk instabilities are nearly identical. This may be an artifact of our model: we essentially treat disk instabilities as dissipationless mergers. As disk instabilities are shown to be an important mechanism of bulge formation in SAMs we hope that future surveys and hydrodynamical simulations will be able to provide a deeper understanding of the interaction between the disk and the bulge.

Chapter 4

Simulating the Formation History of Massive Galaxies

4.1 Introduction

While it has long been understood that galaxies in the local universe fall along the Hubble Sequence, it is not yet clear whether this classification extends to higher redshifts, or how this bifurcation between disks and spheroids is formed.The color bimodality between 'red sequence' and 'blue cloud' galaxies is thought to persist to $z \sim 2-3$, with a higher normalization in star formation rate (SFR) (Daddi et al., 2007; Faber et al., 2007; Noeske et al., 2007b; Ilbert et al., 2010; Oesch et al., 2010). High-redshift galaxies have been shown to exhibit structural

characteristics similar to their local counterparts. Star-forming galaxies (SFG) are larger and less centrally-concentrated at fixed stellar mass, while quiescent galaxies (QG) are smaller and have higher Sérsic indices (Williams et al., 2010; Wuyts et al., 2011).

Quiescent galaxies are thought to exhibit more rapid size evolution than star-forming galaxies, in the sense that QG are increasingly more compact than SFG at high redshifts (Trujillo et al., 2006; Toft et al., 2009; Williams et al., 2010; Newman et al., 2012). Several mechanisms have been proposed to account for the growth of these 'red nuggets (Damjanov et al., 2009), including dry and minor mergers (Robertson et al., 2006b; Hopkins et al., 2009b; Naab et al., 2009; Bezanson et al., 2009; Bluck et al., 2012), quasar activity (Fan et al., 2010), and the production of new, more diffuse QG at later times (Cassata et al., 2011).

Recent studies have also attempted to form an evolutionary link between high-redshift compact and quiescent galaxies. Whitaker et al. (2012) identify separate populations of massive blue galaxies with high specific star formation rates (sSFR) alongside massive red galaxies with lower sSFR, suggesting that that these galaxies may be in the process of quenching. A comprehensive analysis (Wuyts et al., 2011) found that galaxies with the highest SFR at any given mass and redshift actually have *higher* Sérsic indices than main-sequence galaxies, suggesting that these galaxies have high amounts of central star formation and may be in the

process of transitioning from disks to spheroids. Further work Barro et al. (2013) showed that these compact, star-forming galaxies have high rates of AGN activity, and that the prevalence of these galaxies declines rapidly with redshift.

Many hydrodynamical simulations have shown that gas-rich processes such as mergers and disk instabilities can produce massive, compact galaxies (Kereš et al., 2005; Robertson et al., 2006a; Cox et al., 2006; Hopkins et al., 2009b; Dekel et al., 2009b). Taken together with observations, Barro et al. (2013) suggest a scenario in which a portion of high-redshift ($z \gtrsim 2-3$) disk-dominated galaxies undergo high amounts of central star formation, becoming compact spheroids ('blue nuggets'). These galaxies would quench rapidly, becoming 'red nuggets' at intermediate redshifts ($z \approx 1-2$) before growing in both size and mass due to minor mergers, evolving onto the local red sequence.

In this chapter we use the GF SAM to study the processes that form blue nuggets, as well as how they evolve at later redshifts. We include mechanisms for predicting the sizes, masses, and SFR for galaxies, and use them to determine the relative importance of quiescent star formation, mergers, and disk instabilities (DI) in producing disk-dominated and bulge-dominated galaxies.

In Section 4.2 we examine the size-mass and sSFR-surface density relations for a volume-limited subset of the galaxy population across a range of redshifts. We find that the simulated galaxies roughly reproduce the observed size evolution

of disk-dominated and bulge-dominated galaxies out to z=2.5. In Section 4.3 we examine the evolutionary histories of individual galaxies, binned according to their morphologies and peak central surface densities. We show that bulge-dominated galaxies that ever become 'blue nuggets' have unique formation histories: they form rapidly, remain relatively compact, and quench at high redshifts. We discuss the implications of our work in Section 4.4.

In general, mergers between gas-rich disk-dominated galaxies will produce a compact, bulge-dominated remnant, and mergers between two gas-poor bulge-dominated galaxies will produce a diffuse bulge-dominated remnant. In this chapter we term all mergers that produce a remnant with a *smaller* half-mass radius than the more massive progenitor as 'dissipative', and mergers that produce a *larger* remnant as 'dissipationless'. While the prescription for calculating the half-mass radius following mergers is based upon the results of hydrodynamical simulations, the DI prescription has not been explicitly measured; this remains the most uncertain prediction of our model.

4.1.1 Selection Criteria

We present two sets of results: the first were drawn from 48 $(50\ h^{-1})^3$ subvolumes of the Bolshoi simulation. In these results we include all galaxies higher than $10^8 M_\odot$ at the desired redshift. In section 4.3 we examine the formation his-

tory of randomly-selected galaxies; these galaxies were drawn from the population of massive ($\geq 10^{10}\mathrm{M}_{\odot}$) galaxies in one $(50\ h^{-1})^3$ subvolume that are present at redshift zero. All results were produced using the 'Stars + Gas DI' version of GF, which incorporates bulge growth from stellar- and gas-triggered disk instabilities.

Following Barro et al. (2013) we use the threshold $\log(M/r_e^{\alpha} < 10.3\,\mathrm{M}_{\odot}\,\mathrm{kpc}^{-\alpha})$ to separate compact galaxies from diffuse galaxies; this scaling is similar to the observed slope of the early-type size-mass relationship (Newman et al., 2012). We classify galaxies as quiescent or star-forming using a sSFR threshold of $10^{-0.5}\mathrm{Gyr}^{-1}$. Using these two criteria, all galaxies fall into one of four categories at any redshift: diffuse star-forming galaxies (dSFG), compact star-forming galaxies (cSFG, 'blue nuggets'), diffuse quiescent galaxies (dQ), and compact quiescent galaxies (cQ, 'red nuggets').

4.2 Evolution of the Galaxy Population

We first show the size evolution of galaxies from redshift 2.5 to redshift zero (Figure 4.1). Comparing to observations, we find that the simulated galaxies roughly match the observed mean size-mass relation for both disk-dominated (Trujillo et al., 2006) and bulge-dominated (Newman et al., 2012) galaxies out to redshift z = 2.5. At every redshift interval the average disk-dominated galaxy at fixed stellar mass is larger than the average bulge-dominated galaxy. Bulge-

dominated galaxies also show greater evolution with redshift: the average size of a $10^{10} - 10^{10.5}\mathrm{M}_{\odot}$ bulge-dominated galaxy increases by a factor of 3.06 from z = 2.5 to z = 0, while a disk-dominated galaxy of similar mass only increases by a factor of 0.20. The difference in the magnitude of the size evolution is prominent enough that, in the redshift interval $1.5 < z < 2.5$ the population of galaxies displays a clear bimodal distribution of diffuse disk-dominated galaxies and compact bulge-dominated galaxies.

Further correlations can be seen when galaxies are separated according to whether they ever undergo a 'blue nugget' phase. While disk-dominated 'blue nugget' galaxies tend to be randomly distributed, bulge-dominated 'blue nuggets' are to be smaller at all redshifts than non-blue nugget galaxies. These blue nugget galaxies also show less evolution in mean size. The most compact galaxies tend to remain relatively compact at all redshifts. Instead the size evolution of bulge-dominated galaxies is led by the appearance of diffuse bulge-dominated galaxies at lower redshifts. now examine the evolution in surface density and specific star formation rate (Figure 4.2). For comparison with the previous figures we limit the sample to galaxies more massive than $10^{9.5}\mathrm{M}_{\odot}$. Comparing the average sSFR, we note that both disk-dominated and bulge-dominated galaxies have less efficient star formation at lower redshifts, in agreement with several observations (Noeske et al., 2007a; Wuyts et al., 2011; Barro et al., 2013). At all redshifts bulge-

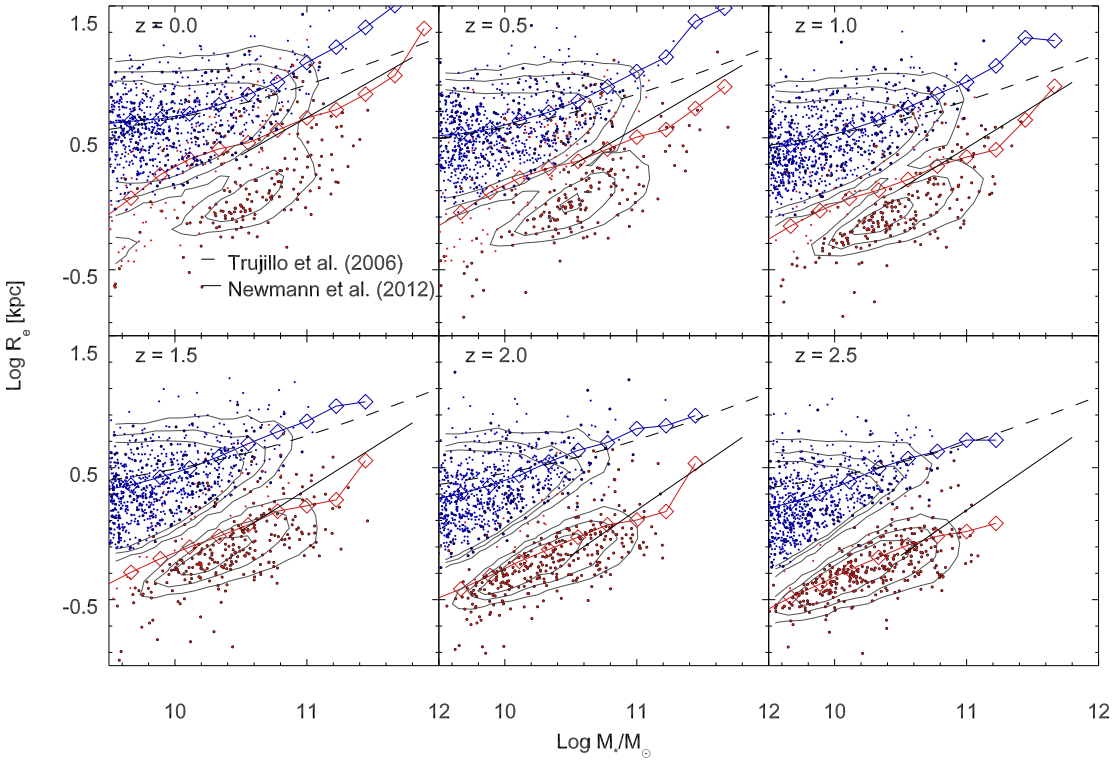

Figure 4.1: Evolution of the size-mass relationship from redshift z=0.0 (top left panel) to z = 2.5 (bottom right panel). The solid blue (red) lines show the mean relation for disk-dominated (bulge-dominated) galaxies in each redshift bin. The blue and red points show 1,000 randomly-chosen galaxies, with blue points indicating disk-dominated galaxies and red points indicating bulge-dominated galaxies. Points with a black outline show the subset of galaxies that ever undergo a 'blue nugget' phase. The dashed and solid lines indicate the observed size-mass relation for disk-dominated Trujillo et al. (2006) and bulge-dominated galaxies Newman et al. (2012). Bulge-dominated galaxies tend to be smaller at fixed stellar mass than disk-dominated galaxies, and display greater evolution with redshift. In every redshift bin, bulge-dominated 'blue nugget' galaxies are systematically smaller than 'non-blue nugget' galaxies.

dominated galaxies are more compact than disk-dominated galaxies: less than 1% of the galaxies in the compact quadrants are disk-dominated at any redshift. This difference is also reflected in the lower zero-point in the size-mass relationship.

In agreement with Barro et al. (2013) we find a rapid decrease in number density of compact star-forming galaxies with redshift. At z = 2.5 43.0% of all galaxies (and 67.5 % of bulge-dominated galaxies) are cSFG; by z = 1.5 the proportion has dropped to 10.2%, and by z=0.5 the less than 1% of galaxies are cSFG. The proportion of compact quiescent galaxies increases from 5.6% at z = 2.5 to 26.9% at z = 1.5, and drops to 12.3% at redshift zero. The proportion of diffuse quiescent galaxies mirrors that of the cSFG, rising from 5.6% at z= 2.5 to 86.3% at z=0.

These changes in number density point to two evolutionary trends. At high redshifts disk-dominated galaxies and bulge-dominated galaxies have similar specific star formation rates, while bulge-dominated galaxies are more compact. Progressing to lower redshifts, bulge-dominated galaxies become more diffuse overall and quench, while disk-dominated galaxies have higher star formation efficiencies and less evolution in surface density. Among bulge-dominated galaxies, 'BN' galaxies are more compact than 'non-BN' galaxies, even at low redshifts.

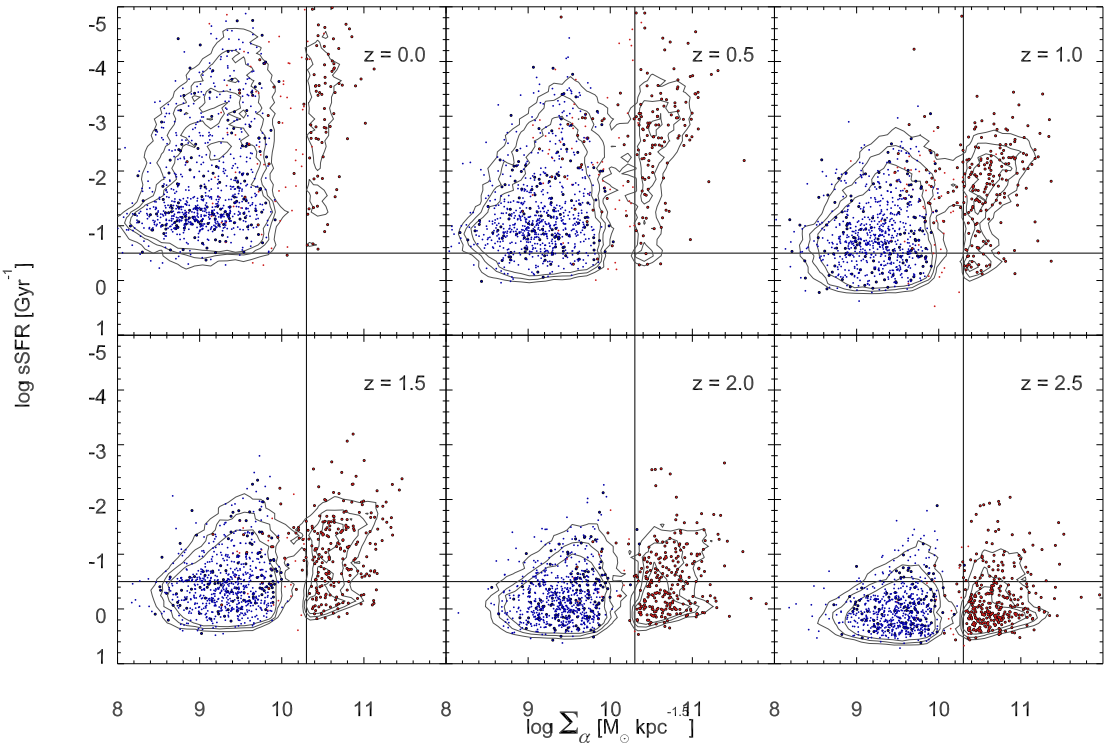

Figure 4.2: Specific star formation rate (sSFR) vs. Σ_α for disk-dominated (blue) and bulge-dominated (red) galaxies at redshifts z = 0.0, 0.5, 1.0, 1.5, 2.0, and 2.5. The sizes of 1,000 randomly-chosen galaxies are shown. Points with a black outline show the subset of galaxies that ever undergo a 'blue nugget' phase. The solid lines indicate the threshold separating diffuse galaxies from compact galaxies (vertical) and quiescent galaxies from star-forming galaxies (horizontal) from Barro et al. (2013). The proportion of galaxies lying within each quadrant is shown.

4.3 Evolution of individual galaxies

In the previous section we restricted our analysis to volume-limited snapshots, mimicking what might be observed at distinct redshifts. However the advantage of a semi-analytical model is that we can track the full formation history of any galaxy, enabling us to detail why specific correlations arise. Having established that bulge-dominated and disk-dominated galaxies occupy separate regions in the size-mass and sSFR-surface density planes, we now turn to the evolutions of individual galaxies.

We first examine the evolution of galaxies in the size-mass plane. In this analysis we have randomly selected 15 disk-dominated, non-BN bulge-dominated, and BN bulge-dominated galaxies that are more massive than $10^{10}M_{\odot}$ at redshift zero. The evolutionary tracks, along with the z=0 location, are shown in Figure 4.3.

Disk-dominated galaxies appear to have a rather uniform formation history, with a gradual yet steady increase in size. A few of the galaxies experience a rapid shrinking in size – presumably these galaxies underwent major mergers, formed compact bulges, and then regrew a massive disk.

The size evolution for nBN bulges is similar to that of disks for much of the mass range. At some point above $\sim 10^{9}M_{\odot}$ however most of these galaxies experience a rapid decrease in size along with an increase in mass, which is often

followed by a rapid increase in both size and mass. As we will show, these changes are the result of gas-rich and gas-poor mergers, respectively. By redshift zero the nBN bulges are more compact than the disks on average.

The size evolution for BN bulges is the most interesting. Even at $10^7 M_\odot$, BN galaxies are more compact than the other two categories, suggesting that these galaxies have structural differences early in their formation. These galaxies tend to grow steadily, experience one or several near-instantaneous decreases in size, and then continue to grow. At redshift zero these galaxies are more compact than both the disks and the nBN bulges. Most of these galaxies do not exhibit the jumps in both size and mass that characterized mergers in the nBN bulges.

We next turn to the evolution of the same randomly-selected galaxies in the sSFR-surface density plane (Figure 4.4). Comparing the evolution of all three populations, we find that the galaxies originate as diffuse galaxies with high sSFR. All three populations begin by experiencing a gradual rise in surface density accompanied by a gradual fall in sSFR. In most of the disk galaxies, this growth phase eventually slows as galaxies begin to quench. Few of the galaxies experience significant changes in surface density after they enter the dQ quadrant.

nBN bulges experience more turbulent growth. Following the steady phase of increasing surface density and decreasing sSFR, these galaxies have rapid increases in both surface density and star formation efficiency, as one might expect during

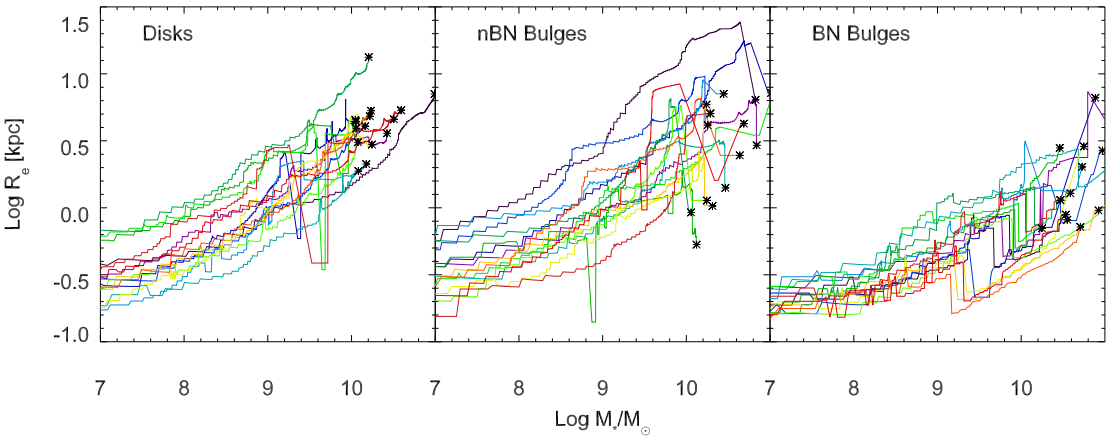

Figure 4.3: Size-mass evolution of simulated galaxies. From left, the panels show the evolution of 15 randomly-selected disks, non-BN bulges, and BN bulges. Black stars show the positions of the galaxies at redshift zero. Most disk-dominated galaxies show a steady increase in radius with time and a shallow turnover in SFR at high stellar masses. Bulge-dominated galaxies tend to be smaller at fixed stellar mass and have sharper turnovers in SFR. Bulge-dominated cSFG have the noisiest size evolutions, with many galaxies undergoing a rapid decrease in size followed by a regrowth.

a gas-rich merger. These galaxies then quench rapidly, with a steep drop in sSFR and almost no change in surface density. Several of the galaxies experience large decreases in surface density while already being classified as quiescent; as we will show these jumps are due to dissipation less mergers. At redshift zero these galaxies are more compact than the disk galaxies, with lower sSFR.

BN bulges originate with the highest sSFR and follow the same steady growth phase as disks and nBN bulges. However around $\log \Sigma_\alpha = 9.5$ these galaxies all undergo a large increase an surface density, pushing them into the cSFG quadrant. In contrast to the nBN bulges, there is no accompanying increase in sSFR. This rapid increase is generally followed by a more gradual increase in surface density

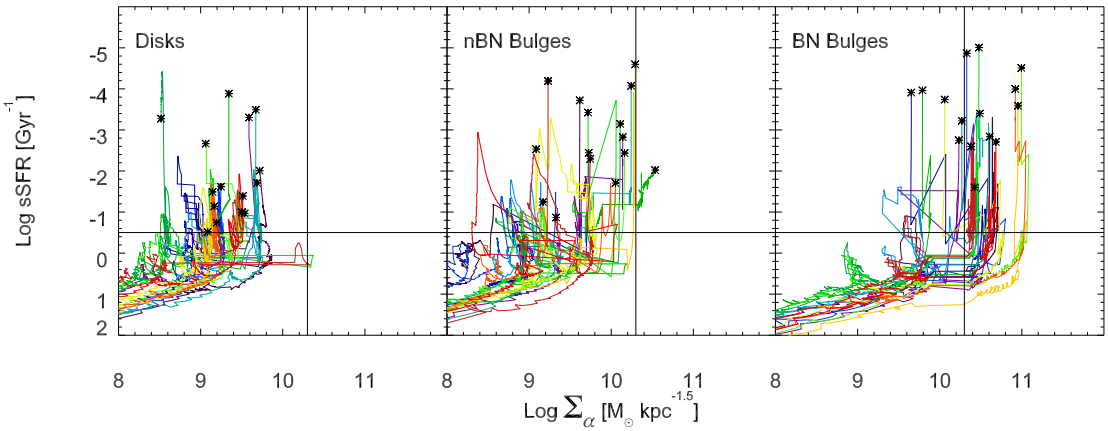

Figure 4.4: sSFR-surface density evolution of simulated galaxies. From left, the panels show the evolution of 15 randomly-selected disks, non-BN bulges, and BN bulges. Black stars show the positions of the galaxies at redshift zero. While disk galaxies have relatively steady evolution, nBN bulges exhibit rapid jumps in both sSFR and surface density, which are indicative of mergers. BN bulges show rapid increases in surface density with almost no change in sSFR.

along with a gradual decrease in sSFR. Eventually the galaxies quench, with a sharp decrease in sSFR. BN bulges are the most compact galaxies, with most falling in the cQ quadrant at redshift zero.

4.3.1 The importance of mergers and DI

The differences between the size-mass and sSFR-surface density paths for these three categories of galaxies indicate different evolutionary processes that contribute to the growth of massive galaxies. In the following section we focus our analysis on the growth of individual galaxies. As noted in section 2, galaxy growth occurs in one of three ways: through the quiescent accretion of cold gas onto the disk; through disk instabilities, which transfer a small amount of stars

and gas from the disk to the bulge; and through mergers, which can destroy much of the disk and form a massive bulge.

In Figure 4.5 we show the tracks of five disk-dominated galaxies in the size-mass and sSFR-surface density planes. For each galaxy, we highlight the positions in which mergers and DI have occurred. We find that these galaxies have relatively quiet formation histories, with little growth coming from mergers or DI. On average, 77% of the stellar mass was formed quiescently, 18% was formed during or transferred to the bulge during a merger, and 5% was formed in or transferred to the bulge in a DI.

Figure 4.6 performs the same analysis for nBN bulges. We find that most of these galaxies become bulge-dominated through merger events, as opposed to through DI. This is reflected in the composition of the stars at redshift zero: on average, 26% of the stellar mass was formed quiescently, 64% was formed during or transferred to the bulge during a merger, and 7% was formed in or transferred to the bulge in a DI. Comparing the size-mass and sSFR-surface density relations, we confirm that the large changes in both of these relations step from merger events. Dissipative mergers tend to lead to large increases in surface density and sSFR, along with large decreases in effective radius. Dissipationless mergers produce small increases in stellar mass and effective radius, but have little effect on sSFR or surface density.

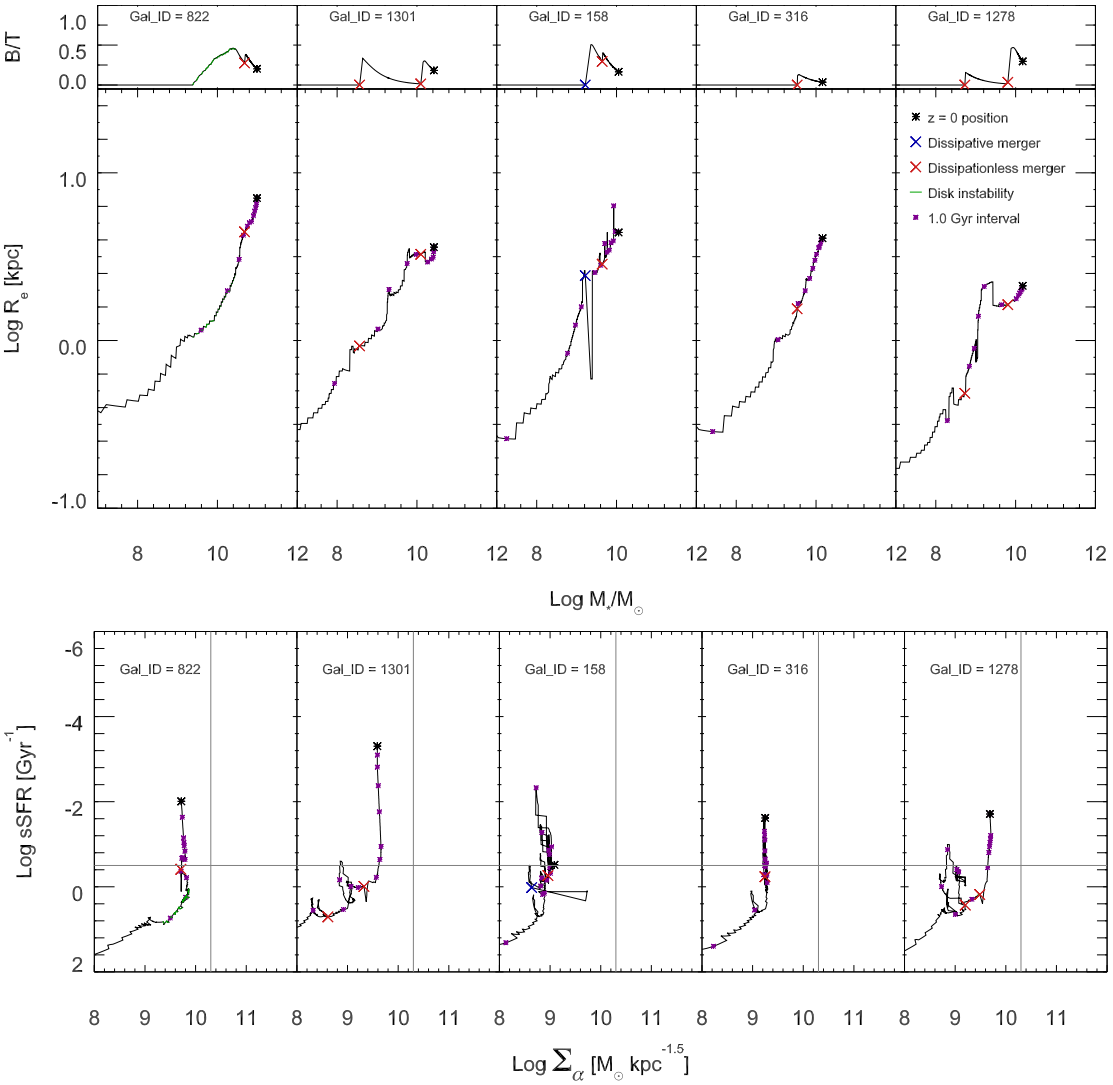

Figure 4.5: The evolution of five randomly-selected disk-dominated z=0 galaxies in bulge-to-total ratio, size-mass (top) and sSFR-surface density (bottom) planes. Vertical panels show the same galaxy. Purple crosses show time intervals of 1.0 Gyr. Blue and red crosses indicate gas-rich and gas-poor mergers, respectively. Green lines show timesteps in which the galaxy was undergoing a DI. Black crosses indicate the z=0 positions. Disk galaxies have relatively quiet formation histories, with steady increases in star formation and stellar mass due to quiescent cooling of hot gas.

We note that the majority of these galaxies become bulge-dominated rather late, typically within the past 1 Gyr. The emergence of this class of relatively diffuse bulges is thus a key driver of the evolution in the size-mass relationship. While late minor mergers have been shown to increase the sizes of bulge-dominated galaxies (Naab et al., 2009; Oser et al., 2010) nBN galaxies, in our model only 34% of nBN galaxies experience a minor merger after becoming bulge-dominated.

The BN bulges have formation histories that are dominated by DI, rather than mergers 4.7. 58% of BN bulges are experiencing a DI when they enter the cSFG quadrant. In contrast to the nBN galaxies, these galaxies become bulge-dominated at low stellar masses, presumably due to the increased importance of DI at high redshifts. Being the most compact galaxies at any given mass, when these galaxies experience mergers they are more likely to increase in size. This accounts for part of the size- and surface density-evolution of bulge-dominated galaxies seen in Figures 4.1 and 4.2.

4.3.2 The mass accretion history

The fact that BN galaxies have the highest sSFR at fixed surface density, and become bulge-dominated at low stellar masses, would seem to indicate that they have accelerated formation histories. We confirm this in Figure 4.8, in which we

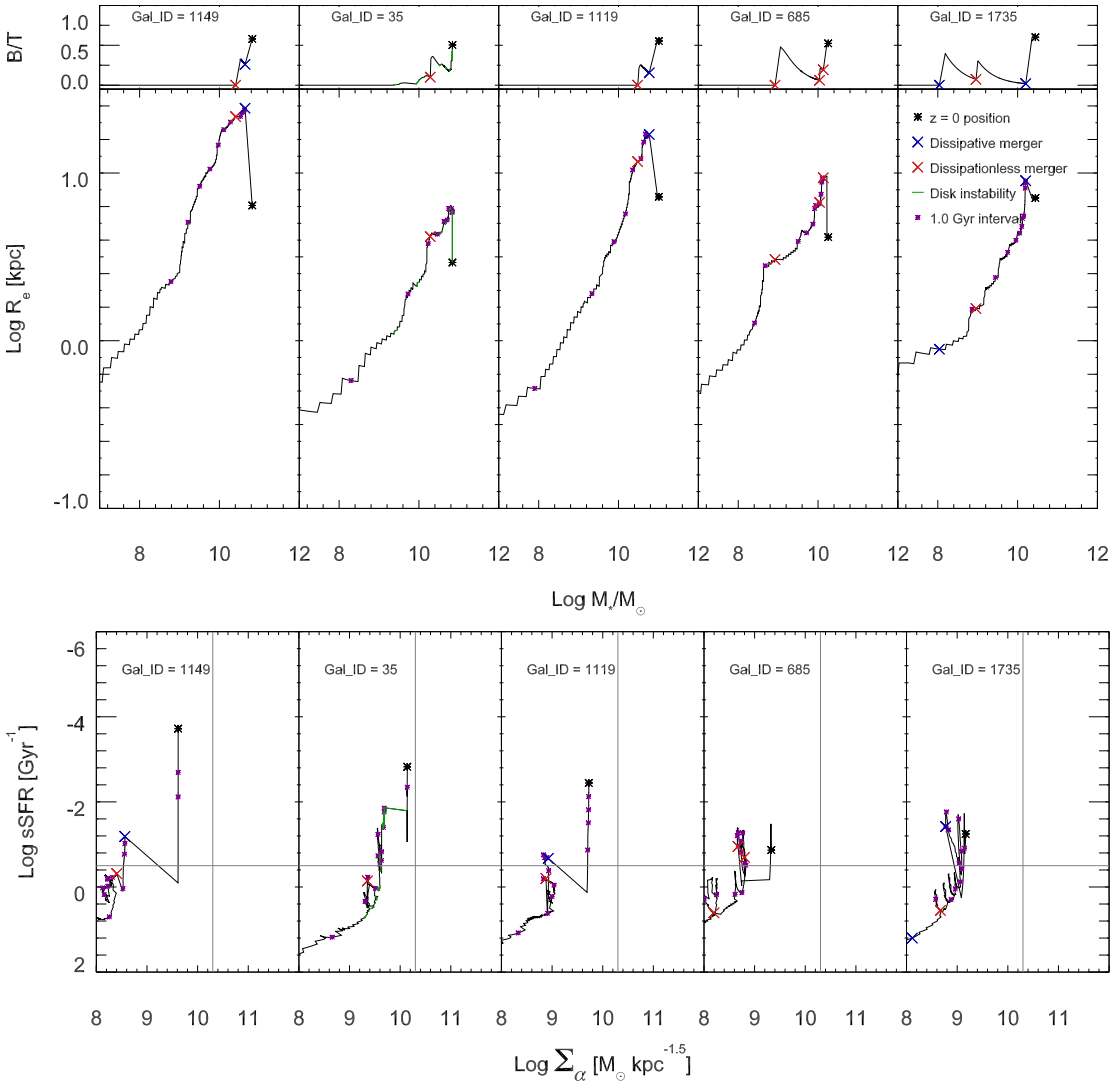

Figure 4.6: The paths of five randomly-selected nBN bulge-dominated z=0 galaxies in the size-mass (top) and sSFR-surface density (bottom) planes. Top and bottom panels show the same galaxy. yellow crosses show time intervals of 1.0 Gyr. Blue and red crosses indicate gas-rich and gas-poor mergers, respectively. Green lines show timesteps in which the galaxy was undergoing a DI. Black crosses indicate the z=0 positions. nBN galaxies experience rapid changes in structural properties and sSFR due to dissipationless mergers.

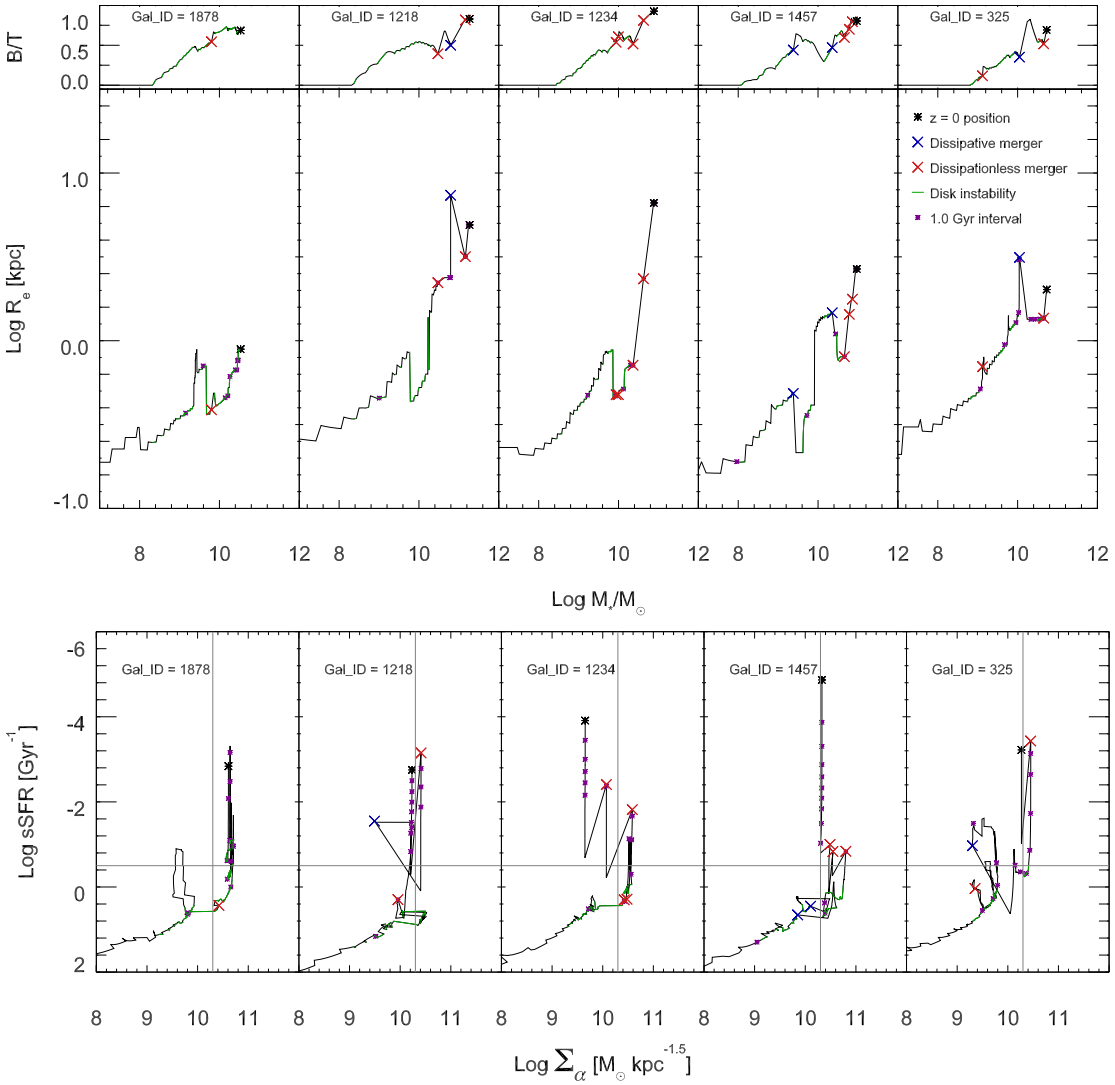

Figure 4.7: The paths of five randomly-selected BN bulge-dominated z=0 galaxies in the size-mass (top) and sSFR-surface density (bottom) planes. Top and bottom panels show the same galaxy. yellow crosses show time intervals of 1.0 Gyr. Blue and red crosses indicate gas-rich and gas-poor mergers, respectively. Green lines show timesteps in which the galaxy was undergoing a DI. Black crosses indicate the z=0 positions. While BN galaxies experience both dissipational and dissipationless mergers, most BN become compact due to DI.

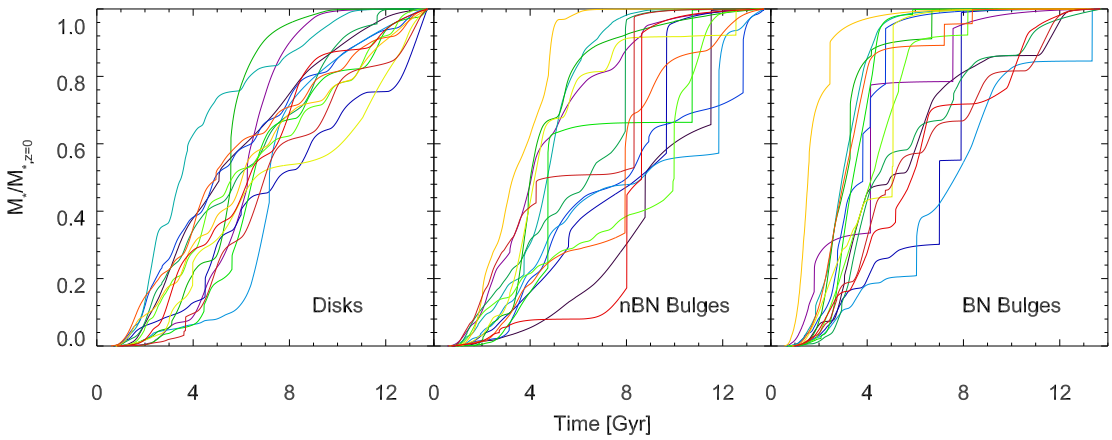

Figure 4.8: The stellar mass of galaxies as a function of the stellar mass at redshift zero. From left, the panels show the evolution of 15 randomly-selected disks, non-BN bulges, and BN bulges. Black stars show the positions of the galaxies at redshift zero. Disk galaxies have steady mass accretion histories, while nBN galaxies have large increases in mass due to mergers. BN galaxies display some of the characteristics of mergers but also have accelerated formation histories.

examine the mass accretion histories of 15 randomly-chosen disk, BN, and nBN galaxies. While disk galaxies have slow, steady accretion, BN galaxies form much of their mass early; one of the galaxies actually forms 90% of its final stellar mass within the first 3 Gyr. nBN galaxies have mass accretion histories that are similar to disk galaxies at early times, but have sharp discontinuities indicative of major mergers later on.

We reiterate that these randomly-selected galaxies are all in the same mass range at redshift zero; thus as we examine higher redshifts the BN galaxies are likely to be the most massive. Put another way, the evolution in the red sequence of massive galaxies is partially driven by the new appearance of merger-driven new nBN galaxies.

Table 4.1: Summary of differences between disks, 'blue nugget' bulges, and 'non-blue nugget' bulges at redshift zero. Measured quantities are for galaxies between $10^{10} - 10^{10.5} M_{\odot}$ at redshift zero.

Measurement (z = 0)	Disks	Non-BN bulges	BN bulges	All bulges
Mass ($10^{10} M_{\odot}$)	1.76 ± 0.29	1.95 ± 0.32	2.17 ± 0.32	2.07 ± 0.32
Size (kpc)	5.15 ± 1.71	3.35 ± 1.19	1.67 ± 0.80	2.46 ± 1.09
sSFR (Gyr^{-1})	0.06 ± 0.04	0.04 ± 0.04	0.02 ± 0.03	0.03 ± 0.04
Σ_{α} (10^9 $M_{\odot} kpc^{-1.5}$)	2.44 ± 0.87	9.19 ± 4.13	30.1 ± 14.2	19.8 ± 11.7

4.4 Discussion and Conclusion

We have presented the formation and assembly histories of massive galaxies within a semi-analytic model. By including mechanisms for passive star formation, mergers, and disk instabilities we are able to calculate the sizes, surface densities, masses, and star formation rates at any redshift.

On average, we find that bulge-dominated galaxies and disk-dominated galaxies agree with the observed size-mass relation from z=0 to z=2.5. Bulge-dominated galaxies however fall into two broad categories, depending on whether they ever can be classified as 'blue nuggets,' compact galaxies with high amounts of star formation. We summarize the differences between 'blue nuggets', 'non-blue nuggets', and disk-dominated galaxies in Tables 4.1, 4.2 and 4.3.

The structural and evolutionary differences between these galaxies seem to be indicative of different formation histories. To summarize while disks and 'non-

Table 4.2: Summary of differences between disks, 'blue nugget' bulges, and 'non-blue nugget' bulges at redshift 2.5. Measured quantities are for galaxies between $10^{10} - 10^{10.5} M_{\odot}$ at redshift zero.

Measurement (z = 2.5)	Disks	Non-BN bulges	BN bulges	All bulges
Mass ($10^{10} M_{\odot}$)	0.19 ± 0.09	0.23 ± 0.11	0.48 ± 0.25	0.36 ± 0.21
Size (kpc)	1.39 ± 0.41	1.35 ± 0.43	0.89 ± 0.34	1.10 ± 0.41
sSFR (Gyr^{-1})	1.92 ± 0.67	1.95 ± 0.61	1.98 ± 0.71	1.97 ± 0.66
Σ_{α} (10^9 $M_{\odot} kpc^{-1.5}$)	3.15 ± 1.01	1.90 ± 1.05	23.1 ± 3.27	13.1 ± 2.43

Table 4.3: Summary of formation histories for disks, 'blue nugget' bulges, and 'non-blue nugget' bulges. Measured quantities are for a $10^{10} - 10^{10.5} M_{\odot}$ galaxy. 'Quiescent' stellar mass refers to mass that has never interacted in a merger or DI. 'DI' mass refers to the portion of stars that were formed or transferred to the bulge in a DI. 'Merger' mass refers to the portion of stars that were formed or transferred to a bulge in a merger.

Measurement	Disks	Non-BN bulges	BN bulges	All bulges
Time at which 50% of stars have formed (Gyr)	6.25 ± 0.86	6.16 ± 1.17	4.83 ± 1.02	5.46 ± 1.14
Time at which 90% of stars have formed (Gyr)	10.67 ± 0.98	8.74 ± 1.41	7.64 ± 1.46	8.16 ± 1.47
Proportion of 'quiescent' stellar mass at z=0	0.79 ± 0.07	0.32 ± 0.06	0.32 ± 0.06	0.32 ± 0.06
Proportion of 'merger' stellar mass at z=0	0.17 ± 0.06	0.59 ± 0.10	0.52 ± 0.10	0.56 ± 0.10
Percentage of stellar mass formed in DI	0.05 ± 0.03	0.09 ± 0.07	0.16 ± 0.07	0.12 ± 0.07

blue nuggets' are structurally similar at high redshifts, 'blue nuggets' tend to have the highest sSFR. These high sSFR produce unstable disks which then collapse via disk instabilities, forming massive, compact spheroids. As the most massive galaxies at a given redshift, 'blue nuggets' quench early. Being the most compact galaxies, 'blue nuggets' are the most likely to increase in size following a merger.

'Non-blue nuggets' become bulge-dominated and compact at later redshifts, through dissipative mergers. While we emphasize that further research needs to be done to fully characterize the relative sizes of bulges resulting from mergers and DI, in this model merger-driven bulges are less compact than their DI-driven counterparts. Given their more extended formation histories, the rapid size evolution of massive galaxies is at least partially the result of the formation of these more extended galaxies at later redshifts.

Observations (Barro et al., 2013) have linked high-redshift compact star-forming galaxies with increased AGN activity, while also suggesting that this activity may not be due to major mergers (Kocevski et al., 2012). We have not examined the AGN luminosities of the galaxies in this thesis, but we do note that cSFG in the model are formed via DI, which also fuel the central black hole. In future work we aim to study the AGN activity of simulated compact star-forming galaxies. In addition, we hope to explicitly test the predictions of the model against a suite of hydrodynamical cosmological simulations.

Chapter 5

Simulating Early-Type Galaxy Age and Metallicity Across and Through the Fundamental Plane

5.1 Introduction

Early type galaxies can be described by a two-dimensional plane relating effective radius ($R_{\rm e}$), central stellar velocity dispersion (σ), and effective surface brightness ($I_{\rm e}$), termed the fundamental plane (FP) (Djorgovski & Davis, 1987; Dressler et al., 1987; Faber et al., 1987). This plane is tilted from the plane one would expect from a simple application of the virial theorem, indicating that fur-

ther processes, such as non-homology or a varying mass-to-light ratio, must have an effect (Jørgensen et al., 1996). Furthermore, the fundamental plane is not an exact relation; galaxies have a degree of scatter around the FP, in effect making the fundamental plane 'thick'. Observations indicate that this scatter increases with redshift, particularly among less massive galaxies (Treu et al., 2005b).

More specifically, while the slope of the FP appears unchanged for high-mass ellipticals since $z \sim 1$, low-mass ellipticals at high redshifts have higher surface brightnesses than their effective radii and velocity dispersions would seem to predict (van der Wel et al., 2004; Treu et al., 2005a,b; Jørgensen et al., 2006; van Dokkum & van der Marel, 2007). If we consider a projected FP, where surface brightness is the dependent parameter, then these low-mass galaxies tend to lie above the mean FP (i.e. they are brighter than average) relation at high redshift, and to fall onto the FP over time.

There are indications that this residual thickness in the FP correlates with the stellar population age. Forbes et al. (1998) and Terlevich & Forbes (2002) found that galaxies with higher residual surface brightnesses are younger than those that lie near the mid-plane of the FP; conversely, those with lower residual surface brightnesses are older.

More recently, observations from the Sloan Digital Sky Survey (SDSS) have been used to analyze stellar population trends both within the R-σ projection of

the FP, and through the thickness of the FP, using residual surface brightnesses (Graves et al., 2009a,b, 2010; Graves & Faber, 2010). By stacking spectra of galaxies with similar stellar properties and measuring the Lick indices on those spectra, the authors were able to derive [Fe/H],[Mg/H], [Mg/Fe], and stellar age for a population of passive early-type galaxies. In agreement with Forbes et al. (1998) and Terlevich & Forbes (2002), Graves et al. (2009b, hereafter G09) found that younger galaxies lie above the FP, and have relatively higher surface brightnesses, while older galaxies lie below it. Galaxies above the FP also tended to have higher [Fe/H] and [Mg/H], and lower [Mg/Fe]. G09 also determined that age, [Fe/H], [Mg/H], and [Mg/Fe] increase with velocity dispersion throughout the FP, independent of the residual surface brightness. These same properties are almost independent of $R_{\rm e}$, indicating that a galaxy's velocity dispersion correlates with its star formation history better than its dynamical mass ($\propto \sigma^2 R_e$) does.

The strong dependence of age and metallicity on velocity dispersion is consistent with previous studies (Smith et al., 2007; Nelan et al., 2005). Similar results were obtained in a recent analysis of the Six-degree Field Galaxy Survey (6dFGS) (Jones et al., 2004, 2009) by Springob et al. (2012), though this work finds a slightly stronger dependence on effective radius. G09 posited that the lack of dependence on R_e occurs because effective radius is strongly dependent on the orbital parameters of the major merger and subsequent dissipationless merg-

ers. This dependence introduces a large amount of scatter in the remnants' radii, effectively diluting any corresponding radial relations that were present in the progenitors.

Semi-analytic models (SAMs) provide a framework to simulate the formation and evolution of galaxies in a cosmological context (Kauffmann & White, 1993; Cole et al., 1994; Somerville & Primack, 1999; Cole et al., 2000; Hatton et al., 2003; Croton et al., 2006; De Lucia et al., 2006; Bower et al., 2006; Somerville et al., 2008b; Fontanot et al., 2009; Benson & Bower, 2010; Cook et al., 2010; Guo et al., 2011; Somerville et al., 2012). However, attempts to use SAMs to study the fundamental plane have been limited by the difficulty in modeling the effective radii and velocity dispersions of ellipticals. Cole et al. (2000) provide a simple formula to predict the radii of elliptical galaxies following a major merger using the virial theorem and conservation of energy assuming that the merging galaxies have a similar structure to the resulting spheroidal galaxy. While this relation may be correct for dissipationless gas-poor mergers, the energy lost due to star formation in gas-rich mergers results in a deviation from the virial relation, and smaller remnant radii (C08,C11) Incorporating this dissipation is probably essential: a recent study using the Bower et al. (2006) SAM framework could match the observed SDSS size-mass relation only by adding dissipation (Shankar et al., 2011). A second recent SAM paper that did not include dissipation in

modeling merger remnants had a too shallow slope and too much dispersion (Guo et al., 2011). The predicted scatter in the size-mass relations in these papers was also much larger than observed. Full N-body/SPH simulations of gas-rich mergers have been more successful (Dekel & Cox, 2006; Robertson et al., 2006b; Hopkins & Beacom, 2008), but they do not simulate enough galaxies to compare with observations of populations of galaxies as in G09.

The predictions of effective radius and velocity dispersion from Chapter 2 allow us to determine a simulated galaxy's location above, within, or below the FP, as measured by its residual surface brightness. In this Chapter we use the GF SAM to relate the age and metallicity of simulated galaxies across and through the FP with effective radius and velocity dispersion. We compare galaxies with properties given by the SAM to to the analysis of G09, and find that the stellar population metallically is correlated with both radius and velocity dispersion, while age is strongly dependent on velocity dispersion and almost independent of radius. The metallicity correlation is in contrast to observational results (G09), which found a tight correlation with velocity dispersion only and almost no correlation with radius for either age or metallicity.

We find that the age-velocity dispersion correlation stems from the correspondence between the velocity dispersion of the galaxy and the time at which it first became bulge-dominated; in contrast the metallicity correlation is a result

of the strong mass-metallicity correlation in the SAM. Examining the thickness of the fundamental plane, we find that galaxies that fall below the FP, with relatively lower surface brightnesses, tend to be both older, more metal-poor, and have shorter star formation timescales than galaxies that lie above the FP. This is in agreement with observations (Forbes et al., 1998; Terlevich & Forbes, 2002; Graves et al., 2009b). This chapter represents an improvement from previous work (Porter et al., 2012), in which we applied a simple model to predict the sizes of bulges resulting from major mergers in post-processing, but did not consider the effects of minor mergers or disk instabilities.

Section 5.3 presents a summary of the low-redshift observations of G09, to which we make direct comparisons. We present results beginning in Section 5.4, in which we examine the relationships between age and metallicity, on the one hand, and velocity dispersion and radius, on the other, throughout the fundamental plane for the GF SAM. We find that the age-fundamental plane relation is strongly dependent on velocity dispersion and weakly dependent on effective radius, in agreement with observations. At variance with observations, the metallicity-fundamental plane relation is dependent on effective radius as well as velocity dispersion, owing to the unrealistically-strong relationship between stellar mass and metallicity in the SAM. Section 5.5 examines the stellar population trends across a face-on projection of the FP and through the residual thickness

of the FP. In agreement with observations, we find that the thickness of the FP stems from structural differences in the central stellar surface densities of galaxies, rather than from differences in the stellar mass-to-light ratios.

5.2 Methods

5.2.1 Selection Criteria

Drawing from 23 (50 h^{-1}Mpc)^3 subvolumes of the Bolshoi merger tree, we allow stellar bulges to form via mergers and disk instabilities. All results use the 'Stars and Gas DI' version of GF, in which both stars and gas can contribute to disk instabilities. Since we want to study quiescent early-type galaxies at low redshifts, we include in this analysis only bulge-dominated galaxies with specific star formation rates less than 0.1 $M_\odot$ yr^{-1}/$10^{11}M_\odot$. To compare directly to G09, we also exclude galaxies with r-band absolute magnitudes $M_r > -19.0$, which fall far below the G09 50% completeness threshold of $M_r = -19.7$. Making these selection cuts, we include 4342 bulge-dominated galaxies from the SAM. We draw the mass-weighted ages, metallicities, and K-band luminosities of the galaxies directly from the SAM, which uses the stellar population synthesis model of Bruzual & Charlot (2003) following a Chabrier (2003) IMF.

5.2.2 Binning in the fundamental plane

Once the age, metallicity, effective radius, luminosity, and velocity dispersion have been calculated for all galaxies, we select bulge-dominated galaxies at redshift zero using the selection criteria described above. We separate this population into three regimes according to their location perpendicularly above or below (i.e. 'through') the fundamental plane, using surface brightness as the independent variable. Since we intend to compare to the G09 results, only galaxies that fall within the G09 range of radius, ($0.0 < \log(R_{\rm e}/{\rm kpc}) < 0.7$) and velocity dispersion, ($2.0 < \log(\sigma/{\rm km\ s^{-1}}) < 2.4$) at redshift zero, are included in the fitting routine. We use a least-squares fit to determine a relation between (log) $R_{\rm e}$, (log) σ, and (log) $I_{\rm e}$, finding the fundamental plane prediction

$$\log \frac{I_{\rm e}}{{\rm L_\odot\ pc^{-2}}} = -1.59\ \log \frac{R_{\rm e}}{\rm kpc} + 1.65\ \log\ \frac{\sigma}{\rm km\ s^{-1}} - 0.49. \tag{5.1}$$

For each remnant, the predicted surface brightness is determined using the above relation, and galaxies are separated by their residuals $\Delta \log(I_e/{\rm L_\odot\ pc^{-2}})$ Residuals in the range [-0.3,-0.1], [-0.1,0.1], and [0.1,0.3] are termed the low-, mid-, and high-FP, respectively. Galaxies 'above' the FP have higher surface brightnesses than one would predict using their effective radii and velocity dispersions, while galaxies 'below' the FP have lower surface brightnesses. Galaxies with residuals outside the range [-0.3,0.3] are excluded. If we plot the simulated galaxies according to their location in FP-space, 90.2% of the galaxies fall within the low-to-high FP

slices (Figure 5.1).

After separating the remnants by their location within the FP, we place them in bins according to their radius and velocity dispersion just as G09 did for SDSS galaxies. We define this face-on projection in R_e and σ to be 'across' the FP. We then calculate the median age and metallicity for all galaxies within each bin, excluding bins with fewer than five galaxies for statistical purposes. These values are used to form contours relating the stellar population parameters, namely age and metallicity, with the fundamental plane parameters and residuals. We caution that the simulated quantities are mass-weighted, while G09 calculates light-weighted ages, metallicities, and effective radii.

Comparing the GF and G09 populations, we find that they occupy slightly different regions of the R_e-σ parameter space (Figure 5.2). The SAM includes a population of galaxies with low radii and low surface brightnesses that is not seen in G09. These galaxies tend to have low stellar masses and absolute magnitudes, and thus fall below the G09 completeness threshold.

5.3 Summary of Observations

We compare our findings to a recent survey of early-type galaxies from the Sloan Digital Sky Survey (SDSS) (York et al., 2000) Spectroscopic Main Galaxy Survey (Strauss et al., 2002) Data Release 6 (Adelman-McCarthy et al., 2008).

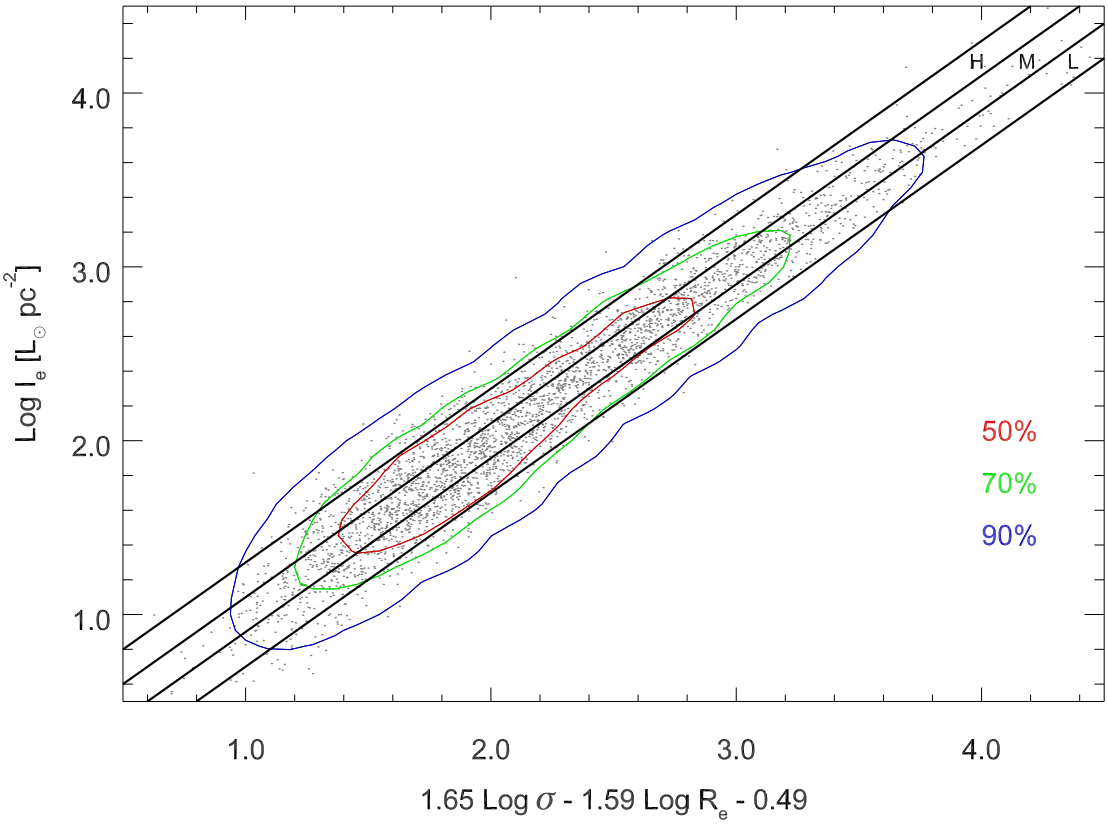

Figure 5.1: Distribution of simulated galaxies through the fundamental plane. Galaxies are fit to a linear relation (horizontal axis) relating surface brightness with velocity dispersion and radius. The measured surface brightnesses are then plotted against the expected values. The areas between the solid black lines represent the slices we term the 'low-FP' (L), 'midplane' (M), and 'high-FP' (H), from bottom to top, according to the residual in surface brightness. Each slice has a thickness of 0.2. 90.2% of the galaxies fall within the middle three FP slices. The red, green, and blue contours enclose 50%, 70%, and 90% of all galaxies, while the grey points represent individual galaxies.

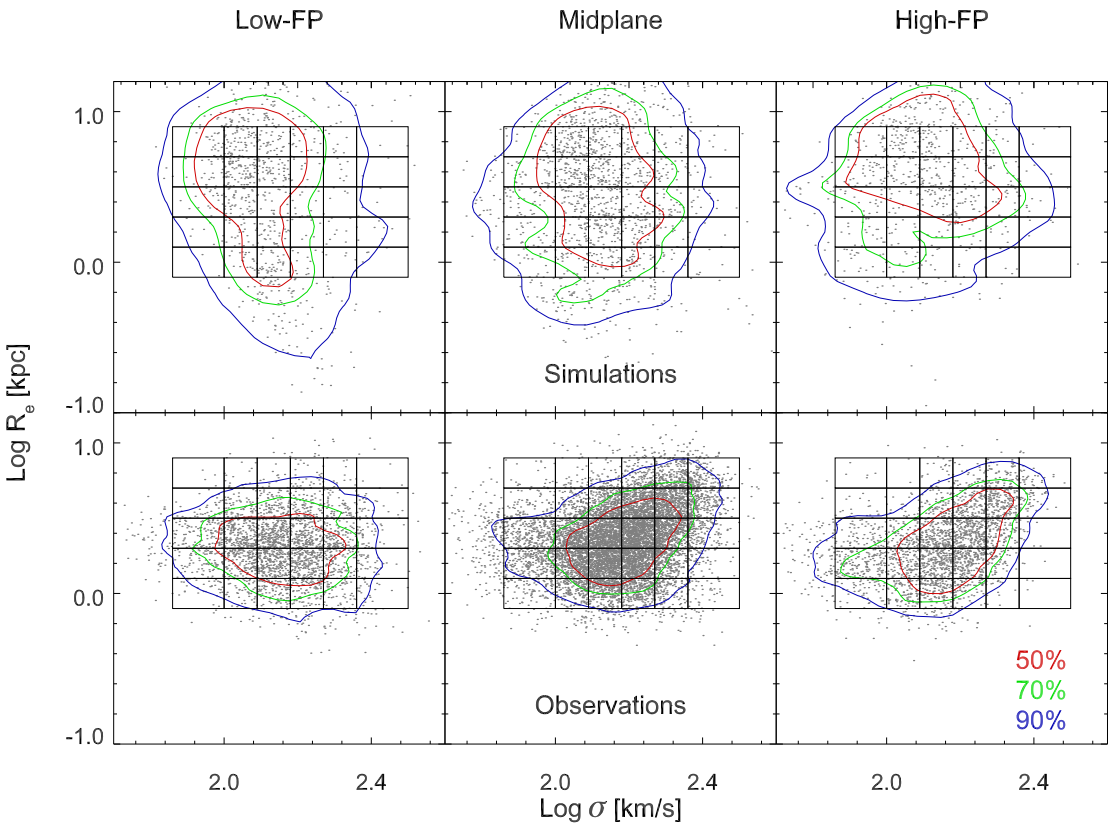

Figure 5.2: Distribution of radius and velocity dispersion for galaxies within each slice of the FP for GF (top) and G09 (bottom). From left to right, the panels represent the 'low-FP', 'midplane', and 'high-FP' slices. The grid lines show the bin definitions in the region observed in G09; the median age and metallicities are calculated within each bin. The SAM contains a population of galaxies with low radii and low surface brightnesses that fall below the completeness threshold of the G09 survey. The red, green, and blue contours enclose 50%, 70%, and 90% of galaxies meeting our selection criteria, while the grey points represent individual galaxies.

The sample of galaxies is described in Graves et al. (2009a,b). The galaxies selected were observed in the redshift range $0.04 < z < 0.08$, with light profiles that were both centrally concentrated and fit a de Vaucouleurs profile. To prevent a small proportion of young stars from biasing the measured luminosity, G09 excluded actively star-forming galaxies. Using colors and emission-line intensities, G09 also rejected Seyfert hosts, low ionization nuclear emission-line region (LINER) hosts, and transition objects, as they can host active galactic nuclei (AGN) which have been found to have light profiles intermediate between early- and late-types (Kauffmann et al., 2003). We have excluded actively star-forming galaxies from the sample, as noted above; but no attempt has been made to exclude galaxies that the SAMs characterize as having active AGN at redshift zero. While the results presented here are for galaxies at redshift zero we have also checked that including galaxies from the range $< z < 0.08$ does not significantly change the results.

We also note that the population of simulated galaxies consists solely of bulge-dominated galaxies that have formed bulges via mergers or disk instabilities; this may not exactly correspond to the population of observed early-type galaxies. Both the simulated and G09 populations may contain a significant number of passive S0 and Sa galaxies. While the GF SAM does reproduce the early-type mass function of Baldry et al. (2012), an analysis of quiescent red sequence SDSS

galaxies similar to the population studied in G09 found that separating galaxies by their stellar bulge-to-total ratios, as we have done, produced a high fraction of S0 and Sa galaxies. More precisely, 36% of the galaxies were true elliptical galaxies while 15% were S0 galaxies and 48% were Sa galaxies (Cheng et al., 2011). Thus, a detailed examination of the fundamental plane will require limiting the simulated and G09 samples to pure elliptical galaxies.

Using the Lick indices (Worthey et al., 1994; Worthey & Ottaviani, 1997) on 16,000 stacked spectra, G09 calculated mean light-weighted ages and metallicities in bins with residual surface brightness above, within, and below the fundamental plane. The bins covered the approximate range ($0.0 < \log(R_{\rm e}/{\rm kpc}) < 0.7$), ($1.9 < \log(\sigma/{\rm km\ s^{-1}}) < 2.4$), and $-0.3 < \Delta \log(I_e/{\rm L_\odot\ pc^{-2}}) < 0.3$, where $\Delta \log I_{\rm e}$ is the residual surface brightness resulting from a log fit in radius and velocity dispersion,

$$\log \frac{I_{\rm e}}{{\rm L_\odot\ pc^{-2}}} = -1.21\ \log \frac{R_{\rm e}}{\rm kpc} + 1.16\ \log\ \frac{\sigma}{\rm km\ s^{-1}} + 0.45 \tag{5.2}$$

G09 formed contours relating the mean light-weighted age and light-weighted metallicities, [Fe/H], [Mg/H], and [Mg/Fe], to effective radius and velocity dispersion across three slices of the fundamental plane. While the GF SAM does include a prescription to track contributions from different elements (Arrigoni et al., 2010b,a), in this work we are only using the total metallicity Z and are not modeling Type I supernova. We thus consider the SAM metallicity to be most

similar to [Mg/H], a measure of alpha-enhancement.

The relevant results can be seen in Figures 7 and 9 of G09. The authors found that stellar population age and metallicity are nearly independent of effective radius but strongly correlated with velocity dispersion. An analysis of the 6dFGS, which has a wider fiber aperture than SDSS, found similar correlations (Magoulas et al., 2012; Springob et al., 2012). In all three slices of the FP, galaxies with larger σ had older ages and higher metallicities. Stellar population age was also inversely correlated with residual surface brightness, so that the youngest galaxies tend to fall above the FP, in agreement with earlier observations (Forbes et al., 1998; Terlevich & Forbes, 2002). A key conclusion of a subsequent analysis (Graves & Faber, 2010; Graves et al., 2010) was that these trends arise because of structural differences in galaxies; galaxies below the FP have earlier truncation times and formed most of their stars early, while galaxies above the FP have more extended star formation histories.

5.4 Results

Our major findings are the contours seen in Figure 5.3. Stellar population age increases with velocity dispersion and is only weakly dependent on radius. We note that the parameter space has a much larger range in radius than velocity dispersion, so that while the contours appear nearly vertical, the radial depen-

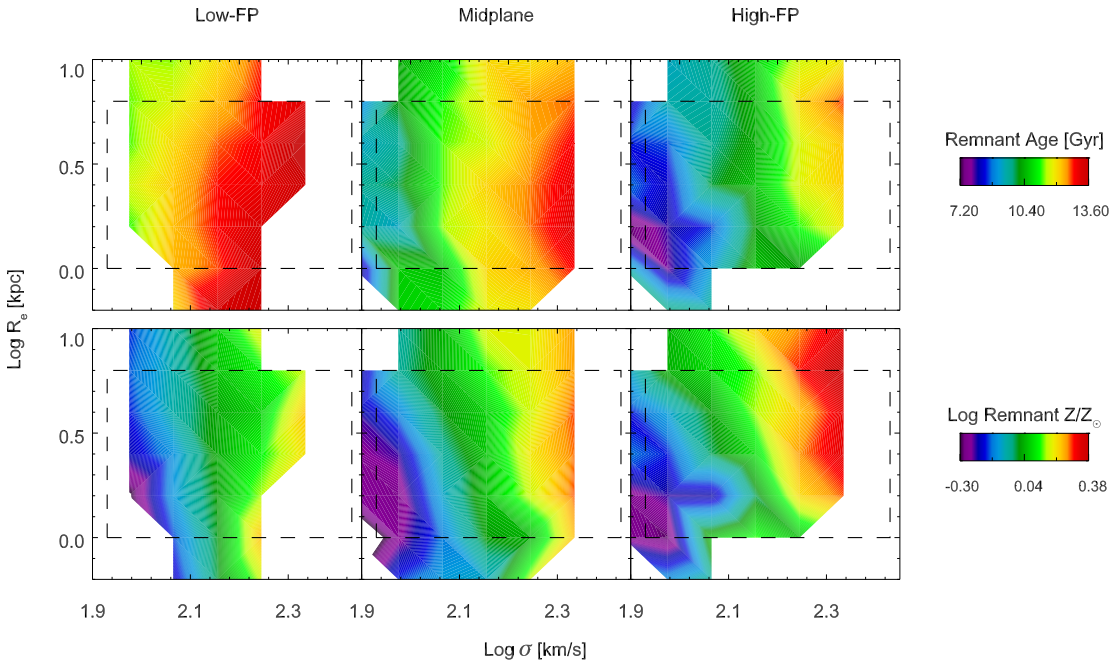

Figure 5.3: Relation between mass-weighted age (top) and metallicity (bottom), effective radius, and velocity dispersion for elliptical galaxies in GF. The different panels represent the three central slices of the FP, as shown in Figure 5.2. The grey dashed line indicates the region analyzed in G09. Stellar population age increases strongly with velocity dispersion and has no clear trend with radius. These results are in qualitative agreement with observations. Metallicity increases with both radius and velocity dispersion (contours are tilted); this is in contrast to observations, in which metallicity increases solely with velocity dispersion. At fixed radius and velocity dispersion, galaxies that lie above the FP tend to be younger and more metal-rich than those that lie below the FP.

dence is non-negligible. If we consider the middle slice of the FP, the correlation between stellar age and effective radius has a Spearman rank coefficient ρ = -0.04 indicating nearly no correlation. The relationship between age and velocity dispersion is much stronger, with a Spearman rank coefficient $\rho = 0.54$. Looking through the FP, galaxies that lie above the FP (those with the largest residuals in log I_e) have younger ages, as suggested from previous observations (Forbes et al., 1998; Terlevich & Forbes, 2002, G09). Galaxies above the FP have a mean age of 10.02 ± 1.61 Gyr, as compared to 12.12 ± 1.12 Gyr for galaxies below the FP.

If we compare the metallicity contours, the differences between the SAM and observations are more pronounced. In the simulated galaxies, metallicity increases strongly with velocity dispersion ($\rho = 0.77$) and weakly with effective radius ($\rho = 0.11$), whereas the G09 galaxies have very little dependence on effective radius. This dependence on effective radius is strongest for galaxies above the FP. As in G09, galaxies that lie above the FP do tend to have higher metallicities ($[Z] = 0.11 \pm 0.52$ vs. $[Z] = 0.01 \pm 0.17$ for high-FP and low-FP galaxies, respectively).

5.4.1 Analysis of the age and metallicity trends

The discrepancy between the simulated and observed metallicity-FP trends is striking but not unexpected: the simulated galaxies have mass-weighted metallicities, while the observe quantities are light-weighted, preventing a direct com-

parison between the two quantities. The GF SAM has a smaller degree of scatter than the observed (Gallazzi et al., 2005) mass-metallicity relationship (Somerville et al., 2008b) for high-mass galaxies (but see Woo et al. (2008a); Kirby et al. (2010), who find a tighter relationship in low-mass dwarf galaxies).

If we consider that stellar mass is closely related to the dynamical mass, which is in turn proportional to $\sigma^2 r$ then the implications of Figure 5.3 become clearer: the tight mass-metallicity relationship is reflected in a dependence of metallicity on both effective radius and velocity dispersion in the projected fundamental plane. In fact, when stellar mass and metallicity are plotted alongside each other in the middle slice of the fundamental plane, we find that the trends are nearly identical (Figure 5.4). As we will show, galaxies above the fundamental plane have the lowest concentrations of dark matter within their effective radii, making the dependence on stellar mass even more pronounced.

We next discuss the simulated age-FP trend, which shows a remarkable agreement with observations. We note that, in the model, the velocity dispersion is calculated from both the effective radius and the total mass within that radius; thus velocity dispersion and effective radius are intrinsically linked. However, the ages of the simulated galaxies have a clear dependence on the former and almost no dependence on the latter. As we will discuss, minor mergers are mainly responsible for removing any correlation between age and effective radius while

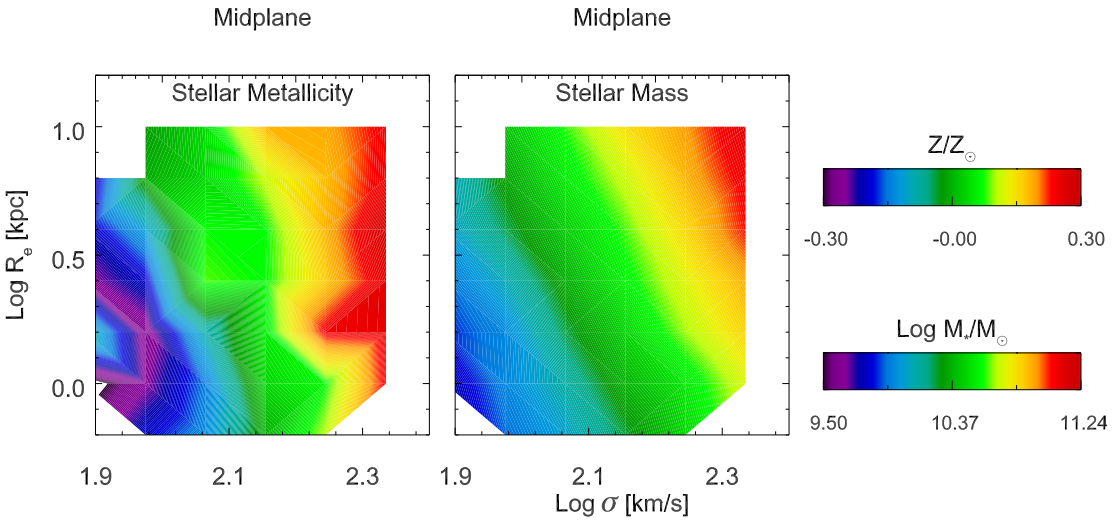

Figure 5.4: Relation between mass-weighted metallicity (left) and stellar mass (right), effective radius, and velocity dispersion for elliptical galaxies in GF. Both panels represent the middle slice of the FP, as shown in Figure 5.2. Colors are individually normalized. Since the SAM has an unrealistically strong correlation between stellar mass and metallicity, the two trends are nearly identical.

preserving the relation between age and velocity dispersion.

5.4.2 Comparison to observations

To better compare with G09, we have replotted the age and metallicity contours over the range $(0.0 < \log(R_e/\mathrm{kpc}) < 0.7\ )$, $(1.9\ < \log(\sigma/\mathrm{km\ s^{-1}}) < 2.4)$, and $-0.3 < \Delta \log(I_e/\mathrm{L_\odot\ pc^{-2}}) < 0.3$ considered by Graves et al. (2009b) alongside the G09 data (Figures 5.5 and 5.6). We caution that the G09 ages were later found to be systematically high by ~ 0.12 dex, owing to weak emission in the Hβ absorption line (Graves & Faber, 2010); however, this would not affect the overall trends. We also note that we calculate mass-weighted ages and metallicities while G09

calculated light-weighted ages and metallicites using the Lick indices. These light-weighted quantities have been shown to more closely correlate with the period of most recent star formation, instead of a global quantity (Trager & Somerville, 2009).

Examining the trends within FP slices, the age-FP correlations are in rough agreement with G09. The major difference between our results and those of G09 is that we find metallicity to be dependent on radius and velocity dispersion especially above the FP, while G09 found metallicity to be dependent on velocity dispersion alone. The SAM does a better job of reproducing observed trends through, as opposed to across, the FP. Galaxies that fall above the FP tend to be younger and more metal-enhanced than average, while those that fall below the FP are older and more metal-poor, in agreement with G09.

5.5 Discussion

Having established the major trends of age and metallicity through the fundamental plane, we can now attempt to characterize the significance of these trends. A key question is how much of the variation through the fundamental plane arises from structural differences in galaxies as compared to the passive fading of elliptical galaxies. If galaxies do 'settle' onto the FP over time, we might expect galaxies above the FP to have younger ages and higher metallicities, in agreement with

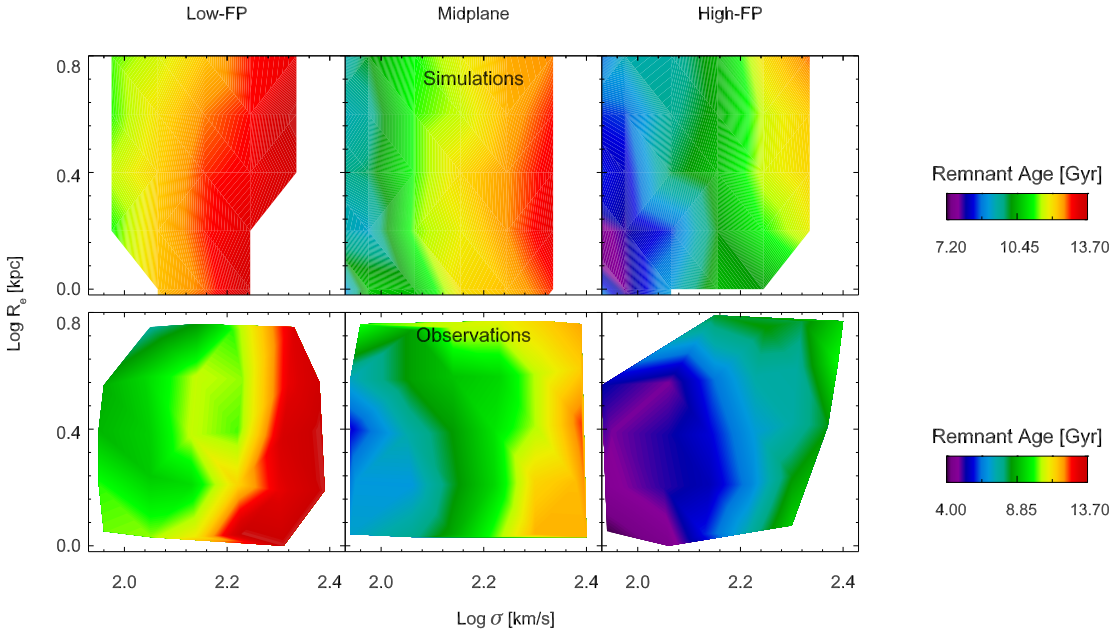

Figure 5.5: Relation between mass-weighted age, effective radius, and velocity dispersion for early-type galaxies in GF (top) and G09 (bottom). Here we plot only the region considered in G09. The different panels represent the three central slices of the FP, as shown in Figure 5.2. In the SAM and the observations, stellar population age increases with velocity dispersion, but the SAM galaxies display a narrower range in age. Galaxies that lie above the FP also tend to be younger than those that lie below the FP.

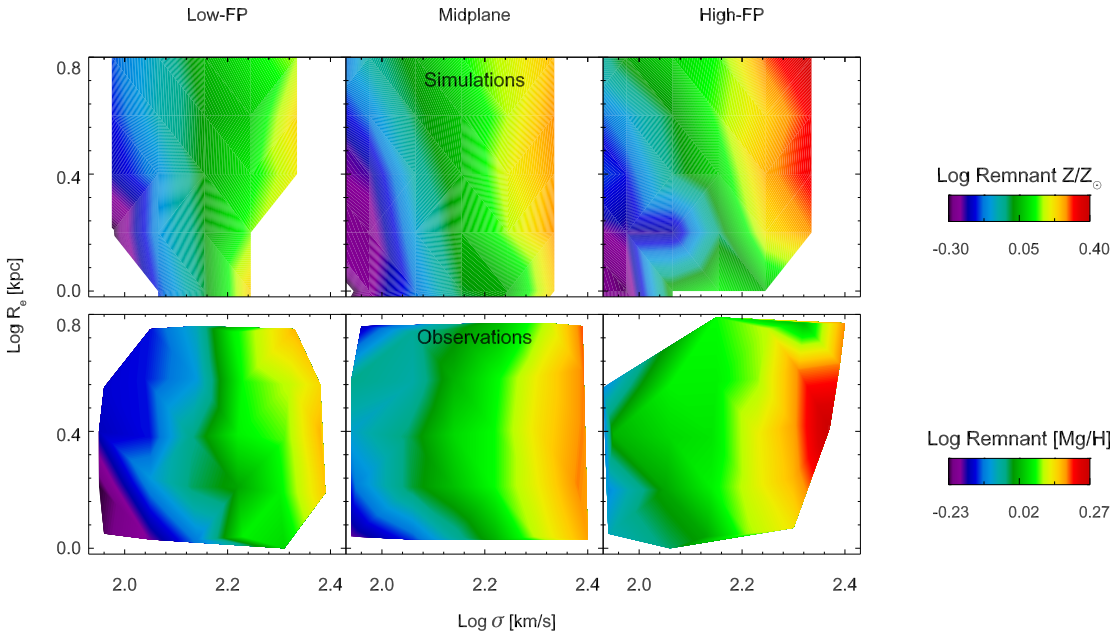

Figure 5.6: Relation between mass-weighted metallicity, effective radius, and velocity dispersion for elliptical galaxies in GF (top) and G09 (bottom). Here we plot only the region considered in G09. The different panels represent the three central slices of the FP, as shown in Figure 5.2. While [Mg/H] depends strongly on velocity dispersion in G09, in the SAM metallicity depends on both velocity dispersion and effective radius. The simulated galaxies tend to have slightly lower metallicities than observations on average.

both simulations and observations. However, this process would not explain why age and metallicity appear to be more strongly correlated with velocity dispersion than effective radius. In addition, this would not explain the significant overlap in age and metallicity ranges in the three FP slices.

5.5.1 Analysis of trends across the FP

In order to understand all of these trends simultaneously, it is necessary to study the implications of our prescription for effective radius and velocity dispersion. In our model, a galaxy's effective radius and velocity dispersion are tightly correlated, regardless of whether it forms a bulge through a merger or through a disk instability event. As a population however, galaxies experience large changes in effective radius with redshift, but only moderate changes in velocity dispersion. By quantifying the scatter introduced by these evolutionary processes we can attempt to explain how low-redshift galaxies with similar ages and metallicities have similar velocity dispersions but a range of effective radii.

Recent works (Naab et al., 2009; Hopkins et al., 2010; Oser et al., 2012) have suggested that gas-poor minor mergers may produce at least some of the observed evolution in the size-mass relation for early-type galaxies, forming an evolutionary link between the compact galaxies seen at high redshifts and the more diffuse galaxies seen in the local universe. While there is some question as to whether the

merger rate is sufficient to explain all of the size evolution (Trujillo et al., 2011; Newman et al., 2012; Nipoti et al., 2012; Quilis & Trujillo, 2012), we can predict the effect that these events would have on the population.

It is important to note that in our simulation-based model any merger where one or both of the progenitors is bulge-dominated is treated as a dissipationless event, as we explained in Chapter 2. Thus, mergers between a massive compact elliptical and a smaller galaxy can be expected to significantly increase the size of the remnant galaxy. Using conservation of energy and the virial theorem, Naab et al. (2009) show that for a series of minor mergers that increase the mass of the galaxy from $M_{\rm i}$ to $M_{\rm f}$, the radius increases as $(M_{\rm f}/M_{\rm i})^2$ while the velocity dispersion decreases as $(M_{\rm f}/M_{\rm i})^{-1/2}$. These scaling relations necessarily introduce a large amount of scatter in effective radius: if, for example, two identical galaxies increase their masses by a factor of 1.9 and 2.0 respectively, their resulting radii will differ by 9.8% while their velocity dispersions will only differ by 2.6%.

This large amount of variation in effective radius means that any original correlations between effective radius and age or metallicity will be weakened over a series of minor mergers. It is interesting to note that this model predicts that there may be a stronger dependence on effective radius at higher redshifts, where the effects of minor mergers are less prevalent.

A second major implication of these scaling relations is that the velocity dis-

persion of a galaxy should remain relatively unchanged from its formation to the present day; if anything, it should decrease slightly. This prediction is in agreement with both simulations (Oser et al., 2012) and observational evidence that the velocity dispersion function evolves to higher values at higher redshifts but at a rate much slower than the evolution in the size-mass relation (Cenarro & Trujillo, 2009; Bezanson et al., 2011).

Since the SAM, based on the Bolshoi simulation merger trees, contains the detailed merger history of every simulated galaxy, we are able to test this prediction directly. If we define the 'assembly time' as the time a galaxy most recently became bulge-dominated, we can examine its variation across and through the FP using the same method as described earlier for age and metallicity. The results can be seen in Figure 5.7. As expected, galaxies with higher velocity dispersions tend to have assembled earlier. Thus, a galaxy's velocity dispersion may be a key signature relating its current structure to the epoch of its formation.

Figure 5.7 also shows that galaxies below the FP tend to have earlier assembly times. There is a significant amount of overlap in this correlation however; in particular the galaxies with the highest velocity dispersions have similar high formation times for all three slices of the FP. This indicates that a further process must be invoked to explain the trends through the thickness of the FP.

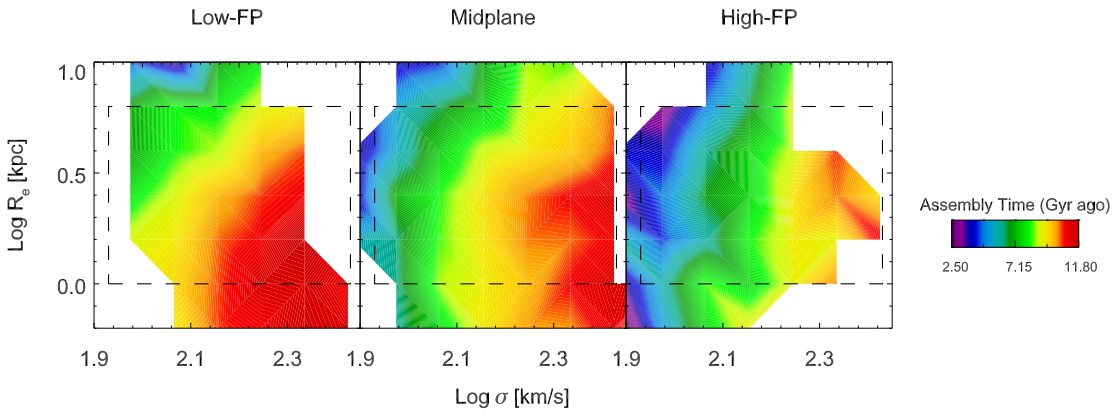

Figure 5.7: Relation between the time since the galaxy was assembled, effective radius, and velocity dispersion for elliptical galaxies. The different panels represent the three central slices of the FP, as shown in Figure 5.2. Galaxies that assembled earlier have higher velocity dispersions and tend to fall below the FP.

5.5.2 Analysis of trends through the FP

Stellar population trends through the thickness the FP can arise in a number of different ways; any process that increases the dynamical mass-to-light ratio of a galaxy will move it further below the virial plane. Graves & Faber (2010) provide a decomposition of the deviation from the virial theorem, separating it into four components:

1. The ratio of the estimated dynamical mass to the true mass within one R_e.

2. The ratio of the true mass within one R_e to the projected stellar mass.

3. The ratio of the projected stellar mass with an assumed initial mass function (IMF) to the true stellar mass and its corresponding IMF.

4. The stellar mass-to-light ratio for the assumed IMF.

For the simulated galaxies and their corresponding FP, the first and third terms are identically one, as we have no uncertainty in the dynamical mass estimate and we model and 'observe' galaxies using the same IMF. Since we know the stellar mass-to-light ratio for the galaxies and can calculate the central dark matter fraction (DMF, see below), we may calculate the second and fourth terms directly. We note that if our assumed Chabrier IMF is incorrect, or if the IMF is non-universal (Conroy & van Dokkum, 2012; Dutton et al., 2012; Spiniello et al., 2012) the fourth term would change; we discuss the implications of a different IMF later in this section.

We have used the same process as described above to project the dynamical-to-stellar mass and stellar mass-to-light ratios of elliptical galaxies across and through the FP (Figure 5.8). The results are in agreement with the conclusions of Graves & Faber (2010): galaxies that fall below (above) the FP have higher (lower) dynamical-to-stellar mass ratios and slightly higher (lower) stellar mass-to-light ratios. Stated another way, galaxies below the FP have lower stellar masses and central surface densities at fixed R_e. The variations in stellar mass-to-light ratio are due to differences in the stellar populations: since galaxies above the FP are younger than galaxies below the FP, they have more young stars and hence higher stellar mass-to-light ratios. The variations in the central dark matter fraction reflect structural differences in the density profiles of galaxies and dark

matter halos.

Comparing the trends through the thickness of the FP, at fixed R_e and σ the dynamical-to-stellar mass ratio has a much larger degree of variation than the stellar mass-to-light ratio. If we limit our analysis to bins of R_e and σ that have at least 5 galaxies in each slice of the FP, we find that the average variance in the dark matter fraction contributes 94% of the thickness of the FP, while the stellar mass-to-light ratio only contributes 6%. This is in general agreement with Graves & Faber (2010), who found that the dark matter fraction and IMF variation have a combined contribution in the range of 47% - 98%, and that measured variations in the stellar mass-to-light ratio were insufficient to explain all of the thickness of the FP. This is another indication that underlying structural differences, as opposed to passive fading, are the main contributors to the thickness of the FP.

We note that our model assumes that all stars formed under a Chabrier IMF. There is mounting evidence, however, that the IMF may be non-universal. Early-type galaxies and bulges with high stellar masses or velocity dispersions in the local universe may follow a 'bottom-heavy' IMF, with more low-mass stars (Conroy & van Dokkum, 2012; Dutton et al., 2012; Spiniello et al., 2012). While there is some disagreement as to the slope of this bottom-heavy IMF, an IMF that varies with velocity dispersion would contribute to the thickness of the simulated FP; galaxies below the FP with high velocity dispersions would have higher stellar mass-to-

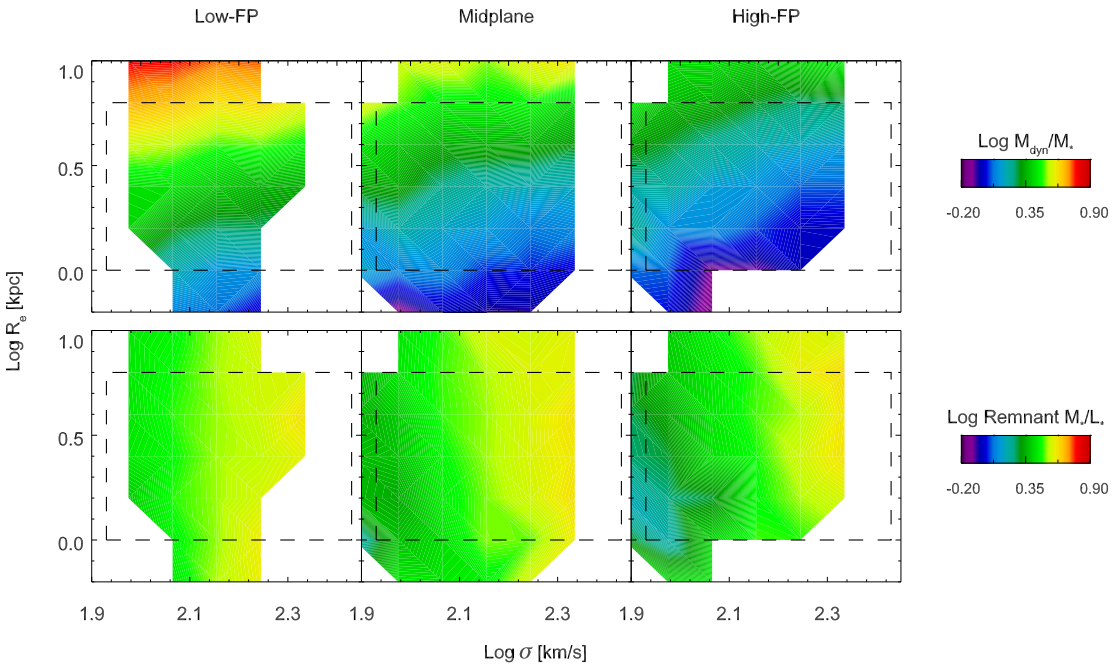

Figure 5.8: Relation between dynamical-to-stellar mass ratio (top), stellar mass-to-light ratio (bottom), effective radius, and velocity dispersion for elliptical galaxies. The different panels represent the three central slices of the FP, as shown in Figure 5.2. The grey dashed line indicates the region analyzed in G09. Galaxies that fall below the FP have higher dynamical-to-stellar masses and mass-to-light ratios. The variation in dynamical-to-stellar mass through the FP is much larger than the variation in the mass-to-light ratio (note that both relations use the same color scalings).

light ratios, moving them even further below the FP. Thus while our results are consistent with those of Graves & Faber (2010), we have not accounted for any contributions from a varying IMF in this work.

To summarize our results so far, we have found that galaxies below the FP tend to be old and metal-poor. They became bulge-dominated at early times, and have high dynamical-to-stellar mass ratios at a given R_e and σ. In contrast galaxies above the FP tend to be young and metal rich, with late formation

times and relatively high stellar masses at fixed R_e and σ. In an analysis of the trends found in G09 and Graves & Faber (2010), Graves et al. (2010) found these results could be explained by a scenario in which galaxies below the FP have their star formation truncated at early times, while those above the FP have more extended star formation histories. Since the SAM contains information about the star formation histories for every galaxy, we can see whether our galaxies are described by this scenario.

The GF SAM keeps track of the stellar masses of galaxies at redshift zero, separated into 196 log-spaced bins in age. For this analysis, we have defined the 'star formation duration' as the duration over which each galaxy formed the middle 68% of its stars. Thus galaxies with a wider distribution of stellar ages will have longer star formation durations. We have defined 'formation time' as the time by which half of the stars in the galaxy have formed; this quantity is significant because it incorporates information about the stars that formed in situ in the galaxy as well as those that were accreted. Taken together, the 'assembly time' (Figure 5.7) and the 'formation time' provide a link between the structure of a galaxy and the properties of its stellar population. These definitions are summarized in Table 5.1.

We have plotted the correlations between star formation duration and formation time, effective radius, and velocity dispersion for all three FP slices in Figure

Table 5.1: Parameters used to determine the mass assembly histories of early-type galaxies. The low-FP, mid plane, and high-FP values are the mean of each parameter for early-type galaxies in each plane.

Parameter	Description	Low-FP	Midplane	High-FP
Assembly time (Gyr ago)	Time when the galaxy most recently became bulge-dominated	9.1 ± 2.2	8.3 ± 2.6	6.6 ± 3.3
Formation time (Gyr ago)	Time by which 1/2 of the stars in a galaxy formed	10.8 ± 0.7	10.3 ± 0.9	9.2 ± 1.3
Star formation duration (Gyr)	Time to form the middle 68% of a galaxy's stars	2.3 ± 0.9	2.8 ± 1.0	3.9 ± 1.2

5.9. Comparing the relations, it is evident that galaxies below the FP have early formation times and short star formation timescales; in fact roughly 75% of these galaxies have star formation timescales less than 2 Gyr. Galaxies above the FP formed their stars slightly later, but more significantly, they have much longer star formation timescales. 70% of these galaxies have star formation durations *greater* than 2 Gyr.

The long duration of star formation allows for a higher conversion of gas to stars, increasing the dynamical-to-stellar mass ratio. As we established earlier that variations in the mass-to-light ratio cannot account for most of the thickness of the FP, these galaxies will not 'fall' onto the FP over time. Their assembly histories have produced galaxies with high baryon fractions and high stellar central surface densities, and their relatively recent star formation has produced stellar

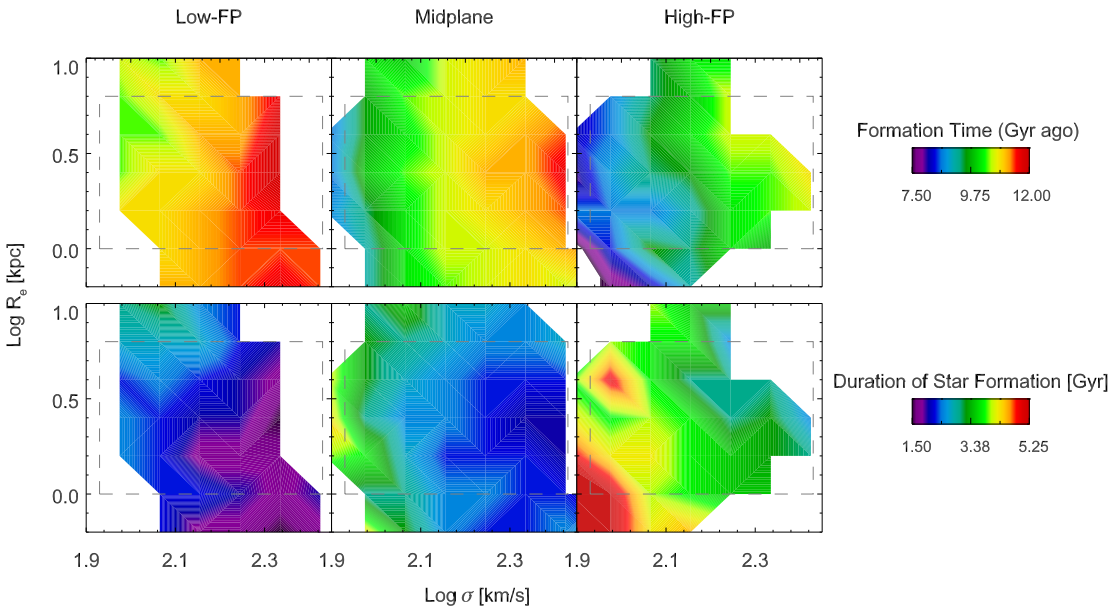

Figure 5.9: Relation between the formation time (top), duration of star formation (bottom), effective radius, and velocity dispersion for elliptical galaxies. The different panels represent the three central slices of the FP, as shown in Figure 5.2. The grey dashed line indicates the region analyzed in G09. Galaxies below the FP tend to have formed their stars early and have short star formation timescales. Galaxies above the FP have extended star formation histories and formed their stars more recently.

populations with young ages and high metallicities. This result is the key prediction of our model: the thickness of the FP appears to be due to structural differences in the galaxies resulting from their differing formation histories. Previous works (Wechsler et al., 2002) have linked the z=0 concentrations and shapes of dark matter halos with the duration and epoch of mass assembly; here we perform a similar analysis for early-type galaxies.

At last, we can combine these relations to account for both the structural and the stellar population differences through the FP. Galaxies below the FP be-

came bulge-dominated early, in a regime in which both halo concentrations and stellar velocity dispersions were higher. This may also account for the compact tail of galaxies seen in the low-FP pane Figure 5.2. These galaxies formed their stars and quenched early, leaving them with old ages, low metallicities, and structural properties that are perhaps representative of compact ellipticals at higher redshifts.

In contrast, galaxies above the FP became bulge-dominated and formed their stars slightly later. More importantly, they have extended star formation histories, producing galaxies with younger ages and higher metallicities. While they do have slightly lower stellar mass-to-light ratios, most of the variation in residual surface brightness stems from their high central stellar surface densities and low dark matter fractions.

5.6 Conclusions

We have used the GF (Somerville et al., 2008b, 2012, Porter et al. 2013a) SAM along with an analytic model for the size and velocity dispersion of stellar bulges from Covington et al. (2008, 2011) and Guo et al. (2011) to predict the distribution of early-type galaxies across and through the fundamental plane. We allow the model to run self-consistently to redshift zero, at which point we select quiescent bulge-dominated galaxies. We then separate them according to their residual

surface brightness in the fundamental plane and calculate the mass-weighted ages and metallicities as a function of effective radius and velocity dispersion.

In agreement with G09 and an analysis of the 6dFGRS (Magoulas et al., 2012; Springob et al., 2012), we find that stellar ages increase as a strong function of velocity dispersion and are nearly independent of radius. We predict that the strong correlation with velocity dispersion stems from the fact that the velocity dispersion of the galaxy changes little from its formation to the present day. Meanwhile minor mergers and ongoing DI introduce large amounts of variation in the size over time, diminishing any correlations with effective radius.

We show that galaxies with higher residual surface brightness tend to be younger and more metal-rich. Examining their structural properties, we find them to have lower stellar mass-to-light ratios and lower dynamical-to-stellar mass ratios. These galaxies became bulge-dominated relatively recently and formed their stars later than galaxies below the FP. Furthermore these galaxies have extended star formation histories, allowing for a higher conversion of baryonic matter to stellar mass and for the production of young, metal-rich stars.

We find that variations in the stellar mass-to-light ratio and the dark matter fraction within one effective radius both contribute to the thickness of the FP, with the dark matter fraction having a much larger effect. Galaxies above the FP have higher ratios of stellar-to-dark matter within one effective radius; put another

way, at fixed halo mass, galaxies above the FP have more efficient star formation. This result is also in agreement with the conclusions of G09, although we have not allowed for any contribution from a non-universal IMF. The reasonably good agreement of our SAM predictions with SDSS observations motivates to pursue more detailed modeling. We predict that the thickness of the FP is largely due to structural differences between galaxies, rather than stellar population differences.

A newer version of the GF SAM than was used here contains a detailed Galactic Chemical Evolution model, including non-instantaneous recycling, enrichment by both core collapse and Type Ia supernovae, and tracking of multiple chemical elements, as described in Arrigoni et al. (2010b,a). We also plan to calculate ages and metallicities using the Lick indices instead of using approximations to calculate the mass-weighted properties. This will allow us to make direct comparisons with [Fe/H], [Mg/H], and [Fe/Mg]. As an analysis of SDSS galaxies found that most red sequence galaxies are actually S0 or Sa galaxies rather than ellipticals, we also plan to separate the population considered in G09 into elliptical and S0/Sa galaxies, using an automated morphological classification scheme (Cheng et al., 2011).

Chapter 6

Conclusion

We construct a simple prescription based on hydrodynamical simulations (Cox, 2004; Cox et al., 2006; Johansson et al., 2009) to predict the effective radii and velocity dispersions of early-type galaxies. We apply this prescription to a semi-analytic model based on the Bolshoi ΛCDM simulations of halo merger trees, allowing for bulge formation via major and minor mergers as well as disk instabilities. We find that it is necessary to include disk instabilities in the model to reproduce the mass function of early-type galaxies, and that galaxies that form bulges via disk instability tend to form bulges earlier. This model is able to reproduce the low-redshift size-mass and Fundamental Plane relations. It predicts a degree of curvature in the Faber-Jackson relation that is not seen in local observations, but this could be offset if higher mass spheroids have more bottom-heavy

initial mass functions. The model is also able to match the observed rapid evolution of the size-mass relation out to higher redshifts, as well as the slower evolution in the normalization of the Faber-Jackson relation. We emphasize that these are genuine predictions of the model since it was tuned to match hydrodynamical simulations and not these observations.

We have also used the SAM to study the formation and evolution of massive galaxies. Separating galaxies based on their morphology and peak central surface density, we determine the effects of mergers, disk instabilities, and quiescent star formation on the sizes, surface densities, and star formation rates of massive galaxies. In agreement with observations, we find populations of compact red and blue galaxies at high redshift. We find that simulated compact star-forming galaxies are most likely to form from compact disks undergoing gravitational instabilities. These galaxies form much of their mass and quench at high redshifts. In contrast, gas-rich mergers produce less compact bulge-dominated galaxies. While minor and gas-poor mergers have the effect of increasing the sizes of all bulge-dominated galaxies, the galaxies with large amounts of disk instability activity remain the most compact even in the local Universe.

Using the SAM we predict the effective radius, velocity dispersion, luminosity, age, and metallicity of bulge-dominated galaxies, enabling us to compare directly to observations of the Fundamental Plane of local early-type galaxies. While we

find a tight correlation between age and metallicity and velocity dispersion, we find a stronger dependence of metallicity on effective radius than observations report. We find that the correlations with velocity dispersion arise as a result of the strong link between the assembly time of a galaxy and its velocity dispersion. Furthermore, minor mergers introduce a large amount of scatter in size, weakening any dependence on effective radius. The strong relationship between effective radius and metallicity stems from the tight mass-metallicity relationship in the SAM.

We examine the formation and assembly histories of the simulated galaxies and find that galaxies with relatively low surface brightnesses have early formation and assembly times, short star formation timescales, and high dynamical-to-stellar mass ratios. In contrast their stellar mass-to-light ratios are similar to those of galaxies with higher surface brightnesses. These correlations all suggest that the scatter in the fundamental plane results from structural differences in the galaxies themselves and not passive fading from a young, bright stellar population.

6.0.1 Future work

This thesis presents many avenues for future work. As we have shown, stellar bulges may have different sizes, masses, and formation timescales depending on how much of their growth was fueled by disk instabilities. We have demonstrated

that simple physical principles can be used to predict the sizes of bulges formed from mergers in hydrodynamical simulations. As of this writing however, there has not been a similar attempt to characterize the evolution in size, mass, and velocity dispersion from disk instabilities in hydrodynamical simulations. Such a treatment is necessary to fully understand the evolution of early-type galaxies in semi-analytical models.

The exquisite statistics of the Bolshoi simulation also present interesting opportunities to examine the importance of environment within a semi-analytical context. Several recent observations have suggested that cluster and field early-type galaxies may have different masses and assembly histories, and obey different scaling relations (Holden et al., 2010; Hoyle et al., 2011; Raichoor et al., 2011; Focardi & Malavasi, 2012; Kampczyk et al., 2013). These correlations should be apparent in the GF SAM if environment is taken into account. Similarly, there is an ongoing effort to characterize the age-FP and metallicity-FP correlations with local environment (Graves et al. in prep.). Extending the fundamental plane analysis in this work to account for variations with environment (as well as with redshift) would seem to be a natural progression.

All of the results presented here were for one set of parameters within the GF SAM. However there is a growing body of evidence that some of the prescriptions we have chosen, in particular the initial mass function and star formation prescrip-

tion, may be incomplete or incorrect (Conroy & van Dokkum, 2012; Krumholz & Dekel, 2011). Furthermore the current generation of SAMs uses a wide set of prescriptions for the same physical processes (e.g. merger interactions, gas cooling times, star formation rates, and black hole feedback). In ongoing work (Lu et al. in prep). we will present an analysis of the major similarities and differences between three SAMs (Croton et al., 2005; Lu et al., 2010; Somerville et al., 2012). These sort of cross-SAM comparisons should help to resolve which sets of measurements are robust predictions from the SAMs, and which areas are more uncertain.

Bibliography

Adelman-McCarthy J. K., Agüeros M. A., Allam S. S., Zehavi I., Zucker D. B., 2008, ApJS, 175, 297

Alexander D. M. et al., 2008, AJ, 135, 1968

Arrigoni M., Trager S. C., Somerville R. S., 2010a, ArXiv, 1006, 1147

Arrigoni M., Trager S. C., Somerville R. S., Gibson B. K., 2010b, MNRAS, 402, 173

Athanassoula E., 2008, MNRAS:L, 390, L69

Auger M. W., Treu T., Gavazzi R., Bolton A. S., Koopmans L. V. E., Marshall P. J., 2010, ApJ, 721, L163

Baldry I. K. et al., 2012, MNRAS, 421, 621

Baldry I. K., Glazebrook K., Brinkmann J., Ivezić Ž., Lupton R. H., Nichol R. C., Szalay A. S., 2004, ApJ, 600, 681

Barnes J. E., Hernquist L., 1996, AJ v.471, 471, 115

Barro G. et al., 2013, ApJ, 765, 104

Behroozi P. S., Wechsler R. H., Wu H.-Y., Busha M. T., Klypin A. A., Primack J. R., 2013, ApJ, 763, 18

Bell E. F., McIntosh D. H., Katz N., Weinberg M. D., 2003, ApJS, 149, 289

Benson A. J., Bower R., 2010, MNRAS, 405, 1573

Bezanson R. et al., 2011, ApJL, 737, L31

Bezanson R., van Dokkum P. G., Tal T., Marchesini D., Kriek M., Franx M., Coppi P., 2009, ApJ, 697, 1290

Birnboim Y., Dekel A., 2003, MNRAS, 345, 349

Bluck A. F. L., Conselice C. J., Buitrago F., Grützbauch R., Hoyos C., Mortlock A., Bauer A. E., 2012, ApJ, 747, 34

Blumenthal G. R., Faber S. M., Primack J. R., Rees M. J., 1984, Nat, 311, 517, 10.1038/311517a0

Bondi H., 1952, MNRAS, 112, 195

Bournaud F. et al., 2011, ApJ, 730, 4

Bower R. G., Benson A. J., Malbon R., Helly J. C., Frenk C. S., Baugh C. M., Cole S., Lacey C. G., 2006, MNRAS, 370, 645

Boylan-Kolchin M., Ma C.-P., Quataert E., 2008, MNRAS, 383, 93

Bruzual G., Charlot S., 2003, MNRAS, 344, 1000

Buitrago F., Trujillo I., Conselice C. J., Bouwens R. J., Dickinson M., Yan H., 2008, ApJ, 687, L61

Bullock J. S., Kolatt T. S., Sigad Y., Somerville R. S., Kravtsov A. V., Klypin A. A., Primack J. R., Dekel A., 2001, MNRAS, 321, 559

Cappellari M. et al., 2009, ApJL, 704, L34

Cappellari M. et al., 2012, Nat, 484, 485

Cassata P. et al., 2011, ApJ, 743, 96

Cenarro A. J., Trujillo I., 2009, ApJL, 696, L43

Centrella J., Melott A. L., 1983, Nat, 305, 196

Ceverino D., Dekel A., Mandelker N., Bournaud F., Burkert A., Genzel R., Primack J. R., 2012, MNRAS, 420, 3490

Chabrier G., 2003, PASP, 115, 763

Cheng J. Y., Faber S. M., Simard L., Graves G. J., Lopez E. D., Yan R., Cooper M. C., 2011, MNRAS, 412, 727

Christodoulou D. M., Shlosman I., Tohline J. E., 1995, ApJ, 443, 551

Cole S., Aragon-Salamanca A., Frenk C. S., Navarro J. F., Zepf S. E., 1994, MNRAS, 271, 781

Cole S., Lacey C. G., Baugh C. M., Frenk C. S., 2000, MNRAS, 319, 168

Conroy C., van Dokkum P. G., 2012, ApJ, 760, 71

Cook M., Barausse E., Evoli C., Lapi A., Granato G. L., 2010, MNRAS, 402, 2113

Covington M., Dekel A., Cox T. J., Jonsson P., Primack J. R., 2008, MNRAS, 384, 94

Covington M. D., Primack J. R., Porter L. A., Croton D. J., Somerville R. S., Dekel A., 2011, MNRAS, 1029

Cox T. J., 2004, PhD thesis, UC Santa Cruz

Cox T. J., Dutta S. N., Matteo T. D., Hernquist L., Hopkins P. F., Robertson B., Springel V., 2006, ApJ, 650, 791

Cox T. J., Jonsson P., Primack J. R., Somerville R. S., 2006, MNRAS, 373, 1013

Cox T. J., Jonsson P., Somerville R. S., Primack J. R., Dekel A., 2008, MNRAS, 384, 386

Croton D. J. et al., 2005, MNRAS, 356, 1155

Croton D. J. et al., 2006, MNRAS, 365, 11

Daddi E. et al., 2007, ApJ, 670, 156

Damjanov I. et al., 2009, ApJ, 695, 101

Davis M., Efstathiou G., Frenk C. S., White S. D. M., 1985, ApJ, 292, 371

De Lucia G., Fontanot F., Wilman D., Monaco P., 2011, MNRAS, 517

De Lucia G., Springel V., White S. D. M., Croton D., Kauffmann G., 2006, MNRAS, 366, 499

Dekel A. et al., 2009a, Nat, 457, 451

Dekel A., Cox T. J., 2006, MNRAS, 370, 1445

Dekel A., Sari R., Ceverino D., 2009b, ApJ, 703, 785

Dekel A., Zolotov A., Tweed D., Cacciato M., Ceverino D., Primack J. R., 2013, ArXiv, 3009

Djorgovski S., Davis M., 1987, ApJ, 313, 59

Dressler A., Lynden-Bell D., Burstein D., Davies R. L., Faber S. M., Terlevich R., Wegner G., 1987, ApJ, 313, 42

Dutton A. A., Mendel J. T., Simard L., 2012, MNRAS:L, 422, L33

Efstathiou G., Lake G., Negroponte J., 1982, MNRAS, 199, 1069

Faber S. M., Dressler A., Davies R. L., Burstein D., Lynden-Bell D., 1987, in Nearly Normal Galaxies. From the Planck Time to the Present, ed. S. M. Faber (New York, NY: Springer-Verlag), 175

Faber S. M., Jackson R. E., 1976, ApJ, 204, 668, a&AA ID. AAA017.158.036

Faber S. M., Jackson R. E., 1976, ApJ, 204, 668

Faber S. M. et al., 2007, ApJ, 665, 265, (c) 2007: The American Astronomical Society

Fan L., Lapi A., Bressan A., Bernardi M., De Zotti G., Danese L., 2010, ApJ, 718, 1460

Focardi P., Malavasi N., 2012, The Astrophysical Journal, 756, 117

Fontanot F., Cristiani S., Santini P., Fontana A., Grazian A., Somerville R. S., 2012, MNRAS, 421, 241

Fontanot F., De Lucia G., Monaco P., Somerville R. S., Santini P., 2009, MNRAS, 397, 1776

Forbes D. A., Ponman T. J., Brown R. J. N., 1998, ApJ, 508, L43

Forbes D. A., Spitler L. R., Strader J., Romanowsky A. J., Brodie J. P., Foster C., 2011, MNRAS, 413, 2943

Gallazzi A., Charlot S., Brinchmann J., White S. D. M., 2006, MNRAS, 370, 1106

Gallazzi A., Charlot S., Brinchmann J., White S. D. M., Tremonti C. A., 2005, MNRAS, 362, 41

Genel S., Dekel A., Cacciato M., 2012a, MNRAS, 3466

Genel S. et al., 2012b, ApJ, 745, 11

Genzel R. et al., 2011, ApJ, 733, 101

Gnedin N. Y., 2000, ApJ, 542, 535

Graves G. J., Faber S. M., 2010, ApJ, 717, 803

Graves G. J., Faber S. M., Schiavon R. P., 2009a, ApJ, 693, 486

Graves G. J., Faber S. M., Schiavon R. P., 2009b, ApJ, 698, 1590

Graves G. J., Faber S. M., Schiavon R. P., 2010, ApJ, 721, 278

Gunn J. E., Gott J. R. I., 1972, ApJ, 176, 1

Guo Q. et al., 2011, MNRAS, 164

Häring N., Rix H.-W., 2004, ApJ, 604, L89

Hatton S., Devriendt J. E. G., Ninin S., Bouchet F. R., Guiderdoni B., Vibert D., 2003, MNRAS, 343, 75

Henriques B. M. B., White S. D. M., Thomas P. A., Angulo R. E., Guo Q., Lemson G., Springel V., 2013, MNRAS, 1076

Hirschmann M., Somerville R. S., Naab T., Burkert A., 2012, MNRAS, 426, 237

Holden B. P., van der Wel A., Kelson D. D., Franx M., Illingworth G. D., 2010, ArXiv, 1009, 4479

Hopkins A. M., Beacom J. F., 2008, ApJ, 682, 1486

Hopkins P. F., Bundy K., Hernquist L., Wuyts S., Cox T. J., 2010, MNRAS, 401, 1099

Hopkins P. F., Cox T. J., Younger J. D., Hernquist L., 2009a, ApJ, 691, 1168

Hopkins P. F., Hernquist L., Cox T. J., Keres D., Wuyts S., 2009b, ApJ, 691, 1424

Hopkins P. F., Hernquist L., Cox T. J., Robertson B., Krause E., 2007, ApJ, 669, 45

Hopkins P. F., Lauer T. R., Cox T. J., Hernquist L., Kormendy J., 2009c, ApJS, 181, 486

Hopkins P. F. et al., 2009d, MNRAS, 397, 802

Hoyle B., Jimenez R., Verde L., 2011, Monthly Notices of the Royal Astronomical Society, 415, 2818

Hyde J. B., Bernardi M., 2009, MNRAS, 394, 1978

Ilbert O. et al., 2010, ApJ, 709, 644

Johansson P. H., Naab T., Burkert A., 2009, ApJ, 690, 802

Jones D. H. et al., 2009, MNRAS, 399, 683

Jones D. H. et al., 2004, MNRAS, 355, 747

Jørgensen I., Chiboucas K., Flint K., Bergmann M., Barr J., Davies R., 2006, ApJ, 639, L9

Jørgensen I., Franx M., Kjaergaard P., 1996, MNRAS, 280, 167

Kampczyk P. et al., 2013, The Astrophysical Journal, 762, 43

Kannappan S. J., 2004, ApJ, 611, L89

Kauffmann G. et al., 2003, MNRAS, 341, 54

Kauffmann G., White S. D. M., 1993, MNRAS, 261, 921

Kennicutt R. C., 1998a, ApJ, 498, 541

Kennicutt R. C., 1998b, ARA&A, 36, 189

Kennicutt, Jr. R. C., 1988, ApJ, 334, 144

Kereš D., Katz N., Weinberg D. H., Davé R., 2005, MNRAS, 363, 2

Khochfar S., Burkert A., 2003, ApJ, 597, L117

Kirby E. N. et al., 2010, The Astrophysical Journal Supplement, 191, 352

Klypin A. A., Trujillo-Gomez S., Primack J., 2011, ApJ, 740, 102

Kocevski D. D. et al., 2012, ApJ, 744, 148

Komatsu E. et al., 2009, ApJS, 180, 330

Komatsu E. et al., 2011, ApJS, 192, 18

Kormendy J., Fisher D. B., 2008, in Formation and Evolution of Galaxy Disks ASP Conference Series, p. 297

Koushiappas S. M., Bullock J. S., Dekel A., 2004, MNRAS, 354, 292

Kravtsov A. V., Gnedin O. Y., Klypin A. A., 2004, ApJ, 609, 482

Krumholz M. R., Dekel A., 2011, ArXiv, astro-ph.CO, 301

Loeb A., Rasio F. A., 1994, ApJ, 432, 52

Lotz J. M., Jonsson P., Cox T. J., Croton D., Primack J. R., Somerville R. S., Stewart K., 2011, ApJ, 742, 103

Lu Y., Mo H. J., Weinberg M. D., Katz N. S., 2010, ArXiv, 1004, 2518

Lynden-Bell D., 1967, MNRAS, 136, 101

Magoulas C. et al., 2012, MNRAS, 427, 245

Marchesini D. et al., 2007, ApJ, 656, 42

McConnell N. J., Ma C.-P., 2013, ApJ, 764, 184

Merloni A. et al., 2010, ApJ, 708, 137

Mihos J. C., Hernquist L., 1994, ApJ, 437, L47

Mo H. J., Mao S., White S. D. M., 1998, MNRAS, 295, 319

Moustakas J. et al., 2013, ApJ, 767, 50

Naab T., Jesseit R., Burkert A., 2006, MNRAS, 372, 839

Naab T., Johansson P. H., Ostriker J. P., 2009, ApJL, 699, L178

Naab T., Johansson P. H., Ostriker J. P., Efstathiou G., 2007, ApJ, 658, 710

Navarro J. F., Frenk C. S., White S. D. M., 1996, ApJ, 462, 563

Navarro J. F., Frenk C. S., White S. D. M., 1997, ApJ, 490, 493

Nelan J. E., Smith R. J., Hudson M. J., Wegner G. A., Lucey J. R., Moore S. A. W., Quinney S. J., Suntzeff N. B., 2005, ApJ, 632, 137

Newman A. B., Ellis R. S., Bundy K., Treu T., 2012, ApJ, 746, 162

Nipoti C., Treu T., Leauthaud A., Bundy K., Newman A. B., Auger M. W., 2012, MNRAS, 422, 1714

Noeske K. G. et al., 2007a, ApJ, 660, L47

Noeske K. G. et al., 2007b, ApJ, 660, L43

Oesch P. A. et al., 2010, ApJL, 714, L47

Oser L., Naab T., Ostriker J. P., Johansson P. H., 2012, ApJ, 744, 63

Oser L., Ostriker J. P., Naab T., Johansson P. H., Burkert A., 2010, ApJ, 725, 2312

Padmanabhan N. et al., 2004, New Astronomy, 9, 329

Pahre M. A., Djorgovski S. G., de Carvalho R. R., 1998, ApJ, 116, 1591

Parry O. H., Eke V. R., Frenk C. S., 2009, MNRAS, 396, 1972

Porter L., Somerville R. S., Croton D. J., Covington M. D., Graves G. J., Faber S. M., Primack J. R., 2012, ArXiv, 1201, 5918

Press W. H., Schechter P., 1974, ApJ, 187, 425, a&AA ID. AAA011.162.012

Quilis V., Trujillo I., 2012, ApJL, 752, L19

Raichoor A. et al., 2011, The Astrophysical Journal, 732, 12

Robertson B., Bullock J. S., Cox T. J., Matteo T. D., Hernquist L., Springel V., Yoshida N., 2006a, ApJ, 645, 986

Robertson B., Cox T. J., Hernquist L., Franx M., Hopkins P. F., Martini P., Springel V., 2006b, ApJ, 641, 21

Sani E., Marconi A., Hunt L. K., Risaliti G., 2011, MNRAS, 413, 1479

Shankar F., Marulli F., Bernardi M., Dai X., Hyde J. B., Sheth R. K., 2010, MNRAS, 403, 117

Shankar F., Marulli F., Bernardi M., Mei S., Meert A., Vikram V., 2011, ArXiv, 1105, 6043

Shankar F., Marulli F., Bernardi M., Mei S., Meert A., Vikram V., 2013, MNRAS, 428, 109

Shen S., Mo H. J., White S. D. M., Blanton M. R., Kauffmann G., Voges W., Brinkmann J., Csabai I., 2003, MNRAS, 343, 978

Silk J., 1977, ApJ, 211, 638

Smith R. J., Lucey J. R., Hudson M. J., 2007, MNRAS, 381, 1035

Somerville R. S. et al., 2008a, ApJ, 672, 776

Somerville R. S., Gilmore R. C., Primack J. R., Domínguez A., 2012, MNRAS, 2820

Somerville R. S., Hopkins P. F., Cox T. J., Robertson B. E., Hernquist L., 2008b, MNRAS, 391, 481

Somerville R. S., Primack J. R., 1999, MNRAS, 310, 1087

Somerville R. S., Primack J. R., Faber S. M., 2001, MNRAS, 320, 504

Spiniello C., Trager S. C., Koopmans L. V. E., Chen Y. P., 2012, ApJL, 753, L32

Springel V., 2005, MNRAS, 364, 1105

Springob C. M. et al., 2012, MNRAS, 420, 2773

Strateva I. et al., 2001, AJ, 122, 1861

Strauss M. A., Weinberg D. H., Lupton R. H., Narayanan V. K., Annis J., Bernardi M., York D. G., Zehavi I., 2002, AJ, 124, 1810

Sutherland R. S., Dopita M. A., 1993, ApJS, 88, 253

Syer D., Mao S., Mo H. J., 1999, MNRAS, 305, 357

Tegmark M., Silk J., Rees M. J., Blanchard A., Abel T., Palla F., 1997, ApJ, 474, 1

Terlevich A. I., Forbes D. A., 2002, MNRAS, 330, 547

Toft S., Franx M., van Dokkum P., Förster Schreiber N. M., Labbe I., Wuyts S., Marchesini D., 2009, ApJ, 705, 255

Toft S. et al., 2007, ApJ, 671, 285

Toomre A., 1964, ApJ, 139, 1217

Toomre A., 1977, in Evolution of Galaxies and Stellar Populations, p. 401

Toomre A., Toomre J., 1972, ApJ, 178, 623

Tortora C., Napolitano N. R., Romanowsky A. J., Capaccioli M., Covone G., 2009, MNRAS, 396, 1132

Trager S. C., Somerville R. S., 2009, MNRAS, 395, 608

Treu T., Ellis R. S., Liao T. X., van Dokkum P. G., 2005a, ApJ, 622, L5

Treu T. et al., 2005b, ApJ, 633, 174

Trujillo I., Ferreras I., de la Rosa I. G., 2011, MNRAS, 415, 3903

Trujillo I. et al., 2006, ApJ, 650, 18

Trujillo-Gomez S., Klypin A., Primack J., Romanowsky A. J., 2011, ApJL, 742, 16

van der Wel A., Franx M., van Dokkum P. G., Rix H.-W., 2004, ApJ, 601, L5

van Dokkum P. G., van der Marel R. P., 2007, ApJ, 655, 30

van Dokkum P. G. et al., 2010, ApJ, 709, 1018

Volonteri M., Stark D. P., 2011, MNRAS, 417, 2085

Wechsler R. H., Bullock J. S., Primack J. R., Kravtsov A. V., Dekel A., 2002, ApJ, 568, 52

Wetzel A. R., 2010, ApJ, 412, 49

Whitaker K. E., van Dokkum P. G., Brammer G., Franx M., 2012, ApJL, 754, L29

Williams R. J., Quadri R. F., Franx M., van Dokkum P., Toft S., Kriek M., Labbé I., 2010, ApJ, 713, 738

Williams R. J., Quadri R. F., Franx M., van Dokkum P., Toft S., Kriek M., Labbé I., 2010, ApJ, 713, 738

Woo J., Courteau S., Dekel A., 2008a, Monthly Notices of the Royal Astronomical Society, 390, 1453

Woo J.-H., Treu T., Malkan M. A., Blandford R. D., 2008b, ApJ, 681, 925

Worthey G., Faber S. M., Gonzalez J. J., Burstein D., 1994, ApJS, 94, 687

Worthey G., Ottaviani D. L., 1997, ApJS, 111, 377

Wuyts S. et al., 2011, ApJ, 742, 96

York D. G., Adelman J., Anderson J. E., Anderson S. F., Yanny B., Yasuda N., 2000, AJ, 120, 1579

Zel'Dovich Y. B., 1970, A&A, 5, 84